ABSTRACT

Title of Document: PROGNOSTICS OF POLYMER POSITIVE TEMPERATURE COEFFICIENT RESETTABLE FUSES

Shunfeng Cheng, Doctor of Philosophy (Ph.D.), 2011

Directed By: Professor Michael G. Pecht
Department of Mechanical Engineering

Polymer positive-temperature-coefficient (PPTC) resettable fuse has been used to circuit-protection designs in computers, automotive circuits, telecommunication devices, and medical devices. PPTC resettable fuse can trip from low resistance to high resistance under over-current conditions. The increase in the resistance decreases the current and protects the circuit. After the abnormal current is removed, and/or power is switched off, the fuse resets to low resistance stage, and can be continuously operated in the circuit. The resettable fuse degrades with the operations resulting in loss or abnormal function of the protection of circuit. This thesis is focused on the prognostics methods for resettable fuses to provide an advance warning of failure and to predict the remaining useful life.

The failure precursor parameters are determined first by systematic analysis using failure modes, mechanisms, and effects analysis (FMMEA) followed by a series of experiments to verify these parameters. Then the causes of the observed

failures are determined by failure analyses, including the analyses of interconnections between different parts, the microstructures of the polymer composite, the properties (such as crystallinity) of the polymer composite, and the coefficient of thermal expansion (CTE) of different parts. The revealed failure causes include the cracks and gaps between different parts, the agglomerations of the carbon black particles, the change in crystallinity of the polymer composite, and the CTE-mismatches between different parts.

Cross validation (CV) sequential probability ratio test (CVSPRT) is developed to detect anomalies. CV methods are introduced into SPRT to determine the model parameters without the need of experience and reduce the false and missed alarms. A moving window training updating based dynamic model parameter optimization (MW-DMPO) n-steps-ahead prognostics method is developed to predict the failure. MW methods update the training data for prediction models by a moving window to contain the latest degradation information/data and improve the prediction accuracy. For each updating of the training data, the model parameters for data-trending model are updated dynamically. Based on the developed MW-DMPO method, a MW cross validation support vector regression (MW-CVSVR) n-steps-ahead prediction is developed to predict failures of PPTC resettable fuses in this thesis. The cross validation method is used to determine the proper SVR model parameters. The CVSPRT anomaly detection method and MW-DMPO n-steps-ahead prognostics method developed in this thesis can be extended as general methods for anomaly detection and failure prediction.

PROGNOSTICS OF POLYMER POSITIVE TEMPERATURE COEFFICIENT RESETTABLE FUSES

By

Shunfeng Cheng

Dissertation submitted to the Faculty of the Graduate School of the
University of Maryland, College Park, in partial fulfillment
of the requirements for the degree of
Doctor of Philosophy
2011

Advisory Committee:
Professor Michael G. Pecht (Advisor), Chair
Professor Donald Barker
Professor Bilal Ayyub (Dean's representative)
Professor Peter Sandborn
Associate Professor David Bigio

Dedication

This dissertation is dedicated to my lovely wife, Haiyan Zhang, my parents-in-law, Tiehua Zhang and Guangping Wei, and my father, An Cheng, who support me all the time. Especially, this dissertation is a memorial to my mother, Yaogui Zhang, who always gave me her endless love.

Acknowledgements

First, I would like to express my gratitude and respect to Prof. Michael Pecht for his guidance in this interesting dissertation topic and challenging me to set a higher standard. I appreciate him for his continuous support towards the progress of this work and the valuable help on my writing and presenting skills.

I would also like to thank Prof. Donald Barker, Prof. Bilal Ayyub, Prof. Peter Sandborn, and Prof. David Bigio for serving on my dissertation committee and providing valuable suggestions.

I would like to especially thank Dr. Michael Azarian and Dr. Diganta Das for their insightful advice to this work. I further thank the Prognostics and Health Management Consortium in Center for Advanced Life Cycle Engineering (CALCE) for its support. I would like to thank Dr. Michael Osterman, Dr. Nikhil Lakhkar, Dr. Alex Coppe, Mr. Bhanu Sood, Mr. Anshul Shrivastava, and Mr. Mark Zimmerman for their supports on my experiments and help on this thesis.

I would like to thank my friends and colleagues at CALCE including Dr. Nikhil Vichare, Dr. Jie Gu, Dr. Lei Nie, Dr. Daeil Kwon, Dr. Sachin Kumar, Dr. Nishad Patil, Weiqiang Wang, Wei He, Xiaofei He, Jin Tian, Gilbert Haddad, Edwin Sutrisno, Vasilis Sotiris, Hyunseok Oh, Sandeep Menon, Mohammed Alam, and Sony Mathew for their help during my graduate experience. I would like to thank Dr. Larry Lai in Nano Center, Dr. Xin Zhang in Material Science, and Dr. Peter Zavalij in Department of Chemistry and Biochemistry for their help on the analyses of samples.

Finally, I would like to extend very special thanks to my wife Haiyan Zhang and my family for their constant support and encouragement towards my work.

Table of Contents

List of Publications

Published Journal Papers:

- S. Cheng, K. Tom, L. Thomas, and M. Pecht, "A Wireless Sensor System for Prognostics", IEEE Sensors Journal, Volume 10, Issue 4, pp. 856 – 862, 2010.
- S. Cheng, M. Azarian, and M. Pecht, "Sensor System for Prognostics and Health Monitoring," Sensors, No. 10, pp.5774-5797, 2010.
- S. Cheng, K. Tom, and M. Pecht, "Failure Precursors for Polymer Resettable Fuses," IEEE Transactions on Devices and Materials Reliability, Vol.10, Issue.3, pp.374-380, 2010.
- M. Pecht and S. Cheng, "Prognostics and Health Management Method for Aging Systems", U.S. Patent Application Publication, No. US 2010/0191681 A1, Jul. 2010.

Published Conference Papers

- S. Cheng, K. Tom, and M. Pecht, "Prognostics for Polymer Positive Temperature Coefficient Resettable Fuses," Machinery Failure Prevention Technology 2011, Virginia Beach, VA, May. 2011.
- S. Cheng and M. Pecht, "A Fusion Prognostics Method for Remaining Useful Life Prediction of Electronic Products," 5th Annual IEEE Conference on Automation Science and Engineering, Bangalore, India, pp. 102-107, August 22-25, 2009.
- S. Cheng, L. Thomas, J. Cook, and M. Pecht, "A Radio Frequency Sensor System for Prognostics", ASME/CIE 2009, San Diego, CA, August 2009.
- S. Cheng, M. Torres, L. Thomas, and M. Pecht, "Autonomous Prognostic

Monitoring Device," Proceedings of the 62th Meeting of the Society for Machinery Failure Prevention Technology, pp.505-516, Virginia Beach, VA, May. 2008.

- S. Cheng and M. Pecht, "Multivariate State Estimation Technique for Remaining Useful Life Prediction of Electronic Products," Symposium on Artificial Intelligence for Prognostics, pp.26-32, Arlington, VA, 2007.
- B. Tuchband, S. Cheng, and M. Pecht, "Technology Assessment of Sensor Systems for Prognostics and Health Monitoring," IMAPS on Military, Aerospace, Space and Homeland Security: Packaging Issues and Applications (MASH), May. 2007.

Submitted Journal Papers

- S. Cheng and M. Pecht, "Using Cross validation for Model Parameter Selection of Sequential Probability Ratio Test," Submitted to Journal Expert Systems with Applications on 06/17/11.
- S. Cheng, D. Das, M. Pecht, "Using FMMEA to Improve Medical Device Adverse Event Investigations and Reporting", Submitted to journal: Expert Review of Medical Devices on 6/16/2011.
- S. Cheng and M. Pecht, "A Moving Window based Dynamic Model Parameter Optimization N-steps-ahead Prognostics Method," Submitted to Journal Expert Systems with Applications on 06/11/2011.
- S. Cheng, K. Tom, and M. Pecht, "Anomaly Detection of Polymer Positive Temperature Coefficient Resettable Fuses," Submitted to Journal IEEE Transactions on Power Electronics on 06/12/2011.

- S. Cheng, K. Tom, and M. Pecht, "Failure Analysis of Polymer Positive Temperature Coefficient Resettable Fuses". Submitted to Journal IEEE Transactions on Electron Devices on 06/12/2011.
- J. Sun, S. Cheng, and M. Pecht, "Prognostics of Multilayer Ceramic Capacitors Via the Parameter Residuals," submitted to IEEE Transactions on Devices and Materials Reliability in Dec. 2010.

List of Tables

List of Figures

Chapter 1: Introduction

A polymer positive temperature coefficient (PPTC) resettable fuse can "trip" from its normal operational state of low resistance to high resistance when overheated by ambient heat or the Joule heat generated by high current. It can reset to its normal operational state of low resistance when the heat is removed and/or the power is switched off.

1.1 Positive Temperature Coefficient Effect

The trip is caused by an effect of positive temperature coefficient (PTC) for some materials [1]-[6]. According to PTC effect, the resistance of a component increases (decreases) with the increases (decreases) in its temperature. A PPTC resettable fuse is made of polymer composites, which are mixed by conductive particle fillers, such as carbon black particles, and non-conductive semi-crystalline polymer matrix, such as polyethylene[4][5]. The mixing of the conductive particles into the polymer matrix changes the conductivity of the entire polymer composite and enables it to exhibit the PTC effect. Figure 1 is a resistance vs. temperature curve for a typical PPTC resettable fuse. A sharp increase in resistance is observed in a narrow temperature range (100°C -130°C in the example), lower than which the increase in resistance is not obvious with the increase in temperature. The PPTC resettable fuses utilize this sharp increase in resistance to reduce the current of a circuit quickly so as to protect the circuit.

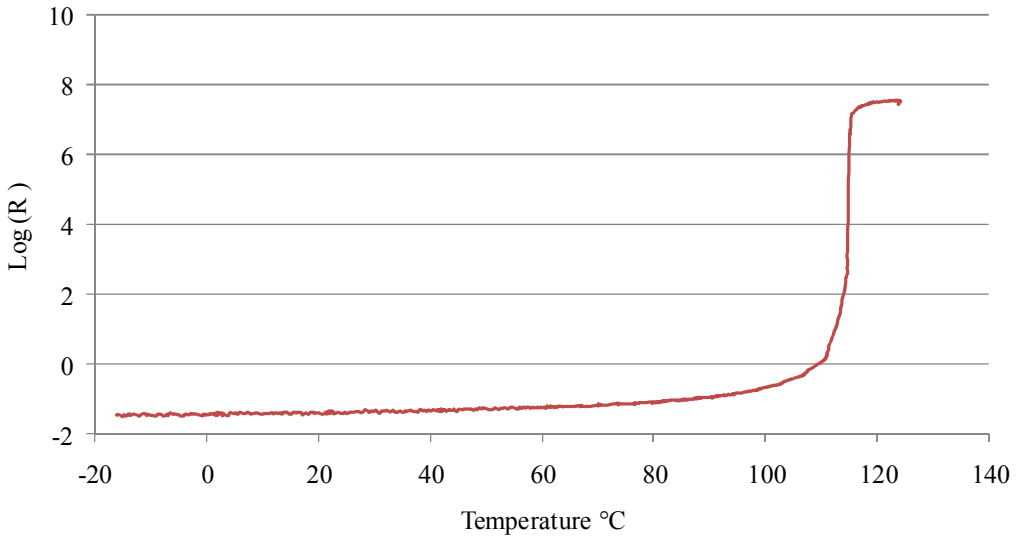

Figure 1: Resistance (Log (R)) vs. temperature curve of a PPTC resettable fuse

1.2 Operation of PPTC Resettable Fuses

Figure 2 is a schematic picture to show the operational process of a typical PPTC resettable fuse [7]. Under normal ambient temperature, the fuse works in a low resistance state (like a wire) when the normal current (less than the hold current, I_{hold}, which is the maximum steady-state current the PPTC device can carry without tripping at the ambient temperature) passes through it. When a fault current (higher than trip current, I_{trip}, which is the minimum current that causes a PPTC device to trip at the ambient temperature) occurs, the resistance of the fuse increases sharply. Because of the sharp increase in resistance, the current is decreased to protect the circuit. The sharp increase in resistance is called trip. After the trip, a PPTC resettable fuse does not break as does a traditional fuse. Instead, it keeps the high resistance state and allows a small trickle current to pass through the circuit. The fuse will reset

to a low resistance state within a short time after the heat or fault current is removed and/or the power is switched off [1]-[7]. The trip time is defined as the time required for a PPTC fuse to decrease the current of the circuit to 50% of the trip current at the ambient temperature [6]. Typically, the hold current (I_{hold}) is half of the trip current. When the current is higher than the trip current, the fuse will trip. When the current is lower than the hold current, the fuse will not trip. When the current is between the hold current and the trip current, the fuse may or may not trip [4][5][6]. After a number of trip-reset cycles, the PPTC resettable fuse will degrade and failures will occur [7].

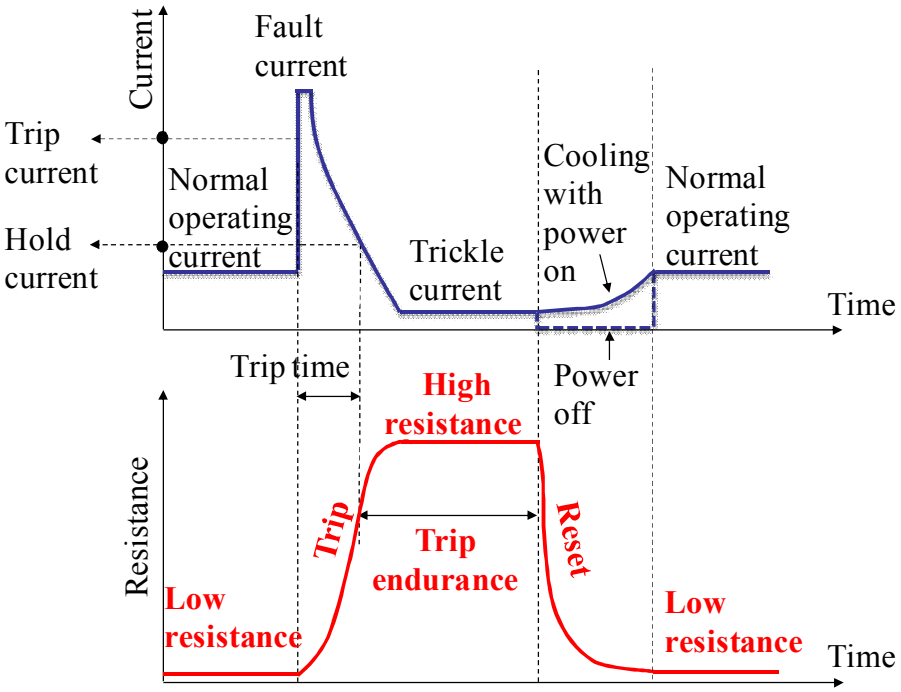

Figure 2: Operation process of PPTC resettable fuse

1.3 Motivation

As a circuit protection device, polymer positive temperature coefficient (PPTC) resettable fuses are widely used in automotive circuits (e.g., the protection of micro-motors in window lifts, seats, and door locks), computers (e.g., the protection of the circuits in hard disk drives, interface ports, and cooling fan motors), telecommunication devices (e.g., cell phones), battery packs, power supplies, medical electronics, and so on [7]. The failure or abnormal behaviors of PPTC devices may cause damage to circuits, abnormal operation of circuits (e.g., inability to work at normal current), or unnecessary operations that force operators to switch off and on the power to reset the circuit. It is necessary to monitor the PPTC resettable fuses *in-situ* to provide advance warning of failures and predict the remaining useful life (RUL) to prevent damage to the circuits.

Prognostics and health management (PHM) has been emerging as an effective method to achieve these requirements. PHM is an enabling discipline consisting of technologies and methods to assess the reliability of a product in its actual life cycle conditions to determine the advent of failure and mitigate system risk [8][9]. PHM generally combines sensing and interpretation of environmental, operational, and performance-related parameters to assess the health of a product and predict remaining useful life. Assessing the health of a product provides information that can be used to meet several critical goals: (1) providing advance warning of failures; (2) minimizing unscheduled maintenance, extending maintenance cycles, and maintaining effectiveness through timely repair actions; (3) reducing the life-cycle

cost of equipment by decreasing inspection costs, downtime, and inventory; and (4) improving qualification and assisting in the design and logistical support of fielded and future systems[8][9].

1.4 Problem Statement and Research Work

As the literature review in chapter 2 shows, the research on prognostics of PPTC resettable fuses has been very limited. There are no established methods to provide the prognostics and health monitoring for PPTC resettable fuses. Firstly, the failure precursor parameters to be monitored have not been determined. This causes the difficulty or increases the complexity of *in-situ* monitoring. Furthermore, the causes of the observed failures of PPTC resettable fuses have not been determined. Without the determination of the root causes of the failures, it is difficult to identify the failure mechanisms and is hard to improve the design and the reliability of the products in the future. The last one, anomaly detection and failure prediction methods have not been developed for PPTC resettable fuses.

This thesis is focusing on solving these problems by the following research work: 1) determining the failure precursors by failure modes, mechanisms, and effects analysis, followed by conducting a series of experiments to verify the parameters; 2) Determining the root causes of the failure by failure analysis methods; 3) Developing data-driven anomaly detection and prediction methods to detect the anomalies and predict the failures of the resettable fuses in time.

1.5 Overview of Thesis

Chapter 2 provides the literature review on principle of PPTC effect, reliability of PPTC resettable fuses, prognostics of PPTC resettable fuses, and describes the problems not covered in literature. Chapter 3 describes the processes and results of determining the failure precursor parameters. Chapter 4 reports the failure analysis methods and results to determine the root causes of the failures. Chapter 5 describes the development of anomaly detection method using cross validation sequential probability ratio test (CVSPRT). In Chapter 6, a moving window (MW) training updating based dynamic model parameter optimization n-steps-ahead prognostics method is developed. Based on this MW method, a MW cross validation support vector regression (MW-CVSVR) prognostics method is developed to conduct the failure prediction for PPTC resettable fuses. Chapter 7 discusses the contributions and future work.

Chapter 2: Literature Review

The literature review includes the following aspects: 1) the operational principle of PPTC resettable fuses; 2) electrical characteristics of PPTC resettable fuses; 3) factors affecting the characteristics of PPTC resettable fuses; 4) the reliability evaluation of the PPTC resettable fuses; and 5) prognostics methods. After the literature review, the unaddressed problems are described in the summary.

2.1 Operational Principle of PPTC Resettable Fuses

The understanding of the operational principle of the PPTC resettable fuse can help to identify its failure causes and mechanisms. In general, a PPTC resettable fuse includes electrodes, conductive polymer composite, and outside coating. The polymer composite is the functional part having PTC effect. It is a mixture of non-conductive polymer, such as polyethylene, and conductive fillers, such as carbon black (CB) particles.

Figure 3: Picture of a radial through-hole PPTC resettable fuse

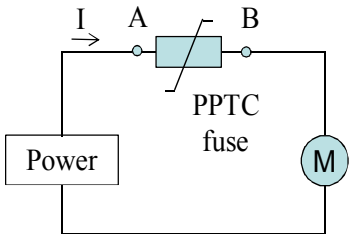

Figure 4: Connection of a PPTC resettable fuse in a circuit

Figure 3 is a picture of a radial through-hole PPTC resettable fuse. There are other types of PPTC resettable fuses in the market, such as surface mount components. The fuse is connected with other components in series in a circuit, shown in Figure 4.

Both the mechanisms of the conduction of polymer composite under normal conditions and the mechanisms of the increase in resistance under abnormal conditions should be understood. Although many models [1][2][10]-[19] have been proposed in an attempt to explain PTC effect in polymer composites, a model that can explain all the phenomenon of PPTC effects is not available yet. The main models include conductive chain and thermal expansion model by Kohler [11], tunneling conductance model by Ohe *et al.* [17], CB aggregation structure change and migration model by Klason *et al.*[18], and Ohm conductance and phase change model by Allak *et al.*[19]. The summary of these models is shown in Table 1. Currently, the conductive chain and thermal expansion model is used to explain the principle in most of literature, for example, Wei *et al.* [1], Luo *et al.* [2], Gorniak *et al.*[3], Doljack *et al.* [12], because of the ease of understanding.

Figure 5, by Cheng *et al.* [7], shows the schematic picture of the structure of a radial through-hole resettable fuse shown in Figure 3. In general, radial through-hole PPTC fuses include conductive polymer composites, electrodes, and outside coatings [4][5]. Conductive polymer composite is generally manufactured as a thin sheet and consists of non-conductive polymer (e.g., polyethylene) and conductive particles (e.g., carbon black (CB)). An electrode is used to conduct and control the flow of electricity and is typically composed of foils and leads.

Table 1: PPTC models

Models	At low temperature	At crystalline to amorphous phase transition temperature	Defects or cannot explain
Conductive chain and thermal expansion model by Kohler [11]	Polymer is in semi-crystalline state; conductive fillers form conductive chains.	Phase transition from crystalline to amorphous→ volume is expanded → conductive chains are broken	Why the sharpness of resistance rise is not a function of volume change
Tunneling conductance model by Ohe *et al.* [17]	Distribution of conductive filler is uniform; gaps between the conductive fillers are small and electron tunnels are formed	Distribution becomes random→ gaps between conductive fillers increase to break the electron tunnels.	Why the particle distribution changes from uniform to random distribution
CB aggregation structure change and migration model by Klason *et al.*[18]	CB aggregation structure is determined by crystalline phase of polymer; CB particles distribute in amorphous phase and form conductive chain.	Phase transition from crystalline to amorphous breaks the CB aggregation structures → a more homogenous particle distribution	Lack of enough experiment results to support
Ohm conductance and phase change model by Allak *et al.*[19]	Linear I-V curve (Ohm behavior); CB resides in amorphous regions → easily establish conductive chains	Crystalline to amorphous with a sudden and large volume increase→gap between new formed amorphous and enlarged amorphous regions reduce→more resistive current pathways→break up the conductive chains	Lacks of enough experiment results to support

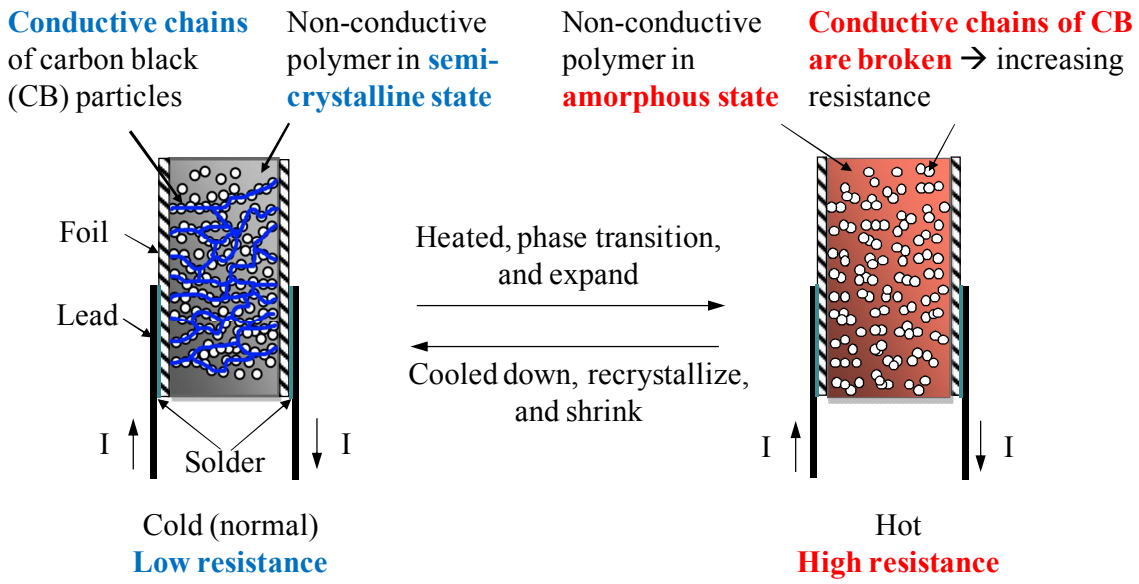

Figure 5: Conductive chain and thermal expansion model

The foils are attached on both sides of the polymer sheet. One lead is connected to each foil by soldering. The dielectric coating material provides protection for the outside of the device.

According to conductive chain and thermal expansion model, at normal temperatures, the conductive particles in the polymer form many conductive paths, which allow current to flow through the fuses without interruption. However, if the temperature rises around the crystalline to amorphous (C→A) phase transition temperature of the polymer, some crystalline state of the polymer will change to amorphous state. The expansion in volume of the polymer during the phase change separates the conductive particles and breaks the conductive paths. This results in a large nonlinear increase in the resistance of the PPTC device just in a narrow temperature range. The whole process of this model is shown in Figure 5 [7].

2.2 Electrical Characteristics of PPTC Resettable Fuses

Some electrical characteristics of PPTC composites should be concerned in the applications. For example, the relationship between resistance and temperature of the fuse is shown in Figure 1. The relationship between the volume (or thickness) of the fuse and the temperature were also introduced by Kohler [11], Doljack [12], and Founrnier *et al.*[14]. For example, Doljack [12] described that the electrical resistivity of conductive polymer composites was determined by the type of CBs and the volume ratio of total CB to polymer. The initial resistance of the devices is defined based on the maximum volume ratio of CB to polymer.

Trip time is dependent upon the size of the current and the ambient temperature. The trip time with different current under a certain temperature should be given by manufacturer. This information is used to guide the users to select the proper devices for their applications. For example, Bourns [20] provide the curve of trip time vs. current under temperature 23 °C in the datasheets. Trip time under 23 °C is used as a reference for users to select the proper fuses for their applications. The trip time decreases with the increasing of the current through the fuse. Figure 6 illustrates schematically the hold- and trip-current behaviors of PPTC devices as a function of temperature [4][5]. Region A describes the combinations of current and temperature at which the PPTC device will trip and protect the circuit. Region B describes the combinations of current and temperature in which the device will allow for normal operation of the circuit. In region C, it is possible for the device to either trip or remains in the low resistance state, depending on the individual device resistance and

its environment. The specific hold current value under different temperature conditions are shown in the datasheet of the fuse.

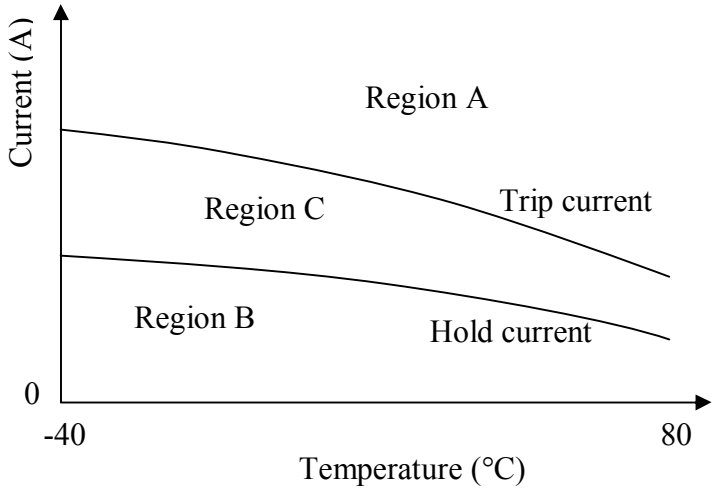

Figure 6: Trip- and hold-current vs. temperature

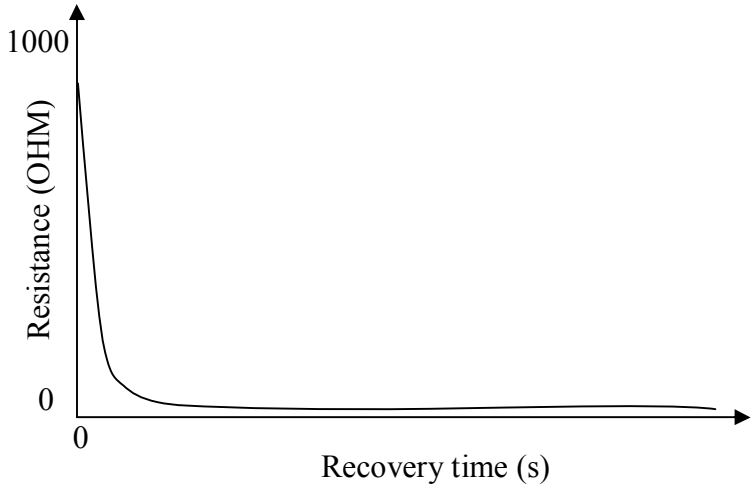

Figure 7: Recovery of PPTC fuse

The recovery of PPTC fuse occurs within the first several seconds. Figure 7 show the process schematically. The resistance fully recovery is depended on both the design of the device and thermal environment. After tripped, the return to maximum

volume compaction of the polymer is a much slower process than simple cooling alone [11].

2.3 Factors Affecting Characteristics of PPTC Resettable Fuses

The factors that affect the characteristics of PPTC resettable fuses include the properties of the polymers, the particle fillers, and the processing conditions, which were mentioned by many researchers, such as Huang [21], Zhang *et al.* [22], Sau *et al.* [23], and Narkis *et al.* [24]. Different conductive particle fillers, such as metal powders or fibers [25], or CB [26], can be dispersed into a plastic matrix to enable the non-conductive plastic become conductive when the concentration of the filler reaches a threshold, which was discussed by many researchers, such as Zhang [22], Miyasaka*et al.* [27], and Lux [28]. Although metal particles are more conductive than CB, CB is applied as the common filler in the PPTC resettable fuses because of CB's resistance on oxidization, which forms an insulating layer on the surface of the filler.

CB is an amorphous form of carbon with a structure similar to disordered graphite. Huang [21] summarized five types of CBs in the CB industry: furnace black, thermal black, lamp black, channel black, and acetylene black. Over 90% of the CBs current produced are made by the furnace process. In this process, oil is thermally decomposed to form CB particles [29]. The general diameter range of the particles to fill in the polymer is less than 100 nm.

Many researchers, such as Mironi-Harpaz *et al.* [30], Donnet [31], and Bourat [32], pointed out that CB particles have trends to aggregate together so that under electron microscope examination CB is composed of prime particles fused into

primary aggregates. The small aggregates also trend to aggregate together again to form larger agglomerates. Zhang *et al.* [22], Narkis *et al.* [24], and Xi *et al.* [33] stated that when the CBs particles or aggregates are filled into polymer matrix, they sit in the amorphous phase of the polymer and are separated by polymer matrix. But when the gap between aggregates is less than some critical distance, electrons can flow across the polymer barrier, and generate a high conductivity [33]. When the polymer is heated and the temperature increase to a certain level, the crystal in the polymer may change its phases from crystalline to amorphous. This phase transition increases the amorphous phases, which cause to the decrease in the density of CBs and increase in the distance between CBs, and cause to the increase in the resistance [33]. The CBs obtain more energy at high temperature and more of them are aggregating together.

Researchers also investigated the effects of using different polymer matrix on the electrical and mechanical properties of PPTC polymer composites. For example Xi *et al.* [33] used polyethylene, Sumita *et al.* [34] and Huang *et al.* [35] used Ethylene-Vinyl Acetate Copolymer, and Tchoudakov *et al.* used the polypropylene/polyamide [36]. It is found that the threshold concentration is affected by the interaction between the polymer and CB, the crystallinity and melts viscosity of the polymer [21][34]-[37]. Huang [21] summarized that if the CB particle-to-particle aggregation is stronger than the adhesion between CB particles and polymer, the CB particles will aggregate and be hard to separate and disperse into the polymer matrix; but in the opposite, the particles will disperse into the polymer without contact, which affects the form of the conductive paths if the concentration of particle

is not too high. So with the increase of the surface tensions of the polymers, the threshold concentration increased. That means more particles are needed to fill into the polymer with high extension to obtain high conductivity.

The other important effect of different polymer on the conductivity of composite is the crystallinity. Semi-crystalline polymer contains crystalline regions and amorphous regions. The crystallinity is used to measure the ratio of crystalline regions. Researches show the threshold concentration increases with the decrease in the crystallinity [38]-[46]. CB particles are dispersed uniformly in the amorphous regions and rejected from the crystalline regions, which was reported by He *et al.* [38], Park [40], Hunag *et al.*[41], Xu *et al.* [43], and Yui *et al.* [45].

Experiments were conducted to evaluate the effect of different high-crystallinity resin and different content of CB on the electrical conductivity of PPTC device [38]-[40][45][46]. For example, Horibe *et al.* [46], investigated the relationship between the resistivity and the crystallinity, and the relationship between the resistivity and carbon content. During the test, the crystallinity of each polymer was determined by X-ray diffraction analysis, and the carbon particle size was directly measured by scanning electron microscopy (SEM). He found that high-density polyethylene (HDPE) has lowest resistivity at room temperature and the highest resistivity after polymer melting. The higher the crystallinity of HDPE is, the lower the resistivity of the composites. The resistivity of the composites decreased with increasing CB content.

The polymer composite tested in this thesis is made of carbon black particles and polyethylene (PE). PE is a semi-crystalline polymer. PE can be classified simply as low density PE (LDPE) and high density PE. Table 2 shows the different properties of them [48].

Table 2: Some properties of LDPE and HDPE

Property	LDPE	HDPE
Formula	$-(CH_2\text{-}CH_2)_n-$	$-(CH_2\text{-}CH_2)_n-$
Melting temperature (crystalline to amorphous transition temperature)	Around 110°C	Around 130°C
Glass transition temperature	Around -110°C	Around -100°C
Crystallinity	< 50%	>90%
Density	0.91-0.94 g/cm^3	0.95-0.97 g/cm^3

Researchers reported that CBs were dispersed into the amorphous region of the PE [38]-[42]. When the temperature is well below the C→A transition point of the PE, the crystalline and amorphous phase is in a solid state, and the resistivity of the composite does not rise significantly with the rise in temperature. Close to the C→A transition point of the polyethylene, the crystalline phase starts to form new amorphous regions. Such structural changes perturb the conducting pathways and consequently, the resistivity of the material increase. The C→A transition increases the volume of amorphous parts, which decrease the volume percent of particle fillers, causes to the increase in inter-distance between particles and the increase in the resistance.

In general, the aggregate of the particles increases the resistance compared with the resistance when the particles are distributed in uniformly, under which more random conductive networks are formed to decrease the resistance. Yui *et al.* [45] used SEM to investigate the aggregation of CB particles and found that CB particles in HDPE aggregated together but these aggregates did not contact together to form conductive networks, thus increased the resistance.

2.4 Reliability and Testing of PPTC Resettable Fuses

The research on the reliability of PPTC resettable fuses has been very limited. A surface-mount PPTC manufactured by Raychem Corporation was tested by White *et al.*[49]. The trip cycle life and the trip endurance life were evaluated from trip tests. The distribution was assumed as an exponential distribution, in which the constant failure rate was estimated through the 100 cycle test. The estimation was that there would be less than one failure out of 276816 trips. The failure of PPTC resettable fuse was defined as the observation of arcing or tripping below the hold current. The estimation for the trip endurance was that there would be less than one failure out of 75,900 tripped hours at 95% confidence level [49].

This work also tested the effect of electrical aging and environmental aging on the trip cycling and trip endurance. The data then were fitted in a statistical model to calculate the time to failure. No cause analyses of the failure were conducted. The device resistance increased with tripping cycles. One failure mode was that, after number of trip cycles or trip endurance, devices would become high enough in

resistance that they would not pass the normal operating current (hold current), and device would nuisance trip.

The environmental aging was generated by the effects of temperature and humidity. Results showed that heat aging caused devices to decrease in resistance from their post-reflow resistance. Higher aging temperatures caused a faster decrease. The results were shown in the Table 3.

Table 3: Test results by White *et al.* [49]

		Resistance (Ohm)	Trip Time (Sec) (15V 8A)	Trip Current(A) (15V 8A)
6000 trip cycles at 15V 40A, 10 sec on, 50 sec off at 20 °C	Before	0.422±0.0219	0.013±0.0005	7.4±0.09
	After	4.25±2.24	0.004±0.0004	6.7±0.18
125 days at 70 °C	Before	0.444±0.022	0.012±0.0008	7.4±0.08
	After	0.258±0.006	0.011±0.0006	7.4±0.07

The failure of the fuse in field was defined as the fuse had not tripped properly. The possible failure modes include the device becoming high in resistance, arcing, or delaminating during trip. Some tests, such as trip cycle test and aging test, are conducted by manufacturing or certified institution based on the standard UL 1434 [6]. Test results are listed in the datasheets of the products. However, these tests are not enough to evaluate the reliability of the PPTC resettable fuses. One of the reasons

is that the number of test cycles is not enough to observe the changes in the properties.

2.5 Prognostics Methods

Prognostics is an emerging technique in recent years. Anomaly detection and prognostics of PPTC have not been reported. This thesis will develop a prognostics method to provide advance warning of the failure of PPTC fuse and predict the remaining useful life of it. Cheng and Pecht [8][9] defined that PHM is an enabling discipline consisting of technologies and methods to assess the reliability of a product in its actual life cycle conditions to determine the advent of failure and mitigate system risk. PHM generally combines sensing and interpretation of environmental, operational, and performance-related parameters to assess the health of a product and predict remaining useful life. Traditionally, prognostics has been implemented by either a data-driven approach or a model-based approach. Gu *et al.* [50], Mathew *et al.*[51], Kumar *et al.* [52], and Pecht *et al.*[53] described these approaches and pointed out advantages and limitations of them.

Data-driven methods use current and/or historical data to statistically derive decisions and predictions about the health and reliability of products [9]. Based on the type of the data available, a variety of data-driven methods can be used. These methods can be classified as three categories: supervised, semi-supervised, and unsupervised. Data-driven methods use a training process to define the healthy behavior or baseline of products. The training process reveals patterns or relationships between parameters, such as correlation, covariance, residual, and inference patterns,

from the historical healthy data or the initial healthy state of the detected electronic product [9]. The data-driven method then compares the current monitored data with the baseline to determine the health of the electronic product and predict its RUL. Data-driven methods do not require an understanding of complex failure mechanisms and damage assessment models. This advantage enables the data-driven methods to be used for the prognostics of complex products that have multiple complex failure mechanisms. There are many data-driven methods, such as autoregressive integrated moving average (ARIMA) developed by Box *et al.* [54] and demonstrated by Ho *et al.* [55][56], neural networks (NNs) shown by Xu *et al.* [57], support vector machines (SVMs) developed by Vapnik *et al.* [58], and demonstrated by Pai *et al.* [59], and Chen *et al.* [60], decision tree classifiers, used by Kuo *et al.* [61], and Freund *et al.* [62] on reliability prediction, principle component analysis (PCA), used by Choi *et al.* [63], and Cho *et al.* [64] on the fault detection, particle filtering (PF) used by Xu *et al.* [65], and Zhang *et al.* [66] on detection and prediction, and fuzzy logic used by Yadav *et al.* [67] on reliability improvement estimation, etc. However, the data-driven methods are dependent on the training data. If the training data does not contain the entire range of the healthy behavior of the product, or if the training data contains any degradation of the product, missed or false alarms may be generated. The data-driven method cannot distinguish between different failure modes or mechanisms.

Pecht [9] stated that PoF methods utilize knowledge of a product's life cycle loading conditions, geometry, and material properties to identify potential failure mechanisms and estimate its remaining useful life. The advantages of the PoF method

include that providing the estimate of damage for given loading conditions and failure mechanisms; identifying the components which are critical to system reliability; estimating remaining life for different loading conditions, as long as the failure mechanisms and accelerated factors are identified; predicting the remaining life even in non-operating conditions. Several examples about PoF methods were shown by Gu *et al.* [68][69] and Mishra *et al.* [70]. However, it is difficult to estimate RUL using the PoF method if the failure mechanisms or models are unavailable. Sometimes, although the individual failure mechanisms are identified, dealing with the interactions between different failures mechanisms is still a challenge for the PoF method. Models with a combination of failure mechanisms are much more complicated than simply being the sum of the individual failure mechanisms.

Selection of different data-driven methods depends on the features of data. For example, if the data is purely linear, ARIMA model may be suitable for the prediction; if the data is nonlinear, the NN and support vector regression (SVR) may be proper. These models can forecast the future value of the data based on the regression of the historical data. The support vector regression (SVR) has some advantages compared with other non-linear forecasting method mentioned by Pai *et al.* [59], and Chen *et al.* [60]. However, SVR has rarely been used in the prediction for the reliability of electronics. Most of research showed how to improve the fitting on the observed data [71]-[73], not the actual application on prediction of data in the future.

2.6 Summary

Most of research on the PPTC polymer composites was focused on the physics of the conductivity and the electrical characteristics under different materials, contents, and structures of the fillers and polymers. Different models used to interpret the PPTC effects and behaviors were developed although none of them can explain all observed phenomenon.

Prognostics and health monitoring of the PPTC devices have not been developed and reported. Failure precursors that can indicate the anomalies or failures of the PPTC resettable fuse have not been determined. Although White et al [49] reported that resistance after reset and the trip time changed before and after tests, he did not monitor these parameters continuously so that the comparison only before and after a test did not reveal the trends of the parameter changes and could not draw a conclusion about the precursors. The causes for the degradation and failures of PPTC resettable fuses as a component, which includes different parts, have not been analyzed. The reactions of different parts of the PPTC resettable fuses were not considered for the degradation or failures of PPTC resettable fuses. Anomaly detection and failure prediction of PPTC devices have not been reported. The failure mechanisms and models of the PPTC resettable fuses have not been determined and developed.

Chapter 3: Failure Precursors of PPTC Resettable Fuses

The potential failure precursor parameters are determined by a systematic method, failure modes, mechanisms, and effects analysis (FMMEA). A series of experimental tests are then conducted to verify the precursors by identifying the correlations among the parameters and the mapping between the observed failures and the parameters. The monitoring of these precursor parameters enables the implementation of prognostics methodologies to detect anomalies and predict the failure of PPTC resettable fuses.

3.1 Potential Failure Precursor Parameters of PPTC Resettable Fuses

It is necessary to understand the environmental and usage conditions, structures, materials and geometry of the PPTC resettable fuses to identify the potential failure modes, mechanisms, and effects. A radial through-hole PPTC resettable fuse, as shown in Figure 3, was used as an example to show the determination of the failure precursor parameters. The methodologies used in this thesis can be extended to any kind of PTC devices.

Figure 5 shows schematic cross-section image of the device shown in Figure 3. In general, radial through-hole PPTC fuses include conductive polymer composites, electrodes, and outside coating. Conductive polymer composite is generally manufactured as a thin sheet by mixing the non-conductive polymer (e.g., polyethylene) and conductive particles (e.g., carbon black), being placed in a mold,

and then being punched out from the mold. An electrode is used to conduct and control the flow of electricity and is typically composed of foils and leads. The foils are attached on both sides of the polymer sheet. One lead is connected to each foil by soldering. The dielectric coating provides protection for the outside of the device.

An example of the material sheet of different parts of the device, shown in Figure 3 and Figure 5 can be found in [74]. The operational temperature range of this PPTC resettable fuse is from -40°C to 85°C. The highest surface temperature is around 125°C. The fuse works in a trip-reset cycling way, or essentially a heating-cooling cycling way. Based on the conductive chain and thermal expansion model, device also works in a thermal expansion-shrink cycling way.

The potential failure precursor parameters can be identified by failure modes, mechanisms, and effects analysis (FMMEA). FMMEA is a methodology used to identify failure mechanisms and models for all potential failure modes of a product under its operational and environmental conditions. Figure 8 is a schematic diagram of FMMEA. More detail information can be obtained from Ganesan *et al.*[75], Pecht *et al.*[76], and IEEE standard 1413 [77]. Identification of the potential failure modes, mechanisms, and models can help to determine the potential parameters to be monitored and the locations where the sensors should be placed. A series of experiment may be needed to verify the precursor parameters.

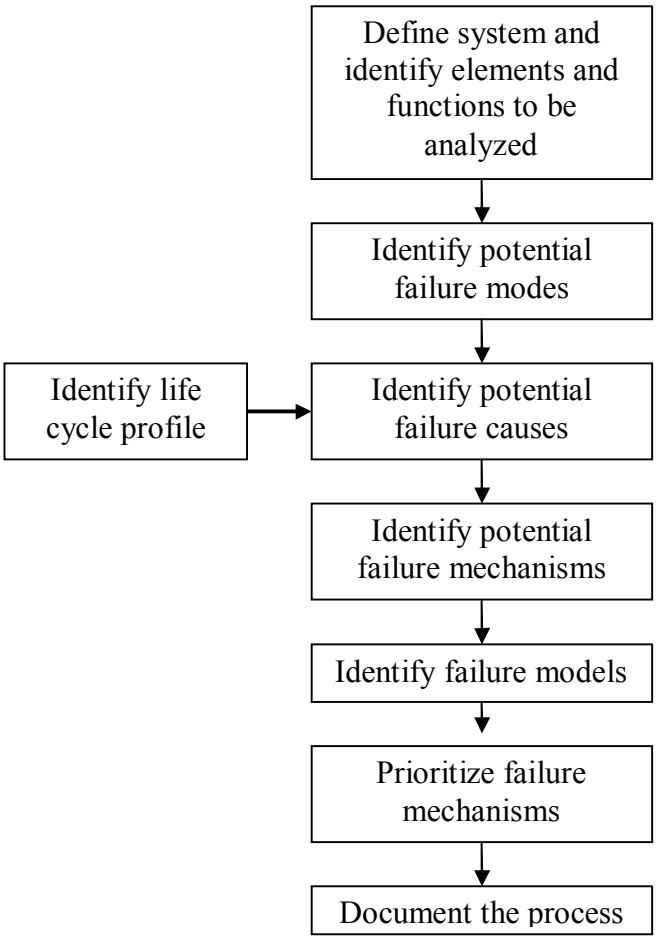

Figure 8: FMMEA process.

Table 4 shows the FMMEA results of the radial through-hole PPTC resettable fuse shown in Figure 3. Potential failure modes include abnormal trip behaviors, shifts in parameters, and physical cracks and gaps. The failure criteria should be defined based on related standards, specifications, and customers' requirements. In this thesis, a failure was defined as any of the following:

1) Fuse trips at less than normal current ($\leq I_{hold}$) at the specific ambient temperature.
2) Fuse does not trip at fault current ($\geq I_{trip}$) at the specific ambient temperature.

3) Deviations in the trip time of the fuse impact the typical operations of the circuit. The criterion of failure in terms of trip time is application-dependent. A trip in a longer time increases the risk of damage to the circuit because of the longer exposure of the circuit to a high fault current. A shorter trip time makes the circuit more likely to be disturbed by noisy currents, which may result in unnecessary faults in circuit operation. For example, when a motor changes its rotating direction, a high peak current may be generated. If the trip time of the fuse becomes too short, the high peak current will trip the fuse, stop the motor, and the operator must switch off and on the power to reset the fuse. In some cases, the designer of a circuit does not consider the reliability issues of the PPTC resettable fuse, and therefore does not design sufficient margin for trip time changes. For example, the circuit may be designed to allow a 20A fault current to pass through the circuit for 3 to 5 seconds when the trip time of the selected PPTC fuse is 4 seconds. If the PPTC resettable fuse degrades, the trip time may become shorter than 3 seconds or longer than 5 seconds. If the trip time of the fuse is shorter than 3 seconds, it will stop the operation of the circuit even for short peak current noise. If the trip time becomes longer than 5 seconds, it will damage the components in the circuit.

Table 4: FMMEA for PPTC resettable fuses
(Structured as Figure 3)

Potential Failure Sites	Potential Failure Modes	Potential Failure Causes	Potential Failure Mechanisms
Conductive polymer composite	Abnormal trip behaviors (e.g., trip at normal current, no trip at fault current)	Increase in the heat dissipation resistance, the cracks or gaps at the interconnections, the changes in the polymer properties, and the changes in the distribution of the CB particles.	Degradation of the polymer; aggregation of CB particles
Interconnection between foil and polymer composite	Shift in resistance and surface temperature	CTE-mismatch; gaps; manufacturing defects	Fatigue
Solder between lead and foil	Shift in resistance	Cracks	Fatigue
Outside coating	Cracks, separation with foil, shift in surface temperature	CTE-mismatch; deformation; manufacturing defects	Fatigue

4) A fuse becomes high in resistance after reset. One effect of the increase in resistance after reset is that it shortens trip time by generating more heat in the same amount of time. The other effect is that an increase in the resistance of the fuse decreases the voltage drops on other components, which may cause abnormal operation of the circuit.

5) Physical cracks, breaks, separations, and/or degradation in the outside coating. Fuses with these types of degradation may still function; however, the internal parts of the fuse will lose protection due to the degradation of

the dielectric coating. For example, moisture will corrode the electrode more easily. Furthermore, degradation of dielectric materials also causes a safety issue for the operators.

Potential causes of these failures include the degradation of materials include the increase in the heat dissipation resistance, the cracks or gaps at the interconnections, the changes in the polymer properties, such as the crystallinity, the changes in the distribution of the CB particles, and CTE-mismatch. Potential failure mechanisms include the degradation of the polymer, fatigue, and aggregation of CB particles.

Table 5 shows the potential precursor parameters based on the FMMEA results. In actual applications, the current through the fuse, the voltage across the fuse, and the surface temperature of the fuse can be monitored *in-situ*. The resistance during the trip can be calculated by Ohm theory using the monitored current and voltage. The resistance after trip can be measured by a data-logger using a 4-wire connection if the circuit is not too complex. Trip time can be calculated by the difference between the time when the fault current occurs and the time when the current decreases to the hold current. This can be measured by a current meter or sensors. Actual hold current cannot be monitored *in-situ* based on the test method defined in standard [6] but it can be measured when maintenance is being conducted.

Table 5: Potential failure precursor parameters

Potential Failure Precursors		Can be monitored *in-situ*?
Trip time		Yes
Resistance	Resistance after reset	Yes
	Resistance during trip	Yes (by measure current and voltage of the device during trip)
Surface temperature		Yes
Current	Current through the devices at normal condition	Yes
	Trickle current	Yes
	Actual hold current	No
Voltage across the device		Yes

3.2 Experiments and Results

In this thesis, the trip cycle tests and aging tests were designed to determine whether the trip time, current, resistance, and surface temperature are indicators of degradation in PPTC resettable fuses.

3.2.1 Trip cycle test

Referring to the manufacturer's specifications for the fuse [20], standards [6], and the requirements of customers, trip cycle tests were conducted for at least 6000 cycles at four different ambient temperature conditions, -10°C, room temperature (RT, 19-23°C), 60°C, and 85°C, respectively. Four samples were tested in each

condition, which was limited by our power supply. In each cycle, current through the fuse, voltage across the fuse, the surface temperature, trip time, and resistance in the resetting process (power switched off) of the fuse were monitored. The actual hold current was measured every 2000 cycles.

Figure 9 shows the setup of the trip cycle test. The Labview program was used to control a data logger and the VEE program was used to control a 4-channel power supply. Each channel of the power supply provided power to one PPTC resettable fuse. The fuses were placed inside a temperature chamber or air conditioning room to perform the trip cycle test under different temperature conditions. The temperature in the chamber was constant. The VEE program recorded the time stamp when the initial high current occurred and the time stamp when the current reduced to the hold current at ambient conditions, and then calculated the trip time of each trip cycle. After trip, the VEE kept controlling the power supply on for additional time, and then switched off it. An Agilent Data Logger 34970A was used to monitor the resistance in the resetting process and the surface temperatures of each fuse. A 4-wire connection resistance measurement was used to remove the effects of the wire and the connection. The surface temperature was measured by thermocouples, each of which was attached on each side of the fuse; the maximum temperature of these two thermocouples was used to determine the surface temperature of the fuse.

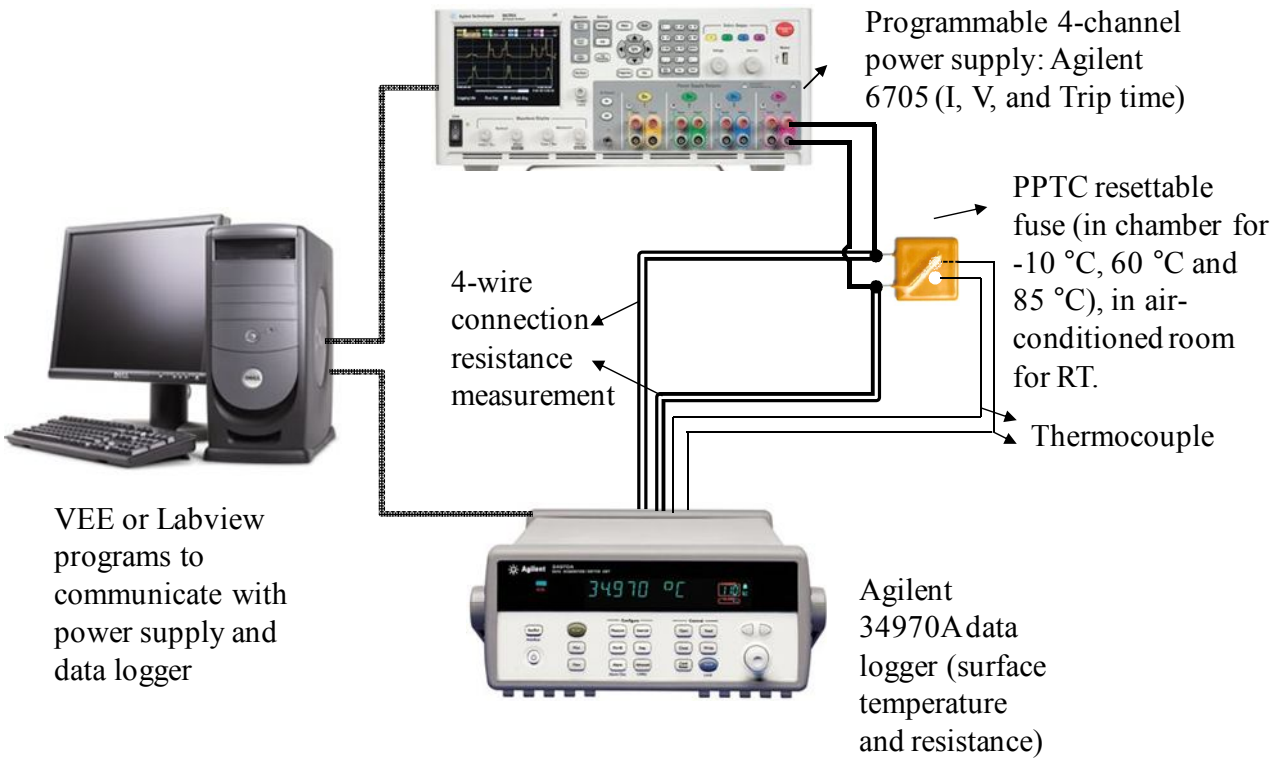

Figure 9: Trip cycle test setup

Figure 10 shows the current profile in one trip cycle. When the power was switched on, a high current was input to the fuse (20A for all conditions). The fuse was heated by Joule heat and tripped to a high resistance state in several seconds. When the current reduced to the specified hold current at the environmental temperature, power supply was kept on for 1 additional minute (called 1 minute trip endurance). After that, power was switched off for 7 minutes to cool the fuse and reset it to a low resistance state. Table 6 is the test matrix, which shows the input current the specified hold current. During each cycle, the fuses were tripped by the heating of fault current and reset by the natural cooling inside the chamber or under room condition.

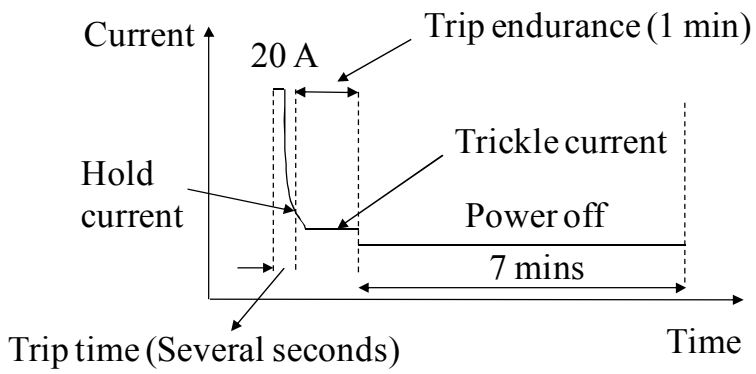

Figure 10: Current profile in one trip cycle (current vs. time)

Table 6: Trip cycle test matrix

Temperature	**Input Current**	**Specified Hold Current**
-10 °C (4 samples)	20A	4.8A
Room Temperature (RT, 4 samples)	20A	3.75A
60 °C (4 samples)	20A	2.4A
85 °C (4 samples)	20A	1.5A

3.2.2 Aging test

When the trip cycle tests were in process, aging tests were being conducted under the same environmental condition. Only the resistances were measured using data-logger via 4-wire connection. Table 7 is the matrix of the aging test. The objectives of the aging tests included the followings: 1) to investigate if the resistance of the PPTC resettable fuse changes with time under a constant temperature condition; 2) to compare the experimental and failure analysis results of the cycled

samples (in trip cycle tests) and non-cycled samples (in aging tests) under the same environmental condition.

Table 7: Aging test matrix

Temperature	Number of samples
-10 °C	8
RT	8
60 °C	8
85 °C	8

3.2.3 Results

Failures were observed in trip cycle tests. No failures were observed in aging tests. Observed failures in trip cycle tests includes damage to the coating of the device (cracks and gaps) and shifting in some of the performance parameters, such as trip time and resistance after rest. The failures are not hard failures that stop the functioning of the fuse, but soft failures that affect the performance of the fuses.

Figure 11 shows the examples of cracks and delimitation observed on the coating of the fuses after trip cycle tests under -10°C and RT conditions. These failures were not observed at any samples under 60°C and 85°C conditions. Figure 12 to Figure 14 show the shifting in the monitored parameters, including trip time, resistance after reset, and surface temperature with increase in number of cycles. Figure 15 shows the maximum resistance that the device can reach during the trip endurance. Each point in these figures is the average of the corresponding parameter values of every 100 cycles. Figure 16 shows the changes in the offline measurements

of hold current, which was conducted every 2000 cycles. Figure 17 shows the changes in the resistance collected by every half hour in aging tests. Table 9 maps all the observations in trip cycle tests and aging tests and the parameter shifting under all test conditions. Table 8 shows the correlation coefficients between different parameters.

Observed at all samples under -10 °C and RT conditions

Side view from left

Figure 11: Example of cracks and gaps

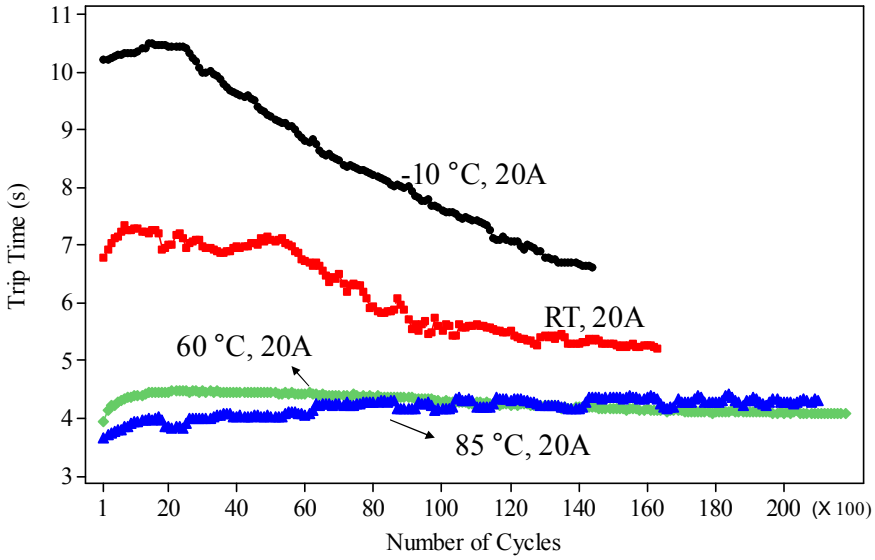

Figure 12: Trip time at different conditions
(Each point is the average of every 100 cycles)

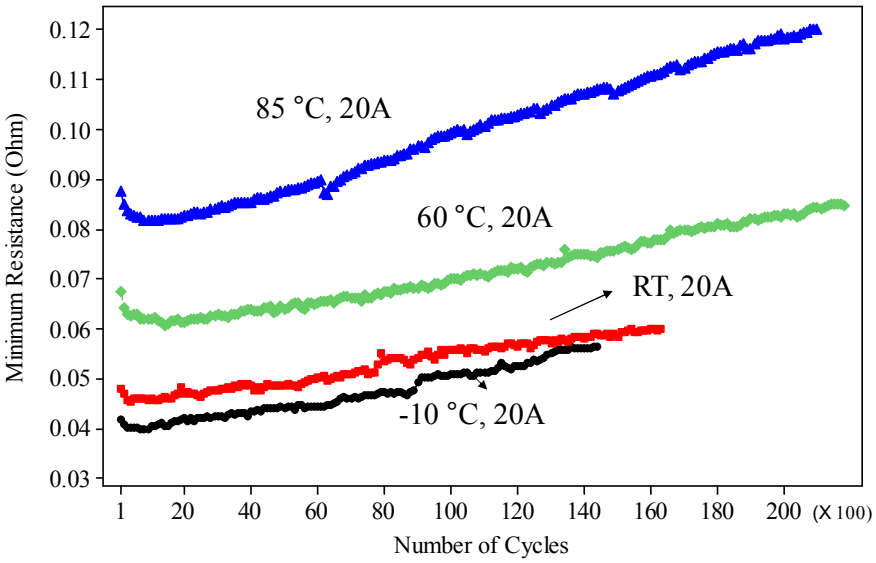

Figure 13: Minimum resistance after reset at different conditions
(Each point is the average of every 100 cycles)

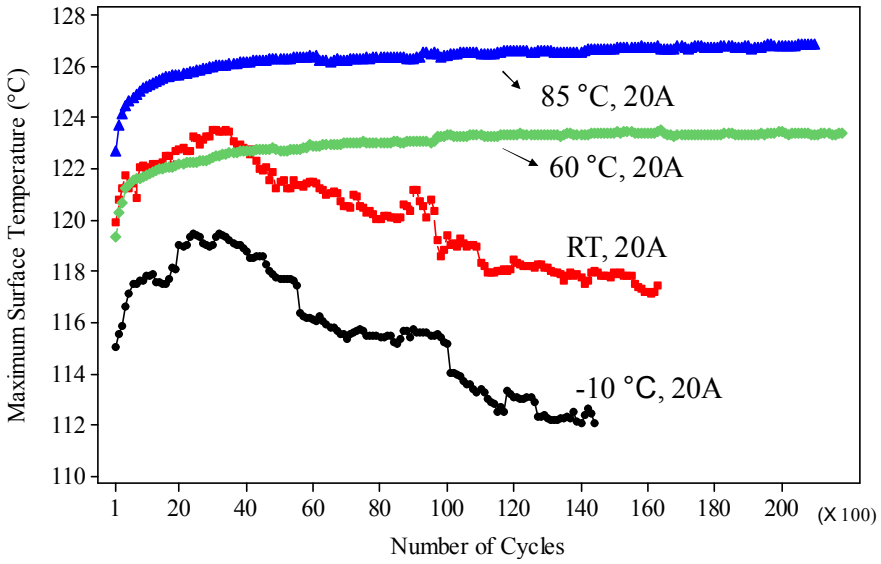

Figure 14: Maximum surface temperature at different conditions
(Each point is the average of every 100 cycles)

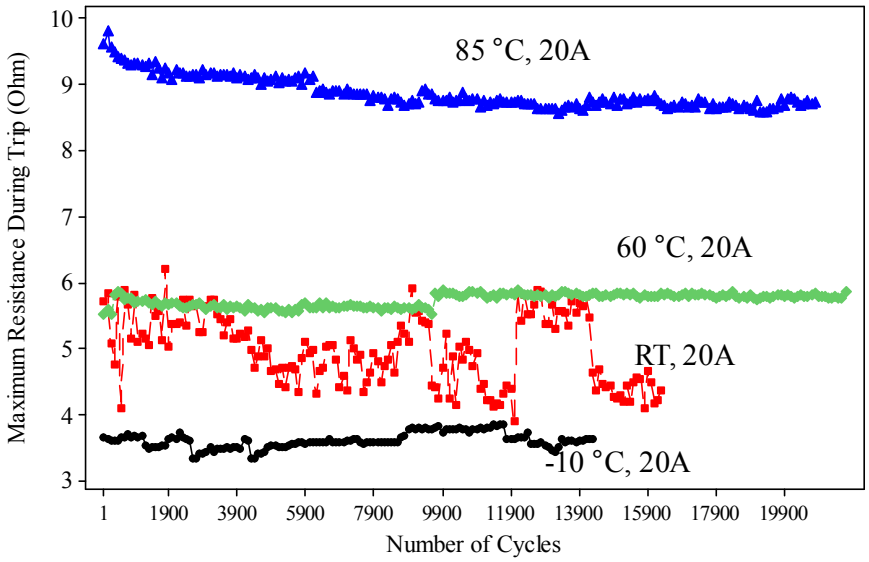

Figure 15: Maximum resistance during trip endurance at different conditions (Each point is the average of every 100 cycles)

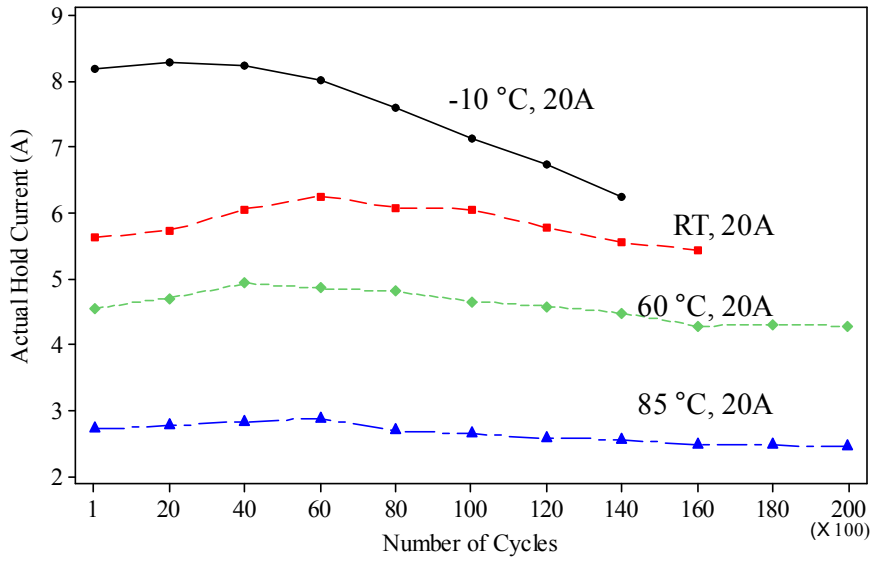

Figure 16: Actual hold current every 2000 cycles at different conditions

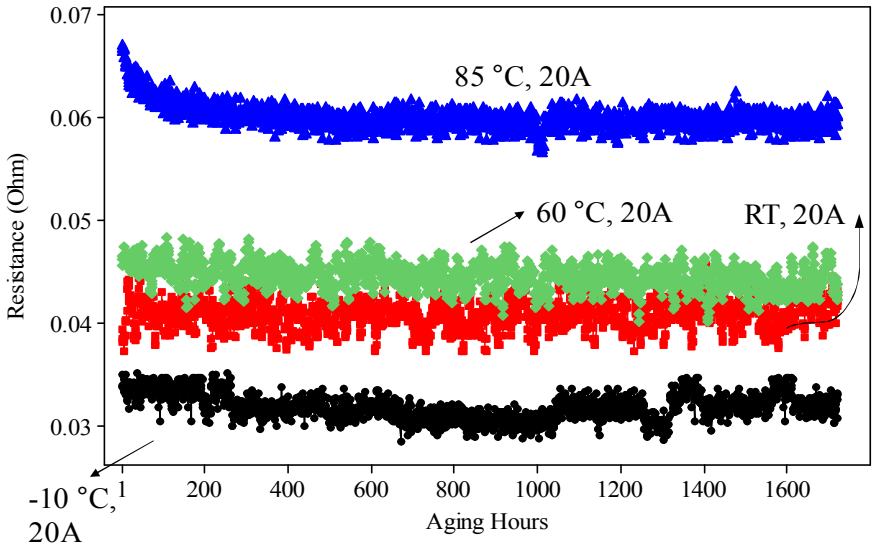

Figure 17: Resistance in aging tests at different conditions

Table 8: Correlation coefficients among parameters in trip cycle tests

Conditions	TT vs. MinR	TT vs. MaxST	MinR vs. MaxST	TT vs. MaxR	MinR vs. MaxR	MaxST vs. MaxR
-10 °C	**-0.97**	**0.92**	**-0.90**	-0.43	0.39	-0.43
RT	**-0.98**	**0.92**	**-0.93**	0.27	-0.32	0.36
60 °C	**-0.93**	-0.46	0.68	-0.33	0.37	0.41
85 °C	0.77	**0.85**	0.72	-0.36	-0.42	-0.46
	Trip time: TT, Maximum surface temperature: MaxST, Minimum resistance after reset: MinR, Maximum resistance during trip: MaxR					

Under -10 °C, RT, and 60°C conditions, decreases in trip times are correlated with the occurrences of cracks at coating or gaps between coating and foil (it was verified that internal gaps between coating and foil occurred in samples under 60°C condition). For 85 °C condition, the changes in trip time are correlated with the absence of cracks and gaps. Most importantly, trip time shows the decreases much earlier than observable cracks or gaps. This indicated that trip time is precursor for cracks or gaps.

Table 9 Summary of observations

Conditions	**Observable cracks or gaps**	**Changes in trip time**	**Changes in min. resistance after reset**	**Changes in max. surface temperature**	**Changes in actual hold current (every 2000 cycle)**	**Changes in (max. resistance or min. trickle current) during trip endurance**	**Changes in resistance in aging test**
-10 °C	Yes (around 4000 cycles)	Increased by **3%** in the first **2000** cycles, then decreased by **35%** of the initial value	Decreased by **7%** in the first **1000** cycles, then increases by **43%** of the initial value	Increased by **4%** in the first **3500** cycles, then decreases by **3%** of the initial value	Decreased by **24%** but still much higher than the value in mfr's specification **(6.5 vs.4.8A)**	No trends	No trends
RT	Yes (around 6000 cycles)	Increased by **7%** in the first **1000** cycles, then decreased from **5000** cycles by **24%** of the initial value	Decreased by **4%** in the first **1000** cycles, then increases by **28%** of the initial value	Increased by **3%** in the first **4000** cycles, then decreases by **2%** of the initial value	Decreased by 2% but still much higher than the value in mfr's specification **(5.8 vs.3.75A)**	Decreased and then recover	No trends

Conditions	**Observable cracks or gaps**	**Changes in trip time**	**Changes in min. resistance after reset**	**Changes in max. surface temperature**	**Changes in actual hold current (every 2000 cycle)**	**Changes in (max. resistance or min. trickle current) during trip endurance**	**Changes in resistance in aging test**
60 °C	No (after 22000 cycles, but internal gaps were identified by failure analysis)	Increased by **13%** in the first **1000** cycles, then decreased gradually	Decreased by **10%** in the first **2000** cycles, then increased by **27%** of the initial value	Increased sharply by **4%** in the first **1000** cycles, then gradually increased by **3%** of the initial value	Decreased by **6%** but still much higher than the value in mfr's specification **(4.5 vs.2.4A)**	No trends	No trends
85 °C	No (after 21000 cycles)	Increased sharply by **15%** in the first **2000** cycles, then no obvious changes	Decreased by **7%** in the first **1000** cycles, then increases by **38%** of the start value	Increased sharply by **3%** in the first **1000** cycles, then gradually increased by **3%** of the initial value	Decreased by **10%** but still much higher than the value in mfr's specification **(2.8 vs.1.5A)**	Gradually decreased and then recovered	No trends

Under -10°C and RT conditions, surface temperature shows similar trends with trip time, shown in Figure 12, Figure 14, and Table 8, it changes in small range and later than the changes in trip time. For 60°C and 85°C conditions, surface temperature changes are not obvious (less than 5%). Although trip time can provide most of the information that surface temperature can provide, we suggest surface temperature should be monitored to be assistance for trip time.

The increases in the trip time in the early period of experiment correlated with the decreases in the resistance after reset for all test conditions. This observation agrees with the principle of PPTC resettable fuses, in which the lower the resistance, the less heat is generated for the same input current, and the longer trip time is at the same ambient condition. After the early period, high positive correlation between the resistance after reset and the trip time was shown in the tests under -10°C and RT conditions. But weak correlation were observed for tests under the 60 °C and 85°C conditions, under which the resistance increased more than 30% of the initial value but the trip time showed no obvious changes (less than 5% of the initial value). This observation inferred that trip time changes were caused by not only the resistance changes but other impact factors, and the resistance changes may be not the dominant one. The increases in resistance affect the performance of other components in the circuit and can indicate other failures of the entire fuses, such as the defects in interconnections between different parts and the degradation of CB/PE polymer. Thus it is a failure precursor parameter. Other parameters, such as the highest resistance (or the minimum trickle current) during the trip endurance and the actual hold current, did not present obvious changes in the tests. Although the actual hold currents under -

10 °C, 60°C and 85 °C conditions have decreasing trends, it is much higher (more than twice) than the manufacturer specified hold currents. The correlation analysis among maximum resistance during the trip endurance and other parameters is shown in Table 8, which indicates that the maximum resistance during trip endurance has low correlation with others. Not enough evidences are observed to conclude that the highest resistance during trip endurance and the actual hold current are precursors at this stage. The resistance in the aging test does not change obviously, which showes that under normal aging conditions, the characteristics of the PPTC fuses are stable.

3.3 Summary

Trip time, resistance after reset, and surface temperature show high correlations with the observed failures, including the cracks at the coating, the gaps between coating and foil, and the performance shifting of the fuses. Changes in the trip time and the minimum resistance after reset affect the performance of the fuses directly and indicate the degradation of fuses. These parameters are failure precursors and must be monitored. High correlation between the trip time and surface temperature can simplify the post-analysis of the data. For example, it is enough to use trip time to predict the failure. But as a side-product of the performance of the fuse, surface temperature can be monitored to provide assistance information for trip time. Other parameters, including the maximum resistance during trip endurance and the actual hold current, did not exhibit obvious changes in all the conducted trip cycle tests. They are not considered as failure precursors at this stage. The resistances at aging tests under different conditions were stable thus were not failure precursors.

Chapter 4: Determination of Failure Causes

Failures including cracks, gaps and performance parameter shifting were observed in trip cycle tests. Determination of the causes of the failures helps to identify the actual underlying failure mechanisms, develop proper data-driven and physics of failure models to predict the failure, and improve the design and reliability in the future.

The PPTC resettable fuse includes polymer composite as a PTC functional component, foils, solders, electrodes, and outside coating materials. Degradation of any of them contributes to the performance degradation of the fuse. No literature has reported the cause analysis considering the entire resettable fuse. Potential failure causes of radial through-hole resettable fuses (shown in Figure 3) were identified by FMMEA and shown in Table 4. In this chapter, failure analyses considering all the parts of the fuse were conducted to determine the causes of the changes in trip time, resistance after reset, and surface temperature.

4.1 Failure Analysis Methods

Based on the potential failure cause analysis, some nondestructive and destructive analyses were conducted. First, heating process analysis (or surface temperature increase process) was conducted by infrared (IR) camera to investigate whether the heat dissipation changed after the trip cycle test. IR pictures were also used to identify the location of the internal gaps between different parts and to verify the effect of cracks and gaps on the changes in the surface temperature and the trip

time. The IR pictures were taken under RT condition. For each trip cycle test condition, one tested sample was picked for IR test without any cutting.

The destructive analyses included: 1) interconnection analysis in order to determine the effects of the defects at the interconnection on failures of the fuse; 2) CB/PE microstructure analysis in order to investigate the effects of the distribution of the CB particles on failures of the fuse; 3) CB/PE crystallinity analysis in order to investigate the effects of the crystallinity changes in PE on failures of the fuse; 4) CTE test on a new sample to investigate the CTE-mismatch. The destructive analysis 1), 2), and 3), were conducted on the cycled samples under each test condition. A fuse was cut to different small parts for different analysis, shown in Figure 18.

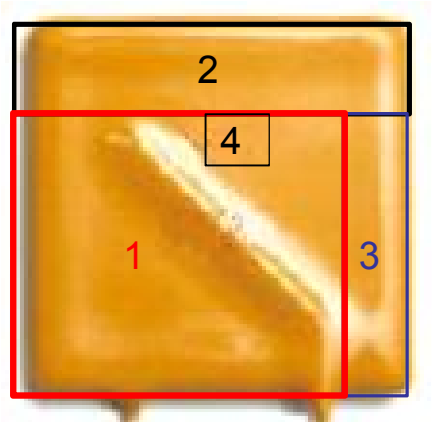

Figure 18: Different areas for different analyses

Area 1 was used for interconnection analysis to identify the cracks, voids, and gaps, which affect the mechanical, thermal, and electrical properties of the fuse. This area was cut from the fuse, cross-sectioned to different locations, and then investigated by environmental scanning electrons microscopy (ESEM). The concerned interconnections include those between coating and metal foil sheets, the

foil sheets and the leads, and the foil sheets and the polymer composite. Area 1 was also used to investigate the distributions of CBs in the polymer composite after some special process, such as ion etching by Argon ions, which can remove a thin layer of the PE and keep CB at its location. Aggregation of CB particles affects the conductivity of the polymer composite.

Area 2 and area 3 were used to investigate the microstructure. The parts were freeze fractured. In freeze fracturing process, parts were immersed in liquid nitrogen for 1 hour to become fragile and easy to break, and then were broken in the liquid nitrogen. The surface at the broken site then was coated with a thin layer of gold by sputter coater. Comparing with ion-etched surface, freeze fractured surface kept all components of the polymer composite. The gold-coated surface of the section was investigated by ESEM to identify the microstructure of polymer composite including the CBs and PE networks.

Area 4 was used to investigate the crystalline to amorphous (C→A) transition temperature and crystallinity of the polymer composite. These properties of the composite affect the heat required for the fuse trip. The polymer composite of this area was taken out and put into differential scanning calorimetry (DSC) to investigate the changes in C→A transition temperature and crystallinity. DSC is a technique for measuring heat capacity during a programmed change of temperature. Specific heat, which is the amount of energy needed to change the temperature of unit mass by unit degree at a constant pressure, was measured using a Pyris DSC. The specific heat curve measured over a wide temperature range shows how much energy is required to

the polymer phase transitions. For semi-crystalline polymers, the overall area of the transition peak increases with the degree of crystallinity, whilst its shape is determined by the crystal population present in the specimen. In DSC tests, sample was heated at 10 °C /min from 30 °C to 180 °C and then cooled at 10 °C /min to 30°C for 6 cycles.

CTE tests, using Pyris TMA 7, of coating material and the combination of the foil and CB/PE composite were conducted to investigate the CTE mismatches, which were the possible causes for the gaps between different parts inside the fuses.

4.2 Analysis Results

4.2.1 IR test results

Figure 19 and Figure 20 are the IR pictures of a new sample and a sample with cracks and gaps after cycle test under -10°C condition, shown in Figure 11. IR pictures reveal the presents and locations of the gaps between coating and foil, as well as the thermal distribution in the heating process. Table 10 summarizes the time needed to reach the heat balance for samples after cycle tests under different conditions. The tests results indicate that the samples, which have cracks and gaps, require longer time to dissipate the heat out. This means that the heat is kept inside for a longer time, and causes the faster heating of the internal CB/PE composite than that of the sample without cracks and gaps. This verifies that the gaps does cause the decrease in the trip time. Table 10 can also explain the reason of the a little increase in the trip time under 85°C, under which the heat dissipation is faster than the new

sample so longer time is needed to heat the sample up. All IR pictures are shown in Appendix A.

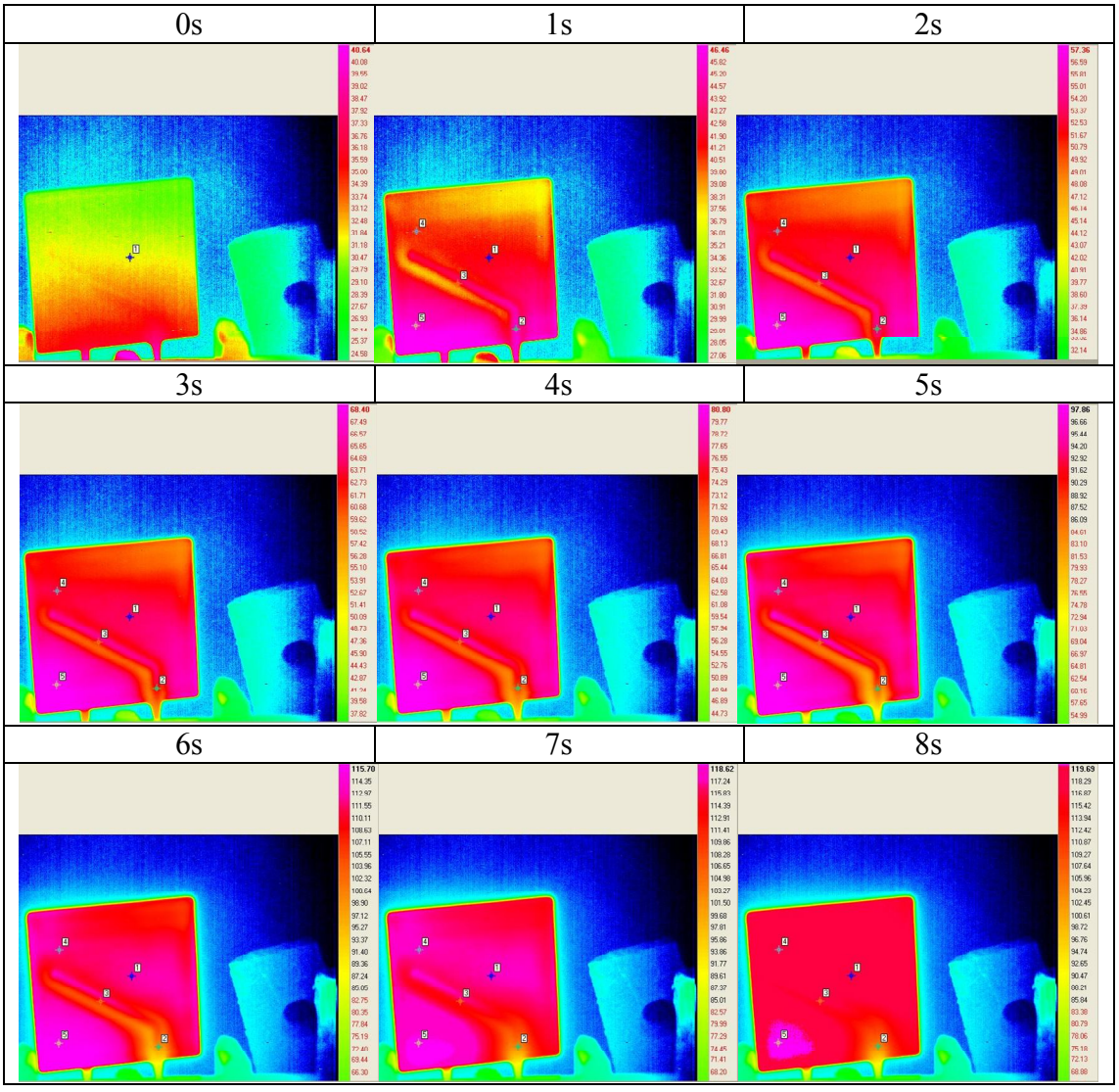

Figure 19: IR pictures at different moments (a new sample)

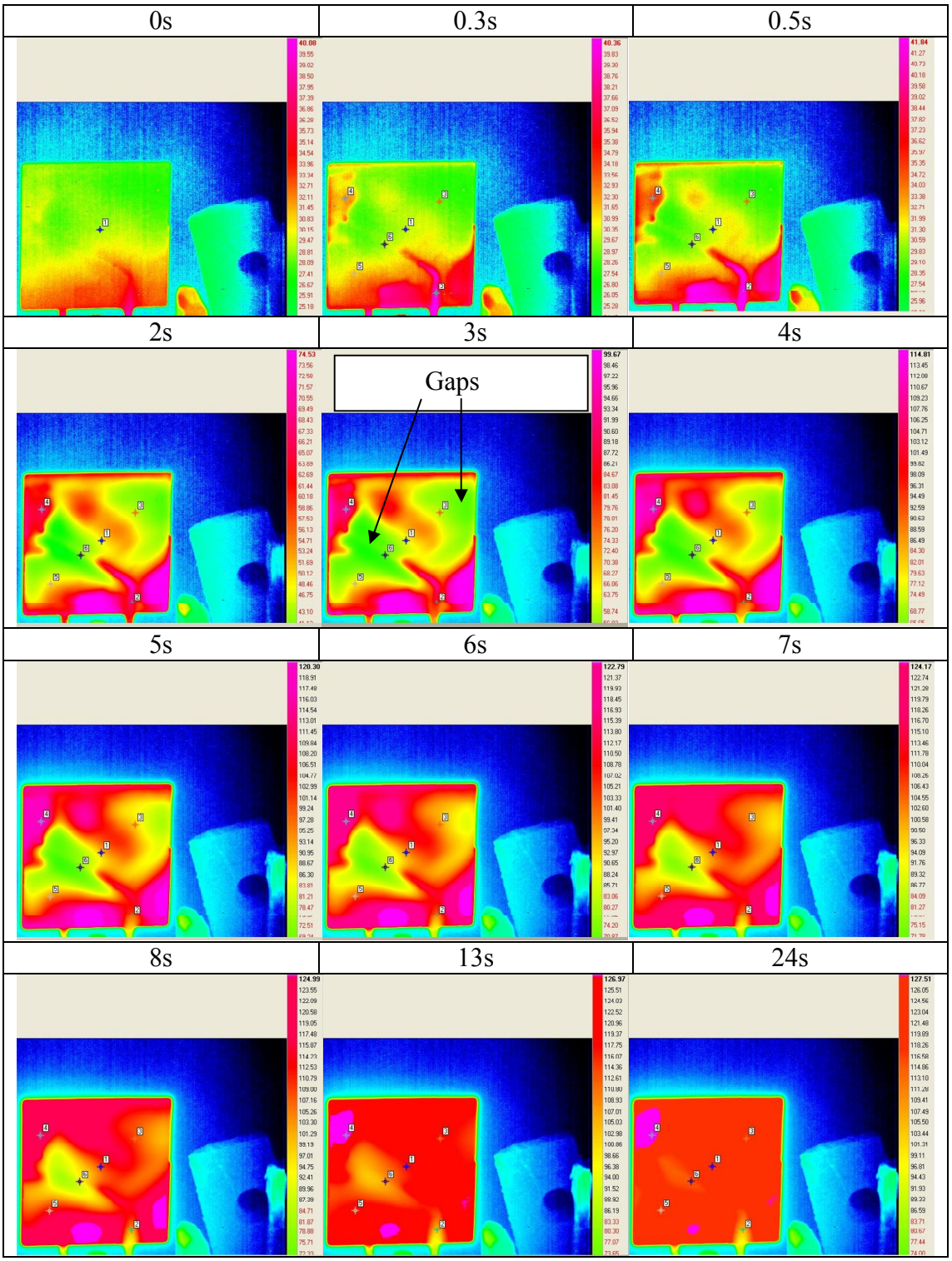

Figure 20: IR pictures at different moments (-10°C cycled sample)

Table 10: Time needed to reach heat balance

Conditions	Time needed to reach heat balance (s)	Cracks or gaps
New sample	8	No
-10°C	24	Yes
RT	15	Yes
60°C	7	Internal gap only
85°C	5	No

4.2.2 Interconnection analysis results

Figure 21 shows an example of new sample, in which no gaps and cracks were observed at all interconnections. Figure 11 shows an example of the observable cracks on the outside coating and gaps between coating and foil, which occurred at all the samples under -10 °C and RT conditions. Figure 22 and Figure 23 show examples of the internal gap between coating and foil, which occurred at all the samples under -10 °C, RT, and 60 °C conditions. Figure 23 to Figure 26 show examples of different type of cracks and voids at the solders, which connect the electrode with the foil. The cracks were observed in all the samples under -10°C and RT conditions. Table 11 summarizes the interconnection analysis results.

Table 11: Summary of interconnection analysis

Conditions	**Observable cracks and gap**	**Internal gap**	**Cracks at solder**
New	No	No	No

Conditions		Observable cracks and gap	Internal gap	Cracks at solder
Trip cycle tests	-10°C	Yes (around 4000 cycles, all samples)	Yes (all samples)	Yes (all samples)
	RT	Yes (around 6000 cycles, all samples)	Yes (all samples)	Yes (all samples)
	60°C	No (after 22000 cycles, all samples)	Yes (all samples)	No (after 22000 cycles, all samples)
	85°C	No (after 21000 cycles, all samples)		
Aging tests	No (all samples under all conditions)			

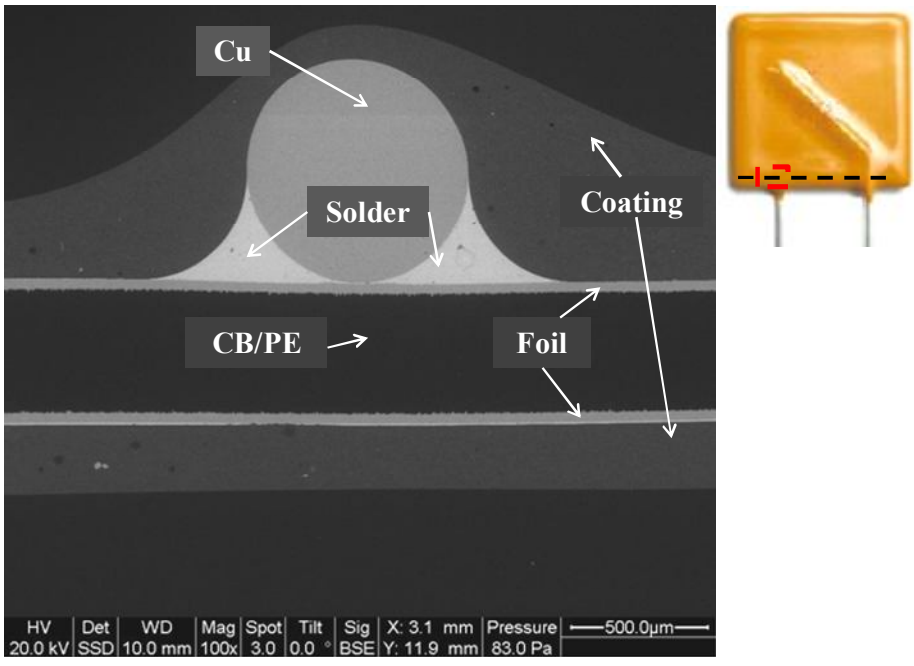

Figure 21: Normal interconnection (No cracks and gaps)

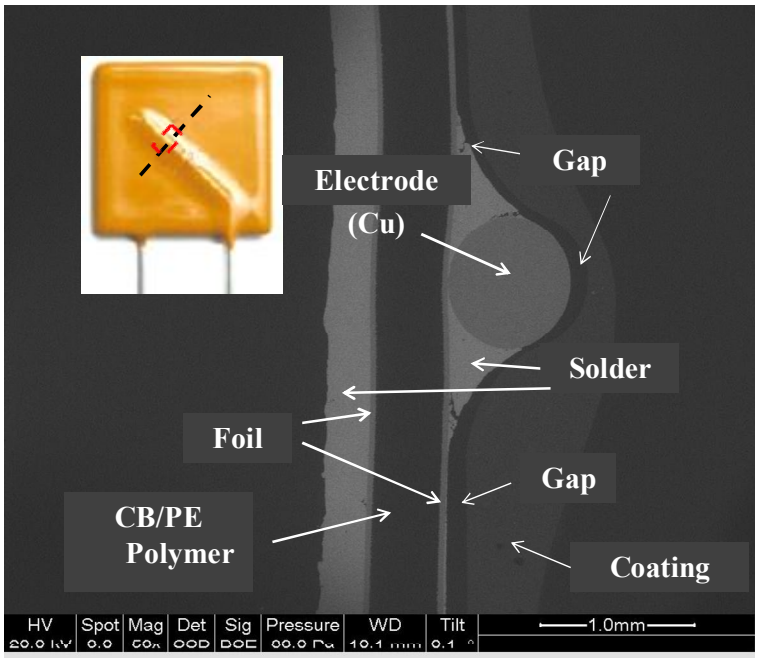

Figure 22: Example of internal gap

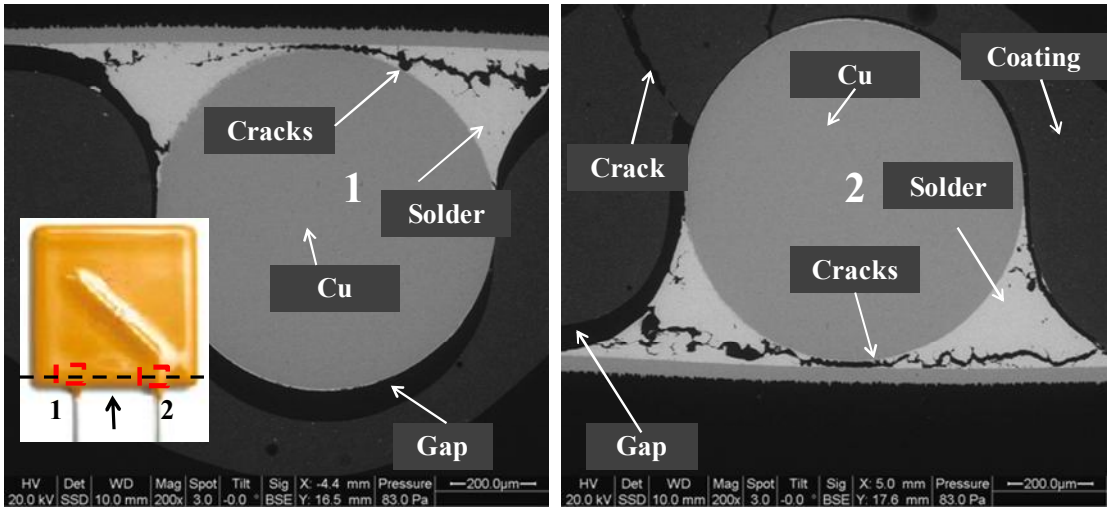

Figure 23: Example of cracks at solders and coatings; and gaps between coatings and electrodes

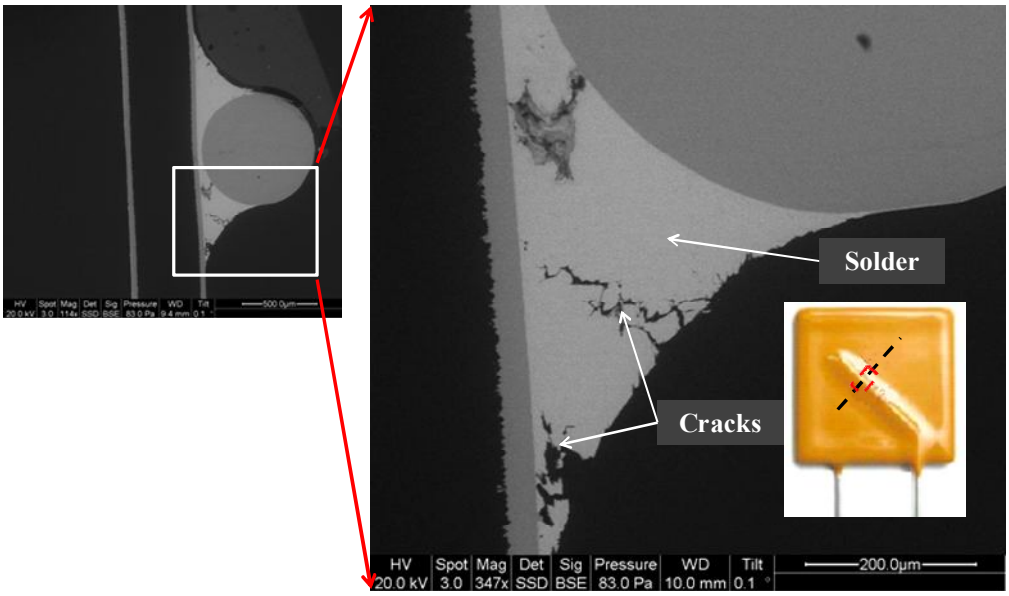

Figure 24: Example of cracks at solder

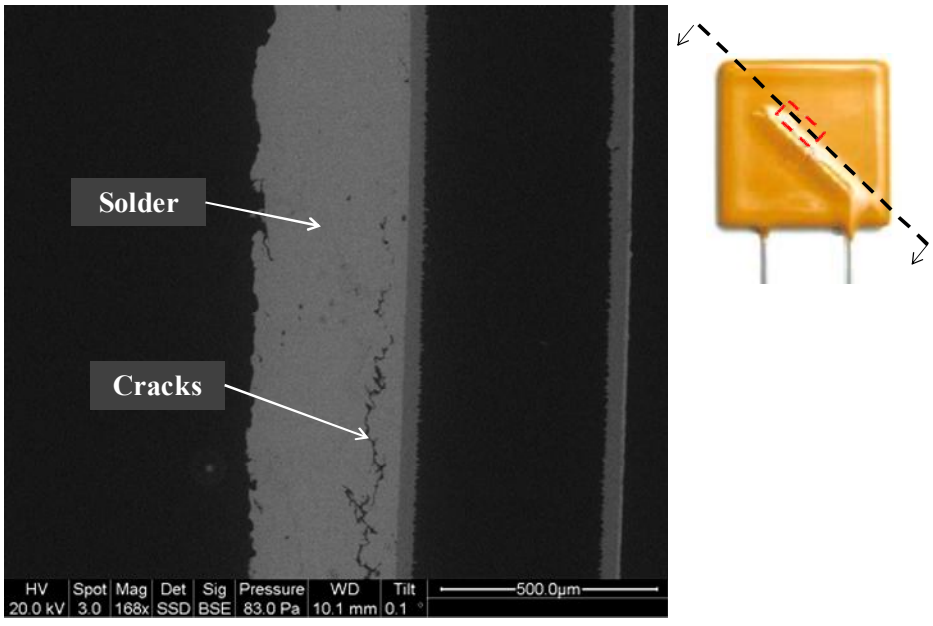

Figure 25: Example of crack along the solder

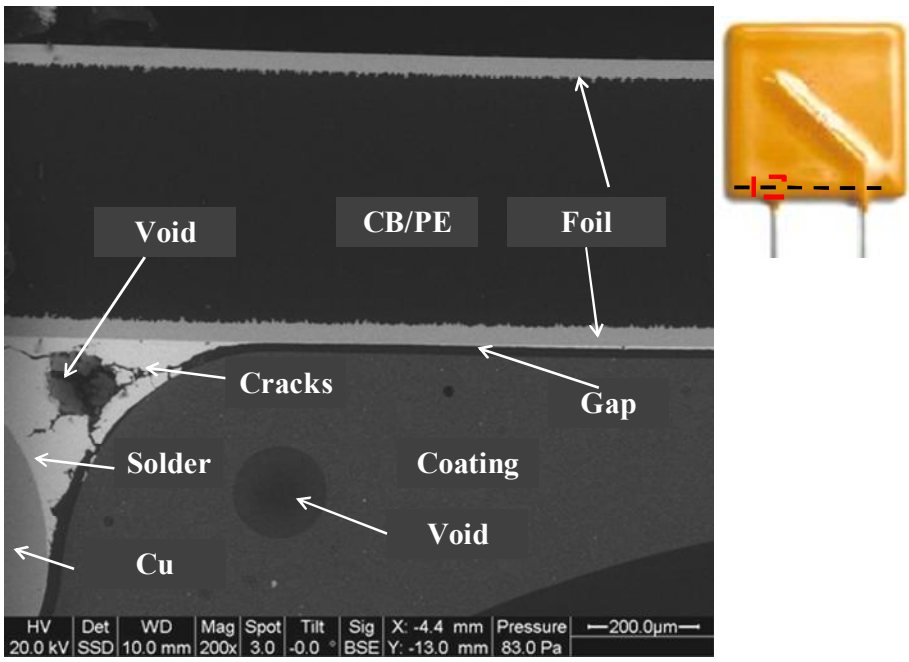

Figure 26: Example of voids and cracks at solder

4.2.3 Microstructure analysis results

Microstructure analysis revealed the distribution of PE and CBs. Figure 27 shows how CBs distribute in PE matrix in a normal case using freeze fracturing method. The CBs have trends to aggregate together. Figure 28 shows a typical microstructure of a sample under 60°C aging test, in which the CBs aggregated in a relative low level. Figure 29 shows a typical microstructure of a sample under 60°C trip cycle tests, in which CBs aggregated more and formed large agglomerations. All microstructure analysis results using freeze fractured method are shown in appendix A.

The analyses using ESEM after ion etching processing also observed the aggregates under different aging testing (non-cycled) conditions and agglomerations

of the CBs under different trip cycle test (cycled) conditions. Figure 30 shows a typical picture of a sample under 60°C aging condition using ESEM after etching by Argon ions. Figure 31 is atypical picture of a corresponding sample under 60 ° C trip cycle tests. All pictures of CBs aggregates and agglomerations under different conditions after ion etching are shown in appendix A.

Agglomeration of CBs affects the form of CB conductive paths. Although more conductive paths are formed in the larger agglomeration, the gap between different agglomerations increases. These agglomerations actually reduce the global conductive paths and increase the resistance. Table 12 summarizes the microstructure analyses.

Table 12: Summary of microstructure analyses

Conditions		CB Aggregates?	CB Large Agglomerations?	Resistance after reset
Trip cycle tests	-10°C	Yes	Yes	Increase
	RT	Yes	Yes	Increase
	60°C	Yes	Yes	Increase
	85°C	Yes	Yes	Increase
Aging tests	CB aggregates were observed for all samples; No CB agglomerations were observed			No obvious changes

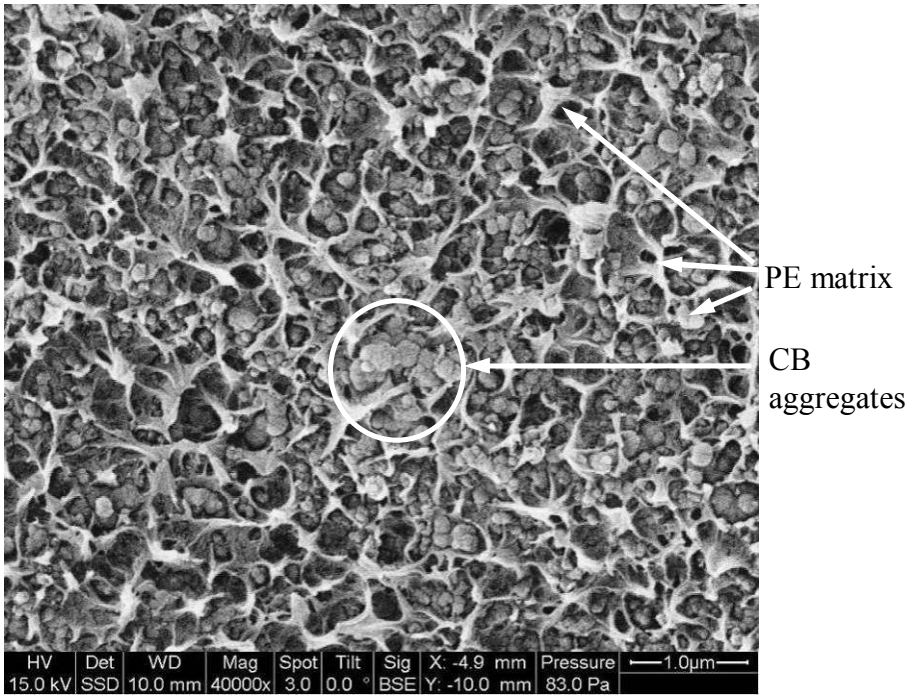

Figure 27: Microstructure of CB/PE composite of a normal sample (Sample was freeze fractured in LN_2)

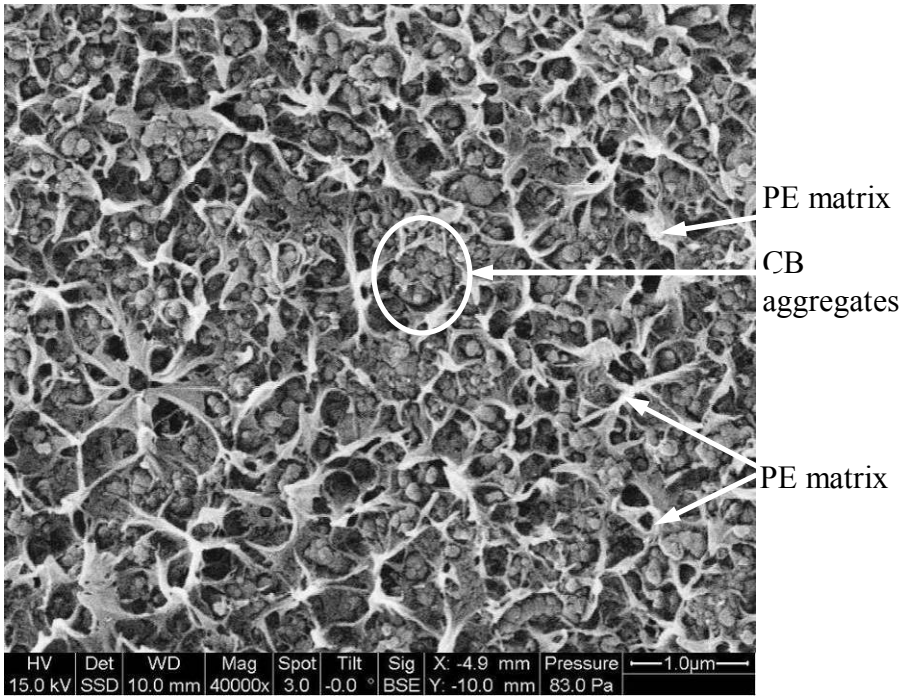

Figure 28: Typical CB aggregates of samples in aging test at 60°C (non-cycled, sample was freeze fractured in LN_2)

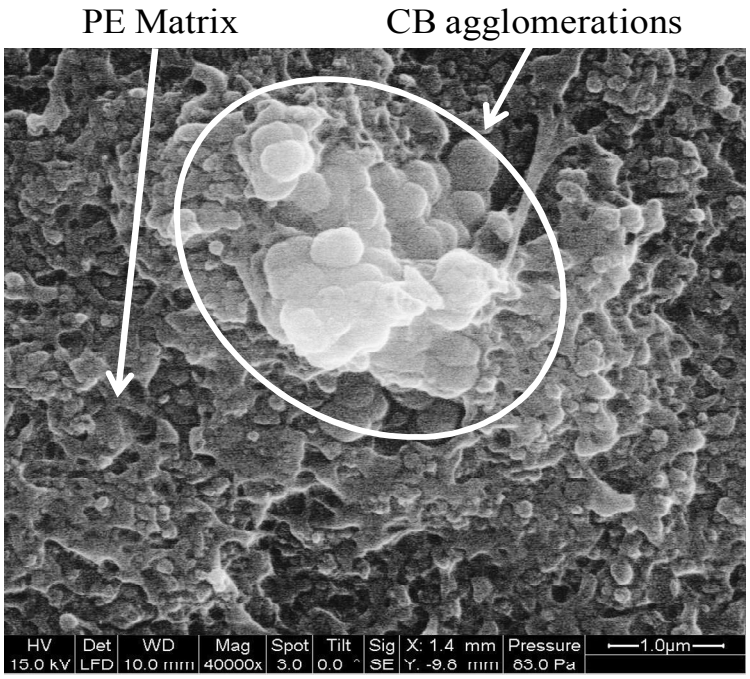

Figure 29: Typical CB agglomerations of samples in trip cycle test at 60°C (Sample was freeze fractured in LN_2)

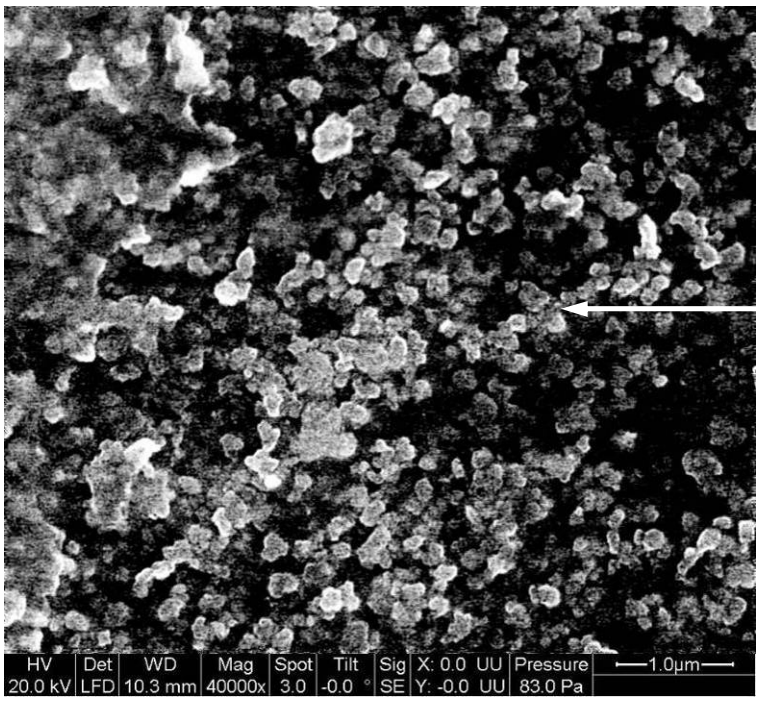

Figure 30: Typical CB aggregates of samples in aging test at 60°C (Non-cycled, sample was etched by Argon ions)

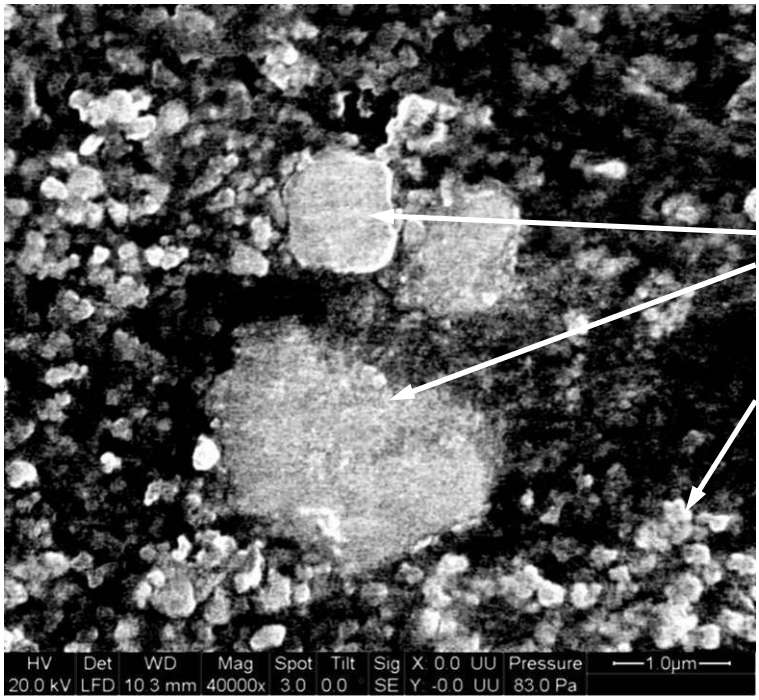

Figure 31: Typical CB agglomerations of samples in trip cycle test at 60°C (Sample was etched by Argon ions)

4.2.4 DSC analysis results

DSC tests revealed the changes in the thermal properties of the CB/PE composite, including the C→A transition temperature and crystallinity of the semi-crystalline PE.. Sample was heated from 30 °C to 180 °C at 10 °C /min and then cooled to 30°C at 10 °C /min for 6 cycles. The results showed that the first heating curve was different with those of the other 5, which were vertically identical. All the cooling curves were identical.

Figure 32 shows an example of DSC test results (only the first and the 6th cycle) of a sample after trip cycle test under RT condition. Table 13 summarizes the DSC test results and compares the C→A transition temperature and crystallinity between

the cycled samples and non-cycled samples (aging samples) under each ambient condition. The DSC result of the first scan contained the sample's thermal history including the heating/cooling cycles in the trip cycle tests and the temperature changes from experimental condition to room condition for sample preparation of DSC. We assumed that the thermal effects of sample preparations for all the samples were the same. The first scan then revealed the effects of trip cycle and aging tests on the thermal properties of polymer. Based on the results, all main C→A transition peak temperature of the cycled samples were higher than those of the aging samples. The percent crystallinity of the cycles samples were also a little higher than that of the aging samples. This indicated that the trip cycle increased the crystallinity of polymer. These results agreed with the results from some researchers. For example, Omastova *et al.* [78][79] conducted thermal cycle tests on polymer composite and found that the thermal cycles increased the crystallinity. The table also shows that the higher the ambient temperature, the higher the C→A transition temperature and crystallinity are. Since the highest temperature of the sample at different conditions is the same, under the natural cooling style, the higher the ambient temperature, the lower the cooling rate is. These results agreed with a results that the faster the cooling, the less crystallinity under RT is [80][81]. The increase of the crystallinity contributes to the increase of trip time because more heat is required for C→A transition. It also contributes to the decrease of resistance after reset because the less amorphous phase decreases the gaps between CB particles.

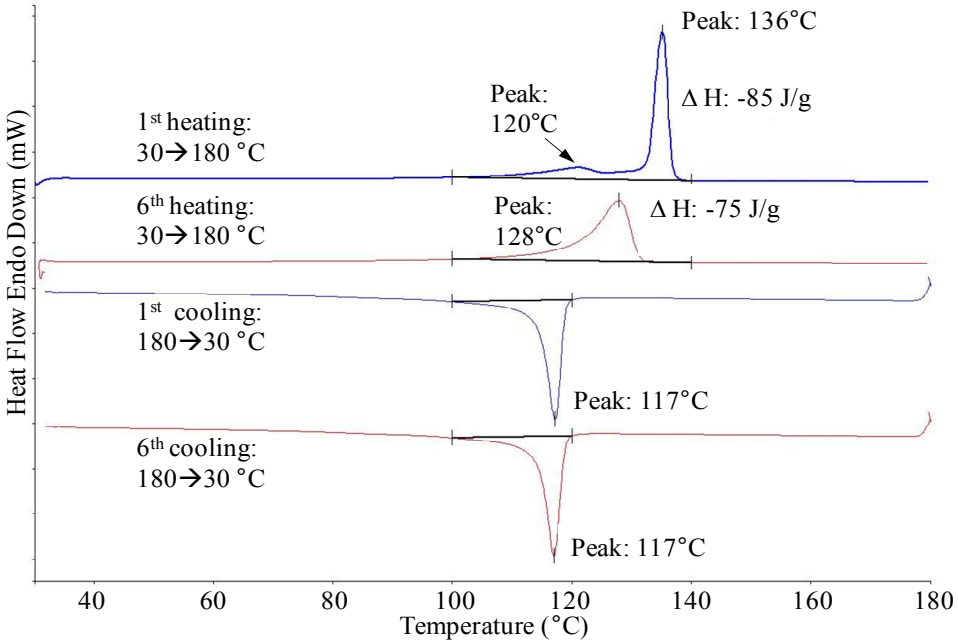

Figure 32: DSC curve of a sample under trip cycle test at RT

Table 13: Summary of DSC test

	MainPeak_1st heating (°C)		LowPeak_1st heating (°C)		MainPeak_6th heating (°C)		C%_1st heating (=$\Delta H_m/\Delta H_m^0$) ×100% ΔH_m^0=285.8 J/g		C%_6th heating (=$\Delta H_m/\Delta H_m^0$) ×100% ΔH_m^0=285.8 J/g	
	Aging	Cycle	Aging	Cycle	Aging	Cycle	Aging	Cycle	Aging	Cycle
-10°C	130	135	120	119	128	128	27%	29%	24%	25%
RT	130	135	119	120	128	128	28%	30%	26%	26%
60°C	132	136	119	120	128	128	28%	29%	26%	25%
85°C	133	137	120	119	128	128	29%	30%	25%	25%
							ΔH_m and ΔH_m^0 are C-A transition enthalpies of sample and 100% crystallization sample			

4.2.5 CTE test results

The CTE at *X* and *Z* directions of outside coating and the combination of the foil and polymer, shown in Figure 33, were measured using Pyris TMA 7. The temperature range is from -10 °C to 140 °C by 5 °C/min.

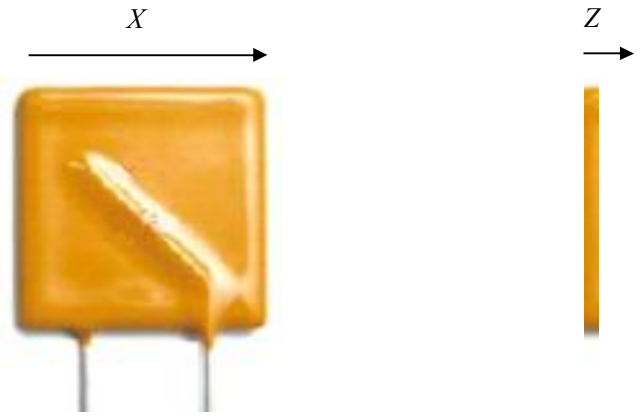

Figure 33: CTE test direction

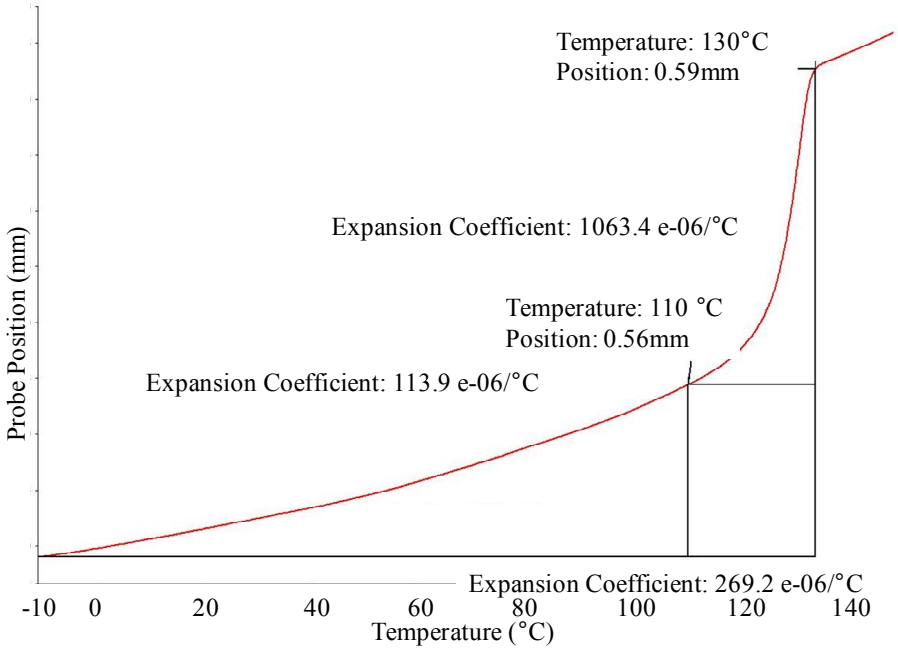

Figure 34: Example of CTE test (foil/polymer, *Z* direction)

CTE tests showed non-linear expansion at both *X* and *Z* directions. Figure 34 is an example of the test curve of the combination of foil and polymer (foil/polymer) at Z direction. Table 14 summarizes the CTE test results. CTE in temperature range from -10°C-110°C and range from 110°C -130°C were calculated individually, and then the overall CTE were calculated at range from -10°C -130°C. At *Z* direction, CTE-mismatch between coating and the foil/polymer combination were high at temperature range from 110°C -130°C, in which the C→A transition occurred and finished. At *X* direction, the CTE-mismatch was not that obvious. CTE-mismatch is one of the causes of the gaps and cracks shown in the interconnections.

Table 14: Summary of CTE test

	CTE (E-06/°C)					
	X direction			*Z* direction		
Temperature range	-10°C-110°C	110°C -130°C	-10°C - 130°C	-10°C-110°C	110°C -130°C	-10°C - 130°C
Coating	38.6	-105.4	20.6	105.4	-294.5	48.6
Foil and CB/PE	20.2	-12.3	18.9	113.9	1063.4	269.2

4.3 Causes for Changes in Parameters

Table 15 shows the mapping of the changes in parameters (trip time and resistance after reset) and the failure analysis results. The causes for the changes in

the parameters can be determined based on this mapping and some theoretical analysis.

4.3.1 Causes for changes in trip time and surface temperature

Trip is caused by the PPTC effect when the temperature is increasing to a certain level. Trip time is affected by changes in the PTC effects and the rate of the temperature increase. PPTC effect is controlled by the properties of the CB/PE composite itself, such as the crystallinity of the polymer, which affects the heat required for phase transition, and the aggregation of the CBs, which affects the resistance changes. Increase in temperature is controlled by a heat transfer equation (1), and finally heating and dissipation reach to a balance shown in equation (2).

$$\underset{1}{mC_p(\Delta T/\Delta t)} = \underset{2}{I^2R} - \underset{3}{U(T-T_A)} \tag{1}$$

$$I^2R = U(T-T_A) \tag{2}$$

Where m = mass of the fuse, C_p = heat capacity of the fuse, ΔT = change in fuse temperature, Δt = change in time, I = current flowing through the fuse, R = resistance of the fuse, U = overall heat-transfer coefficient, T = temperature of fuse, T_A = ambient temperature. In equation (1), item 1 is the heat to raise the temperature of the fuse; item 2 is the generated Joule heat, which is the heat source; item 3 is the heat dissipated to environment. When the heat transfer reaches the balance, the all generated heat dissipates to environment, and temperature of the fuse does not increase any more.

Table 15: Mapping between changes in parameters and failure analysis results

	Trip time changes	Resistance after reset changes	Interconnection analysis results		CBs agglomerations	Time to heat balance (s)	Crystallinity compared with non cycled samples
			Gap	Cracks at solder		***New sample: 8s***	
-10°C	Increased quickly in the early period, and then decreased	Decreased in the early period, and then increased	Observable cracks and gaps	Yes	Yes	24	Increased
RT			Observable cracks and gaps	Yes	Yes	15	Increased
60°C	Increased quickly in the early period, and then decreased gradually		Internal gaps (observed by ESEM)	No	Yes	7	Increased
85°C	Increased quickly in the early period, and increased gradually		No gap found	No	Yes	5	Increased

The external influence factors for temperature increasing include the current passing the fuse, the ambient temperature, and heat dissipation rate around the fuse. Temperature increasing is also affected by some internal factors including the start resistance of in each trip cycle (or the resistance after the previous cycle) and the heat dissipation ability of the device itself. In my experiment, the external effects were assumed to be constant. Only the internal effects were concerned in this thesis.

Based on the analysis above and the mapping in Table 15, the causes for the trip time changes can be determined as the following:

1) The increase in the trip time in the early period was caused by the decrease in resistance at that time period and the increase of the crystallinity, due to which more heat was required for C→A phase transition.

2) The decreases in trip time after the earlier period were caused by the decrease in the heat dissipation ability due to the gaps and cracks at the interconnections between different parts. The increase of the resistance after reset contributed the decrease of the trip time but was not a dominant cause. The gaps between foil/polymer combination and coating were caused by the CTE-mismatch and the heating/cooling cycles.

3) The gradually increase trend exhibited at 85 °C was caused by the increase of the crystallinity and the increase of the heat dissipation ability.

Surface temperature is a side-product of the trip of the fuse. It was high correlated with trip time. The causes for the changes of these two parameters were the same.

4.3.2 Causes for changes in resistance after reset

Table 15 also shows the mapping between the changes in resistance after reset and the failure analysis results. Resistance after reset measured in the trip cycle test was the entire resistance of the fuses including the resistance of the CB/PE composite and the resistance of interconnections. Defects at the polymer and interconnection all contributed the changes in resistance after reset. The causes for changes in the resistance after rest included the following:

1) The early decreases in resistance were caused by the increase in the crystallinity. Based on some research by He *et al.* [38], Park [40], Hunag *et al.*[41], Xu *et al.* [43], and Yui *et al.* [45], the CBs sit in the amorphous phase in PE. The increase in crystallinity reduces the amorphous phases resulting in the increase in the resistance. Furthermore, no cracks at interconnections were observed in this period.

2) Cracks and gaps at the interconnections except for that between coating and foil contributed to the increases in the resistance after reset.

3) The formation of large CB agglomerations caused the increase in resistance. The local conductivity inside the agglomeration increases, but the conductivity between different agglomerations decreases due to the

increase in the gaps. The agglomerations increase the global resistance of the CB/PE composite.

4) With the trip cycles, the effects of crystallinity changes on the resistance were ignorable comparing with the effects by the cracks at interconnections and CB agglomerations in CB/PE composite.

4.4 Summary

The causes for changes in parameters were determined in this chapter. Gaps between different parts were the main causes for decreases in the trip time. Without gaps, the properties change of the CB/PE, such as the increases in crystallinity, were the main causes for the increase of the trip time. The agglomerations of the CBs were the one of the main causes for the increase in the resistance after reset. With the increases in the cycle numbers, the cracks at the solder and the gaps between foil and CB/PE composite will control the increases in the resistance and finally cause an open current. The further analysis by CTE revealed that the CTE-mismatch caused to the gaps between coating and foil/polymer combination.

Chapter 5: Anomaly Detection Using Cross Validation Sequential Probability Ratio Test (CVSPRT)

Trip time and resistance after reset were determined as precursors for gaps, cracks, and prosperity degradation of CB/PE composite, which have different failure mechanisms. Anomaly detection for PPTC resettable fuse should monitor and detect the abnormal behaviors exhibited in each of the precursor parameters. In this thesis, sequential probability ratio test (SPRT) is used to monitor the trip time and resistance after reset to detect the anomalies. The difficulty of model parameter selection for SPRT was solved by a cross validation method.

Sequential probability ratio test (SPRT) has been used in *in-situ* monitoring, anomaly detection, and decision making for electronics, structures, and process controls. For example, Gross *et al.* used SPRT to monitor anomalies in computer servers [83][84], and equipment in nuclear plants [85]. Pecht *et al.* [53] used SPRT to detect anomalies in BGA solders by monitoring the resistance in the temperature cycles. SPRT was also used as an anomaly detection algorithm for an ePrognostics sensor tag [86]. Sohn [87] applied SPRT to conduct a statistical damage classification of a system, such as automotive system based on monitored vibration signals. Stoumbos *et al.* [88][89] utilized SPRT to generate a statistical process control model to monitor the process changes.

However, because model parameters for this method, such as the system disturbance magnitudes, and false and missed alarm probabilities, are selected by users primarily based on experience, the actual false and missed alarm probabilities are typically higher than the requirements of the users. This chapter presents a systematic method to select model parameters for the sequential probability ratio test without the need of experience by using a cross validation method. The presented method can improve the accuracy of sequential probability ratio test by reducing the false and missed alarm probabilities caused by improper model parameters.

General anomaly detection using SPRT is shown in Figure 35. The training data, which are healthy data of the system, can be obtained from historic data or from the stable operational phases when the product is known to be healthy. Statistical features of the training data, such as the distribution, are extracted to create a detection baseline. In the detection procedure, *in-situ* monitored data is compared with the baseline sequentially using SPRT to detect the anomalies.

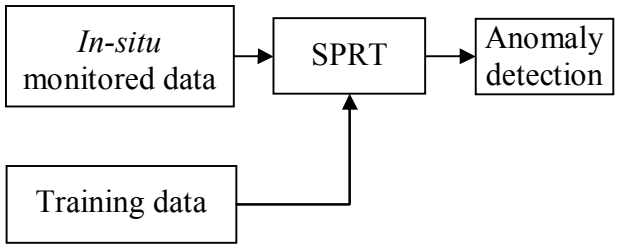

Figure 35: Anomaly detection procedure using SPRT

5. 1 Wald's SPRT

SPRT is a sequential statistical binary hypothesis test introduced by Wald [90]. SPRT is different from traditional hypothesis testing where the data collection is often

executed without analysis, and after all the data are collected analysis is conducted and conclusions are drawn [87]. In SPRT, data is monitored *in-situ* and is analyzed directly once it is collected. This ability enables SPRT for the detection of statistical changes against a null hypothesis at the earliest possible time or with the smallest sample size [90][91].

The binary hypothesis of SPRT includes one null hypothesis and one or more alternative hypotheses, shown in Figure 36. For a normal distribution, the null hypothesis H_0 represents the healthy state, with mean = 0 and standard deviation = σ; The alternative hypothesis includes four cases: 1) H_1: the mean of the test data has shifted high to $+M$, with no change in standard deviation; 2) H_2: the mean of the test data has shifted low to $-M$, with no change in standard deviation; 3) H_3: the variance of test data has increased to $V\sigma^2$, with no change in mean; 4) H_4: the variance of test data has decreased to σ^2/V, with no change in mean. M and V are the predetermined system disturbance magnitudes, which are decided by the user, and in general they are several times of the standard deviation of the training data.

Figure 37 shows the procedure of SPRT. The SPRT calculates the SPRT index for each *in-situ* monitored data point and compares the SPRT index with the boundary to make a decision. The SPRT index is the natural logarithm of the ratio of the probability that accepts the null hypothesis to the probability that accepts the alternative hypothesis. Four SPRT index formulas for normal distribution are shown as Equations (3) to (6) [92].

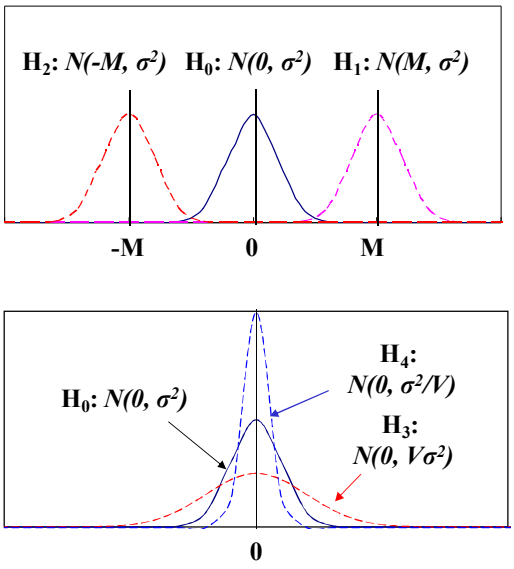

Figure 36: SPRT hypotheses

$$SPRT_1 = \frac{M}{\sigma^2}\sum_{i=1}^{n}(x_i - \frac{M}{2}) \tag{3}$$

$$SPRT_2 = \frac{M}{\sigma^2}\sum_{i=1}^{n}(-x_i - \frac{M}{2}) \tag{4}$$

$$SPRT_3 = \frac{\sum_{i-1}^{n} x_i^{\,2}}{2\sigma^2}(1 - \frac{1}{V}) - (n/2)\ln V \tag{5}$$

$$SPRT_4 = \frac{\sum_{i-1}^{n} x_i^{\,2}}{2\sigma^2}(1 - V) + (n/2)\ln V \tag{6}$$

SPRT uses the probabilities of missed alarms and false alarms to create the thresholds of acceptance and rejection of the null hypothesis, as shown in equation (7).

$$A = \ln(\frac{\beta}{1-\alpha}),\ B = \ln(\frac{1-\beta}{\alpha}) \tag{7}$$

Each SPRT index is compared to the decision boundaries *(A, B)*. For each comparison, there are three possible outcomes: 1) the lower limit is reached, in which case the healthy hypothesis (H_0) is accepted, the corresponding index is reset, and sampling continues; 2) the upper limit is reached, in which case the alarm is given,

the corresponding index is reset, and sampling continues; or 3) neither limit is reached, in which case the information is not sufficient to make a conclusion, and the sampling continues.

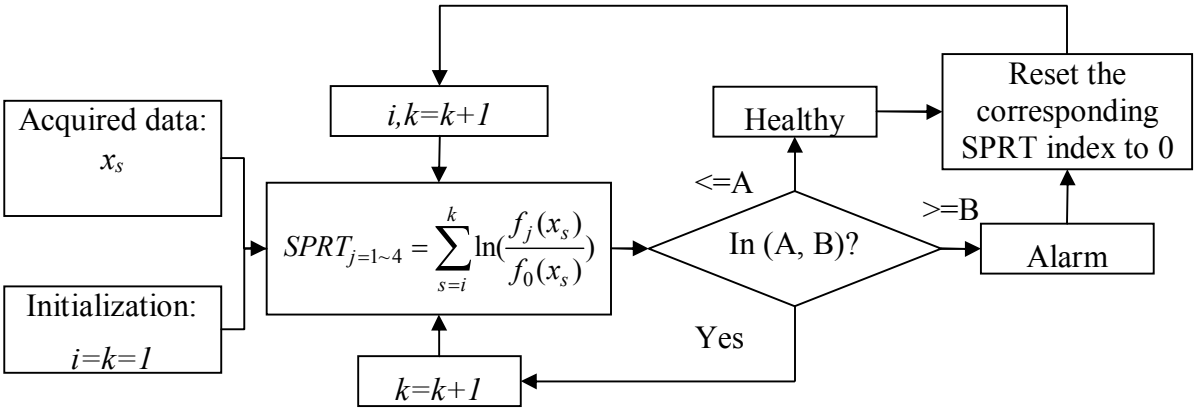

Figure 37: SPRT procedure

Four model parameters should be determined for SPRT detection: the system disturbance magnitude, M, which is m times the standard deviation of the training data; the variation factor, V; the false alarm probability, α; and the missed alarm probability, β. In practice, these model parameters are selected by experience. Even though the system disturbance magnitudes selected are in this recommended range [92] [93], the actual false alarm probability and/or missed alarm probability may be higher than the user-allowed values. Developing a systematic model parameter selection method for SPRT is necessary to improve its performance and control the false alarms and missed alarms. In this thesis, a cross validation method was used as a systematic method to select a proper model parameter set (m, V, α, β) for SPRT without the need for experience.

5. 2 Cross Validation SPRT

Cross validation (CV) is a statistical method that can be used to evaluate the performance of machine-learning-based anomaly detection and prediction algorithms. In the process of CV, the labeled dataset, which is a known healthy dataset, is partitioned into two subsets: a training subset and a validation subset [94]. Machine-learning-based anomaly detection and prediction algorithms are trained by the training subset and tested by the validation subset. The performance of the anomaly detection algorithms can be estimated by the error rate of the detection results compared with the validation subset, in which data is labeled as healthy or abnormal. The performance of the prediction algorithms can be estimated by the mean squared error (MSE) calculated by the difference between the predicted data and the validation data.

CV can also be applied to conduct the model parameter selection for anomaly detection algorithms [94] [95]. For example, it has been used to determine the number of neighbors of *k*-nearest-neighbor classification [96][97] and the number of hidden units for a one-layer neural network [98][99]. The performance of an anomaly detection algorithm with a certain model parameter can be calculated by error rate estimated by the CV process. The model parameter with which the algorithm has the lowest error rate is selected for the algorithm.

Common CV methods include hold-out CV, k-fold CV, and leave-one-out CV (LOOCV) [100][101][102]. In hold-out CV, labeled data is split into two independent subsets randomly: a training subset and a validation subset. For example, 30% of

labeled data are randomly picked up as validation data and the remaining 70% of the labeled data is training data. The anomaly detection error rate is calculated by equation (8).

$$E = \frac{Number of errors}{Number of\ data\ in the validation\ dataset} \tag{8}$$

Hold-out CV avoids the overlap between the training subset and the validation subset. But it does not use all the labeled data to validate the model, and the detection error rate estimation is highly dependent on how to split the dataset. *K*-fold CV can overcome some of these problems [101][102]. In *k*-fold CV, a labeled dataset is partitioned into *k* equally or nearly equally sized subsets. An iterative process is then conducted. In each iteration, a different subset is selected as validation data to estimate the performance of the algorithm, and the remaining *k-1* subsets are used as training data to train the algorithm. The detection error rate is calculated in each iteration using equation (9). The process is iterated *k* times until each of the subset has been selected as the validation data. After *k* iterations, *k* error rates are calculated. The mean of the *k* error rates, shown in equation (10), is considered to be the final detection error rate of the algorithm when the entire labeled dataset is used as the training data.

$$E_{vi} = \frac{Number\ of\ errors\ in\ the\ i^{th}\ iteration}{Number\ of\ the\ validation\ data\ in\ the\ i^{th}\ iteration} \tag{9}$$

$$E = \frac{1}{K}\sum_{i=1}^{k} E_{vi} \tag{10}$$

All the labeled data is used as validation data in k-fold CV; therefore, the accuracy of the detection error rate estimation is improved. However, with the increase of k, the variance of the detection error rate estimation becomes large, and the entire CV process is more time-consuming.

Leave-one-out CV (LOOCV) [102] is actually the extreme condition of k-fold CV, in which k equals to the number of data points in the labeled data, N. In each iteration, 1 different data point is selected as validation data and all the remaining data points are the training data. LOOCV runs N iterations, and the final detection error rate is estimated by equation (11). LOOCV can provide an unbiased estimation of the error rate, but the variance in the estimation is large.

$$E = \frac{1}{N}\sum_{i=1}^{N} Number\,of\,errors\ in\ the\ i^{th}\ iteration \tag{11}$$

The selection of the CV method can be based on the size of the labeled dataset. If the size is small, LOOCV can give unbiased error rate estimation. However, if the size of the labeled data is large, *k*-fold CV may reduce the computation time and maintain the accuracy of the estimation.

The model parameter set *(m, V, α, β)* for SPRT can be selected by *k*-fold CV. We recommend the range for each parameter as shown in Table 16. The procedure of model parameter selection by *k*-fold CV is shown in Figure 38. The first step is to select the training dataset, which is all healthy data and is the training data for SPRT after the proper model parameter set is obtained. After the training data is selected, a model parameter set *(m, V, α, β)* is assigned to SPRT. For each assigned model

parameter set, the actual false alarm probability *(α')* and missed alarm probability *(β')* are then calculated by *k*-fold CV.

Table 16: Range and change interval of SPRT model parameters

Parameter	Range	Start value	Interval
m	2 ~ 4	2	1
V	2 ~ 4	2	1
α	0.005 ~ 0.05	0.005	0.005
β	0.005 ~ 0.05	0.005	0.005

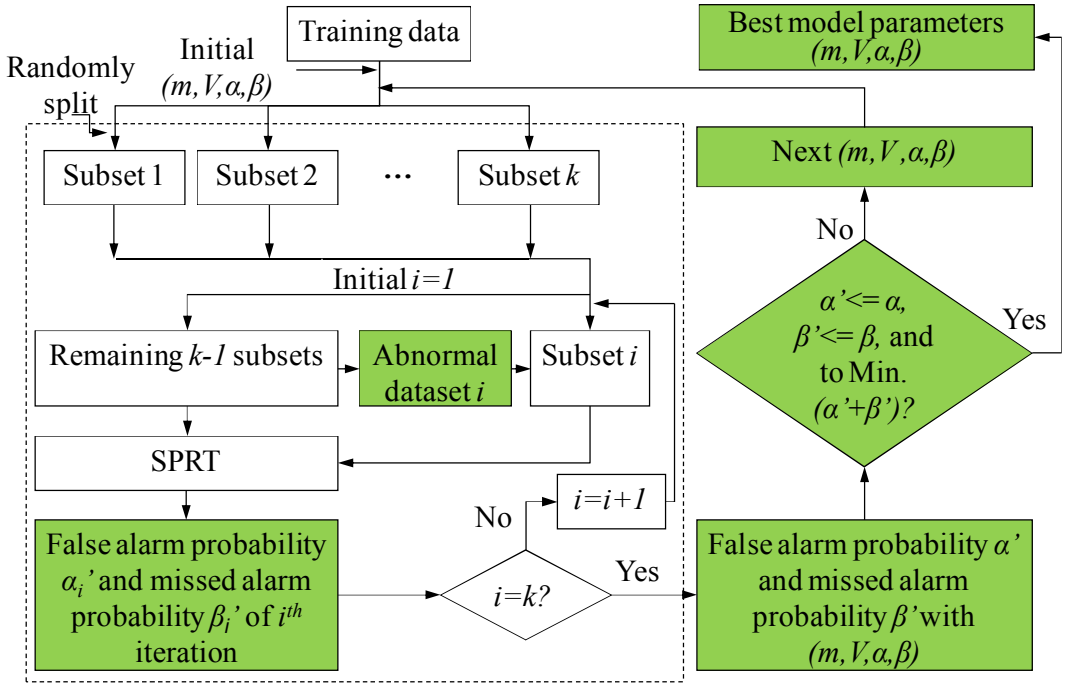

Figure 38: Model parameter selection procedure by k-fold CV

The total training data are partitioned into *k* subsets of equal or nearly equal size. *k* iterations should be conducted to calculate the actual false alarm probability *(α')* and missed alarm probability *(β')*. In each of the *k* iterations, one different subset is selected as the original validation data, and the remaining *k-1* subsets are the

training data. If SPRT is only run on the original validation data, which is all healthy data, only false alarm probability can be calculated. In order to calculate the actual missed alarm probability of SPRT, an abnormal dataset should be added into the original validation dataset, as shown in Figure 38 and Figure 39. The abnormal dataset can be generated by randomly picking up data outside of the range of [μ-$m\times\sigma$, $\mu+m\times\sigma$]. Here the μ and σ are the mean and standard deviation of the training data in each CV iteration (the remaining *k-1* subsets of the entire training data).

In each iteration, both false alarms and missed alarms can be identified based on the comparison of the detection results with the validation data and abnormal data. The false alarm probability and missed alarm probability can be calculated by equations (12) and (13). The process is repeated for k times until each of the subsets has been selected as the original validation dataset. The mean of the k false alarm probabilities and the mean of the k missed alarm probabilities are calculated by equations (14) and (15) as the final false alarm probability, *(α')*, and final missed alarm probability, *(β')*, when using the total entire training data (without the abnormal data).

$$\alpha_i' = \frac{Number\ of\ false\ alarms\ in\ i^{th}\ iteration}{Number\ of\ validation\ data\ in\ i^{th}\ iteration} \tag{12}$$

$$\beta_i' = \frac{Number\ of\ missed\ alarms\ in\ i^{th}\ iteration}{Number\ of\ abnormal\ data\ in\ i^{th}\ iteration} \tag{13}$$

$$\alpha' = \frac{1}{k}\sum \alpha_i' \tag{14}$$

$$\beta' = \frac{1}{k}\sum \beta_i' \tag{15}$$

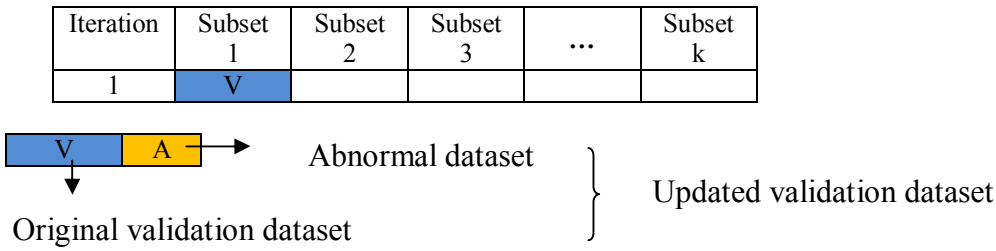

Figure 39: Adding an abnormal dataset into original validation dataset to calculate the missed alarm probability

The actual false alarm probability and missed alarm probability are compared with the ones in the selected model parameter set. If both the final false alarm probability and the missed alarm probability are less than the user-specified false alarm probability and missed alarm probability, respectively, the model parameter set is considered as a proper model parameter set for SPRT, but may be not the optimal model set. The optimal model parameter set can be defined as the one with the minimum error probability, which is the minimum sum of the false and missed alarm probabilities. If the criteria are not satisfied, another model parameter set based on the interval in Table 16 should be re-assigned and the performance of the SPRT with the model parameter should be evaluated by *k*-fold CV again. A model parameter set should be updated when the training data is updated since the actual false alarm and missed alarm probabilities are calculated based on the specific training data.

5. 3 Anomaly Detection Results of PPTC Resettable Fuses

As demonstrations, trip time and resistance after reset under -10°C condition were used individually for the anomaly detection by CVSPRT. Trip time was plotted in Figure 12, and resistance after reset was plotted in Figure 13. Training data should

be selected in the first step. It is proper to select the data in the early period as training data. The sequential changes in the data indicate the occurrences of failures. In this section, the first 20 TT data points in Figure 12, which represented the trip time values in the first 2000 cycles, were selected as training data for anomaly detection on trip time. The first 15 MinR data points in Figure 13, which represented the resistance after reset values in the first 1500 cycles, were selected as training data for the anomaly detection on resistance after reset.

The data may be normalized first using equation (16), where x_i' is normalized data, x_i is original data, and μ *and* σ are mean and standard deviation of the training data, respectively. The normality of the training data should also be checked using some tools. If the training data is not normally distributed, a transformation, such as the Box-Cox transformation [103] or the Johnson transformation [104], may be used to transform the data into normal distribution. Here the normalized training data was normally distributed.

$$x_i' = \frac{x_i - \mu}{\sigma} \tag{16}$$

Then the model parameters (m, V, α, β) were determined by the 5-fold CV process, in which an abnormal dataset with 20 abnormal data points, which were randomly generated out of the range of [μ-$m\times\sigma$, μ+$m\times\sigma$] were added into each validation set. Here the μ and σ are the mean and standard deviation of the training data (the remaining k-1 subsets of the training data). The updated validation data set is used to calculate the actual false alarm and missed alarm probabilities in each iteration.

After the 5-fold CV process, SPRT model parameter set (m=4, V=4, α =0.005, and β=0.01) was selected for trip time data under -10°C condition. SPRT then used these model parameters and the training data to detect the anomalies *in-situ* when a new trip time (TT) data was collected. Figure 40 shows the trip time anomaly detection results on trip time. Figure 41 is a plot of anomaly detection for the trip time when using a different model parameter set *(2, 2, 0.02, 0.01)*, under which some false alarms were detected in the training data. Similarly, after 5-fold CV process, model parameter set (m=3, V=2, α =0.005, and β=0.015) was selected for SPRT for the *in-situ* anomaly detection of the resistance after reset data. Figure 42 shows the final minimum resistance after reset (MinR) anomaly detection results. All the detection results are shown in table and the figures are shown in Appendix B.

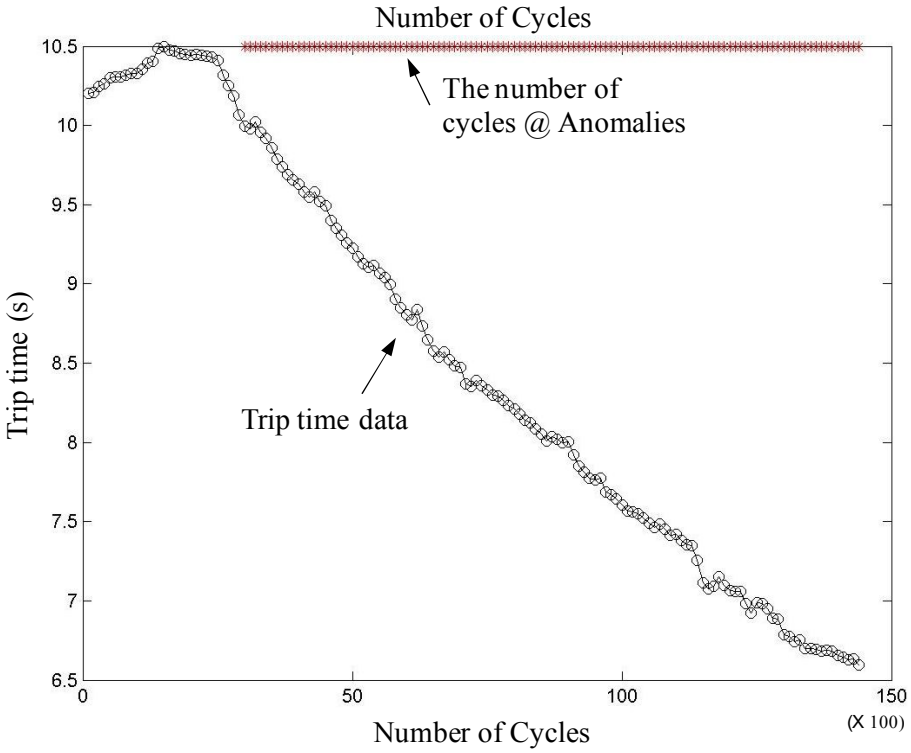

Figure 40: Anomaly detection on trip time under -10°C condition

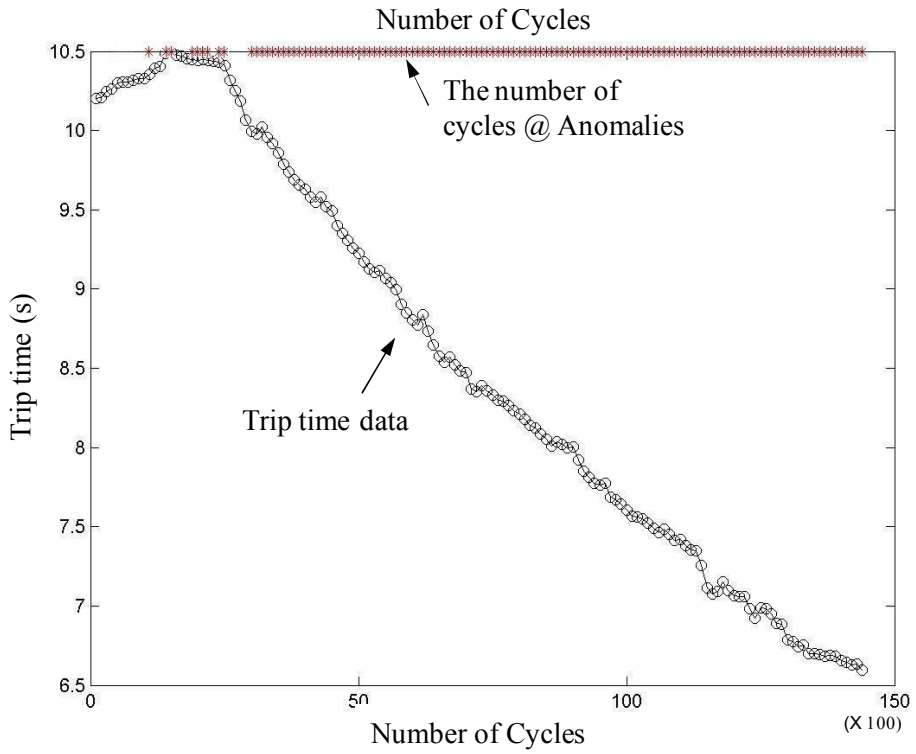

Figure 41: Anomaly detection on trip time under -10°C condition using model parameter (2, 2, 0.02, 0.01) (False alarms detected)

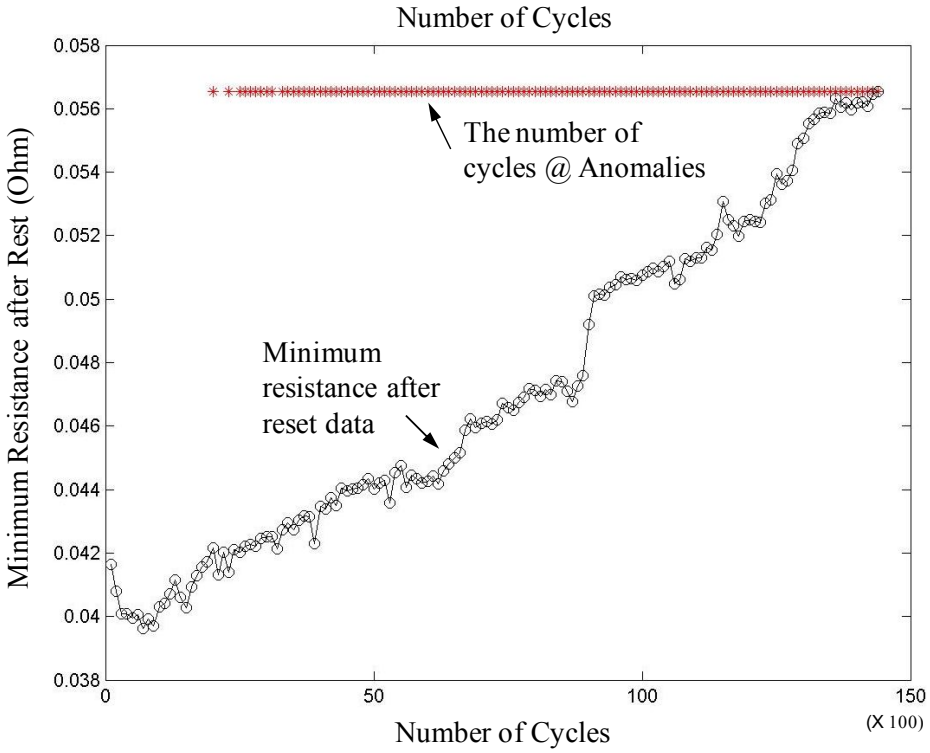

Figure 42: Anomaly detection on minimum resistance after reset under -10°C condition

Table 17 summarizes the anomaly detection results based on trip time and resistance after reset for all the trip cycle test conditions. The anomaly detection for the component should provide the times (cycles) and the corresponding parameters, which triggered the alarm. The earliest anomaly alarm among all the parameters was used to trigger alarm for the anomaly of the component.

Table 17: Summary of anomaly detection results

	Training data for TT	SPRT model for TT	First anomaly cycle for TT (x100)	Training data for MinR	SPRT model for MinR	First anomaly cycle for MinR (x100)	Earliest anomaly for the device (x100)
-10°C	1-20	(4,4,0.005, 0.01)	30	1-15	(3,2,0.005, 0.015)	25	25
RT	1-30	(4,2,0.005, 0.005)	61	1-30	(4,2,0.005, 0.005)	45	45
60°C	10-34	(4,4,0.035, 0.005)	47	7-24	(4,2,0.005, 0.005)	37	37
85°C	1-50	(4,2,0.015, 0.005)	65	1-20	(3,2,0.035, 0.005)	41	41

5. 4 Summary

CVSPRT is developed to select a proper model parameter set for SPRT without the need of experience, thus reduce the false alarm and missed alarm probability. Besides the anomaly detection for PPTC resettable fuses in this thesis, CVSPRT can be extended to conduct the anomaly detection for any conditions if the training data is available and the SPRT index can be calculated.

Chapter 6: Moving Window based Dynamic Model Parameter Optimization N-steps-ahead Prediction

Prognostics of PPTC resettable fuses can be implemented using data trending or regression methods on the precursor parameters directly. When any anomalies are detected by the methods developed in chapter 5, failure prediction should be implemented to provide the information in the future. In this section, a moving window based dynamic model parameter optimization (MW-DMPO) n-steps-ahead prediction method is developed first as a general method for dynamic data trending and then moving window cross validation support vector regression (MW-CVSVR) n-steps-ahead prediction method is developed as a case study for the prediction of the PPTC resettable fuses.

6. 1 Moving Window based Dynamic Model Parameter Optimization (MW-DMPO) N-steps-ahead Prediction

The fixed training data can not contain the latest degradation information, thus cannot generate the prediction with high accuracy. Training data for prediction modeling should contain degradation features as much as or as latest as possible. Moving window method has been developed as the method to update the training data. For example, Djukanovic *et al.* [105] used MW on neural network and Ren *et al.* [106] applied MW on autoregressive quadratic model for short-term forecasting. Pecht and Cheng [107] used MW techniques on data driven methods for prognostics

of aging systems. However, the model parameter parameters, which determine the performance of the trending models, were not updated with each updating of the training data using MW. This caused the prediction inaccurate, even though the MW method was used to update the training data to catch the latest degradation information. A MW-DMPO n-steps-ahead prediction method is developed in this dissertation to solve this problem.

The MW-DMPO n-steps-ahead prediction method is shown in Figure 43. Initial training data may be needed to transform to a certain pattern based on the requirement of the prediction model, and then used to train the prediction model, during the training process, best model parameters for the prediction model is identified by a model parameter optimization method. The n-steps-ahead predictions are calculated by the trained prediction model. N-steps-ahead predictions mean that only *n* values in the future are predicted in one prediction. If any of the n-steps predictions reaches the threshold, alarm is triggered and a failure is predicted. If all the *n* predictions do not reach the failure threshold, a conclusion should be drawn that the product will not fail in the future *n* steps (such as, times or cycles). And then the training data should be updated by a MW method to re-train the prediction model when the actual *n* observations are obtained to conduct the next n-steps-ahead predictions. Most importantly, for each training data updating, the model parameters should be optimized. That is called the dynamic model parameter optimization with each updating of training data.

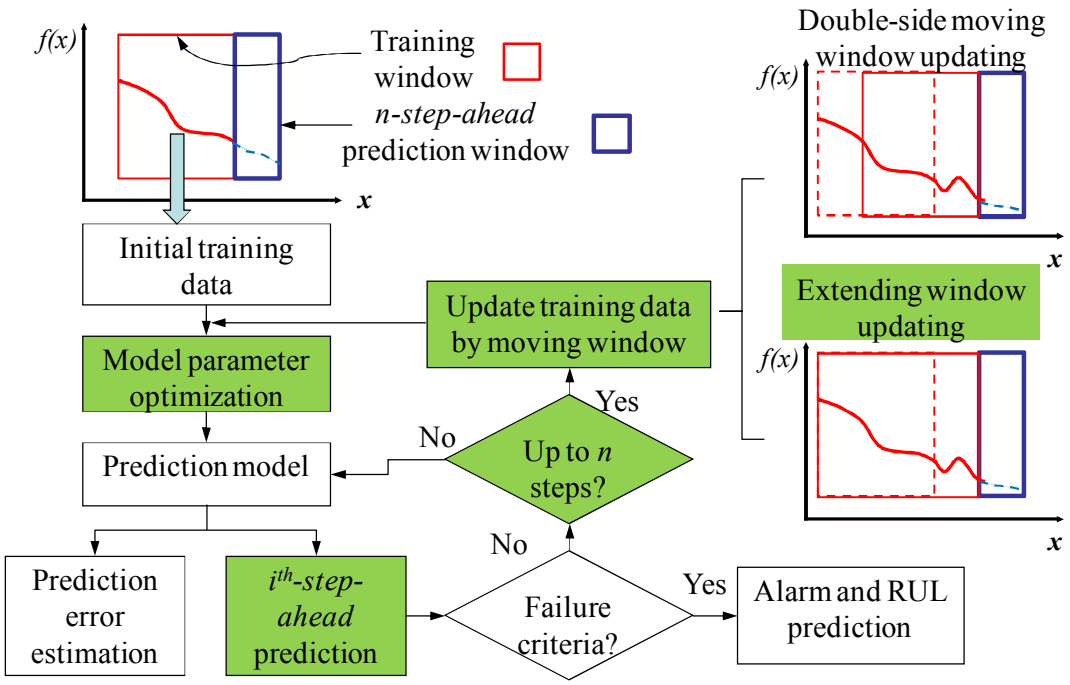

Figure 43: Moving window training updating based prediction method

Two MW methods were developed in this thesis to update the training data. The first one is called double-side MW updating, shown as the upper right in Figure 43. In this method, actual observations in the n-steps-ahead prediction window are added into the training data, but at the same time, the same amount of the oldest training data is discarded. It looks like a fixed size of training window slide n-steps ahead. The second method, shown in the middle right of the Figure 43, called extending window updating, does not discard the oldest training data, but keep all the data when the actual observations in the n-steps-ahead window are added in. The selection of the MW updating methods depends of the features of the data itself, if the features do not change so much, the double-side moving window method maybe enough. If more historic data are needed to present the features, the extending

window method is suitable. After the training data is updated, the next n-steps-ahead prediction will be conducted.

The most valuable information that n-steps-ahead prediction can provide is whether the product will fail in the *n* steps (such as, times or cycles) in the future. Most of researchers in prognostics try to calculate when the product will fail. But sometimes, it is more valuable to tell the heath information (health or failure) of a product in the near future. Then operators can have enough time but not too early to conduct maintenance or replacement. Besides this, n-steps-ahead may be more accurate than long-term prediction because of the accumulation of uncertainty of predictions. Furthermore, n-steps-ahead predictions can be conducted for individual products. It predicts the behavior in *n* steps in advance based on the historical information of the individual product itself.

This MW-DMPO n-steps-ahead prediction method can be implemented by using different data trending and regression models, such as autoregressive integrated moving average (ARIMA), neural networks (NN), and support vector regression (SVR). As a case study, the MW-DMPO n-steps-ahead prediction method was applied on support vector regression (SVR) to predict the failure of PPTC resettable fuses in this chapter. This chapter also developed a cross validation method to select proper SVR model parameters, selections of some of which have not been considered in literature. The entire method was called moving window cross validation SVR (MW-CVSVR).

6. 2 Development of MW-CVSVR

Many models have been used for time series forecasting in recent years, including ARIMA model [54][55] and neural network [56][57]. Selection of different modeling depends on the features of the data. For example, if the data is linear, ARIMA model is suitable, but if the data contains nonlinear components, neural network model has been thought as a universal approximator with an arbitrary accuracy [58][60].

The data shown in Figure 12 and Figure 13 presented nonlinear features and ARIMA model may be not a good choice. As a novel neural network technique, support vector regression (SVR), developed by Vapnik [58], has some advantages compared with traditional neural network modeling. SVR can achieve an optimum network structure by balancing between the empirical error and the confidence interval. This balance eventually leads to better generalization performance than other neural-network models. Additionally, the SVR training process is equivalent to solving linearly constrained quadratic programming problems, and the SVR embedded solution meaning is unique, optimal and unlikely to generate local minima[58][60].

However, using SVR for remaining useful life prediction of a product has been very limited in literature. Most of applications of SVR were focused on the forecasting of the time series data in financial area, such as stock price. Although Chen *et al.* [60], Tian *et al.* [71], Hong *et al.* [72], and Yang *et al.* [73] used SVR for

the reliability estimation, SVR was used only to predict the next reliability value based on the reliability values in the history. The research on using SVR for a real-time tool for the remaining useful life prediction based on actual *in-situ* monitored data directly has been very limited.

In this chapter, a MW-CVSVR model was developed to capture the updating degradation features of the data and predict the future values. MW-CVSVR can solve the problems of traditional SVR on model parameter selection and training data updating.

6.2.1 SVR modeling for precursor parameters

The basic idea for SVR includes mapping the input data X into a high-dimensional feature space F by kernel functions, and then solve a linear regression problem in the feature space. This process is shown in Figure 44. The linear regression in the feature space is presented as equation (17):

$$f(x) = \omega\varphi(x) + b \tag{17}$$

Where, $\varphi(x)$ is the feature in the feature space of data x in the input space. ω and b are coefficients, which are solved from the training data. Assuming a training data set including n data points, in which x_i is the input vector and y_i is target:

Training = $\{(x_i , y_i), i = 1,2,..., n\}$

In ε-SVR (Vapnik [58]), the objective is to find a function *f (x)* to estimate the output of input *x*. The requirements for the function *f(x)* include two points: 1) for all the training data (x_i, y_i), the output estimation of input x_i, $f(x_i)$, can only have at most ε deviation from the actually obtained targets y_i; In other words, errors are not concerned as long as they are less than ε; 2) at the same time *f(x)* must be as flat as possible, which requires small ω. [108].

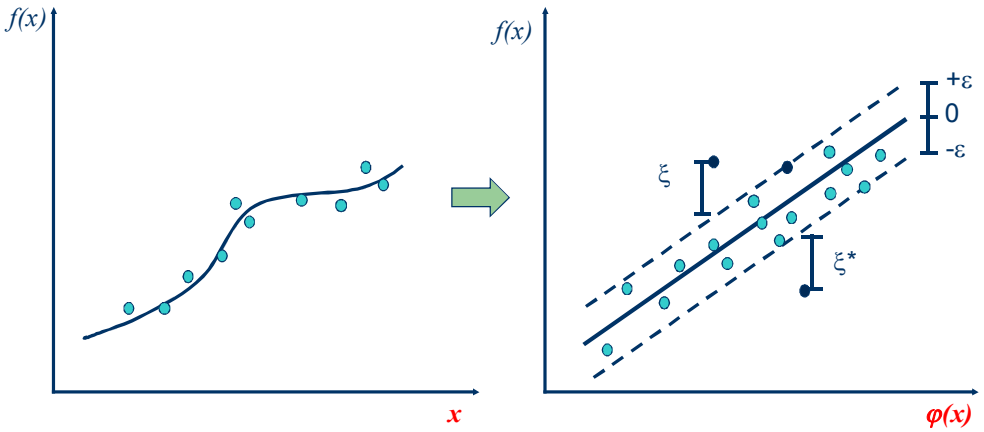

Figure 44: Non-linear SVR

A regularized risk function can be defined by balancing these two requirements as equation (18), in which the first item is used as a measure of the flatness, and second item is used to measure empirical risk. Equation (19) defines a ε-insensitive loss function. The loss is zero if the estimate is within the ε-tube, shown in Figure 44. *C* is called cost function, which specifies the trade-off between the empirical risk and the model flatness. Both *C* and ε are user-determined parameters.

$$R = \frac{1}{2}\|\omega\|^2 + C\frac{1}{n}\sum_{i=1}^{n} L_\varepsilon(f_i, y_i) \tag{18}$$

Where f_i is the estimated output of input x_i and y_i is the actual output of x_i.

$$L_\varepsilon(f,y)=\begin{cases}|f-y|-\varepsilon & |f\text{-}y|>\varepsilon \\ 0 & otherwise\end{cases} \tag{19}$$

The equation (19) has an assumption that function f actually exists and approximates all training data within ε-tube. However, sometimes, this may not be the case, or some small errors may be allowed. Slack variables, ξ_i and ξ_i^*, are introduced into to form a soft margin, shown in Figure 44. The slack variables assume non-zero values outside ε-tube. The SVR fits *f(x)* to the data to satisfy that 1) the training error is minimized by minimizing ξ_i and ξ_i^*, and 2) $(\omega \bullet \omega)/2$ is minimized to raise the flatness of *f(x)*. The entire task is to minimize the equation (20)

$$R=\frac{1}{2}\|\omega\|^2+C\sum_{i=1}^{n}(\xi+\xi^*) \tag{20}$$

Subject to:

$$\begin{aligned} &y_i-\omega\bullet\varphi(x_i)-b\le\varepsilon+\xi_i \quad i=1,2.\cdots,n \\ &\omega\bullet\varphi(x_i)+b-y_i\le\varepsilon+\xi_i^* \quad i=1,2.\cdots,n \\ &\xi_i^*,\xi_i\ge 0 \quad i=1,2.\cdots,n \end{aligned} \tag{21}$$

The minimization can be solved by introducing Lagrange multipliers and exploiting the optimality constraints [108].

$$\begin{aligned} L(\omega,\xi,\xi^*)=&\frac{1}{2}\|\omega\|^2+C\sum_{i=1}^{n}(\xi+\xi^*)-\sum_{i=1}^{n}\alpha^*{}_i(y_i+\varepsilon+\xi_i^*-\omega\bullet\varphi(x_i)-b) \\ &-\sum_{i=1}^{n}\alpha_i(\varepsilon+\xi_i+\omega\bullet\varphi(x_i)+b-y_i)-\sum_{i=1}^{n}(\beta_i\xi_i+\beta_i^*\xi_i^*). \end{aligned} \tag{22}$$

Finally, by applying Karush-Kuhn-Tucher (KKT) conditions for regression, the optimize formulation can be transformed into a Dual problem:

Maxing:

$$Q(\omega,\alpha_i,\alpha_i) = y_i\sum_{i=1}^{n}(\alpha_i^* - \alpha_i) - \varepsilon\sum_{i=1}^{n}(\alpha_i^* + \alpha_i) - \frac{1}{2}\sum_{i,j=1}^{n}(\alpha_i^* - \alpha_i)(\alpha_j^* - \alpha_j)K(x_i,x_j) \tag{23}$$

Subject to

$$\sum_{i=1}^{n}(\alpha_i^* - \alpha_i) = 0$$

$$0 \le \alpha_i^*, \alpha_i \le C \quad i = 1,2.\cdots, n \tag{24}$$

Where, α_i and α_i^* are Lagrange multipliers, and satisfy the equality, $\alpha_i \bullet \alpha_i^* = 0$. By solving the Lagrange multipliers α_i and α_i^*, the optimal weight vector of the regression is expressed as:

$$\omega = \sum_{i=1}^{nsv}(\alpha_i - \alpha_i^*)\varphi(x_i) \tag{25}$$

Then the regression is:

$$f(x,\alpha_i,\alpha_i^*) = \sum_{i=1}^{nsv}(\alpha_i - \alpha_i^*)K(x,x_i) + b \tag{26}$$

The *nsv* denotes the number of total support vectors. For ε-insensitive SVR, the vectors in the tube are not considered as support vectors. The training vectors, whose corresponding coefficients $(\alpha_i - \alpha_i^*)$ are non-zero values, have approximation error equal or larger than zero (on or outside the tube). Only these vectors are called support vectors. That means SVR do not need all training data as support vector, only a few vectors may generate a good regression.

$K(x_i,x_j)$ is the Kernel function, which is the inner product of two vectors x_i and x_j in the feature space, $\varphi(x_i)$ and $\varphi(x_j)$, meaning that $K(x_i,x_j)= \varphi(x_i) \bullet \varphi(x_j)$. The kernel function is intended to handle any dimension feature space without the need to calculate $\varphi(x)$ accurately. Any function can satisfy the Mercer's conditions then can perform the non-linear mapping. Common kernel functions used in SVR are listed in Table 18.

Table 18: Common Kernel functions

Kernel Function	Formula
Polynomial	$K(x,x_i) = (\langle x, x_i \rangle + b)^d$
Gaussian Radial Basis Function	$K(x,x_i) = \exp(\frac{-\|x-x_i\|^2}{2\sigma^2})$
Exponential Radial Basis Function	$K(x,x_i) = \exp(\frac{-\|x-x_i\|}{2\sigma^2})$
Multi-layer Perceptron	$K(x,x_i) = \tanh(\rho\langle x, x_i \rangle + \varsigma)$
Fourier Series	$K(x,x_i) = \frac{\sin(N+1/2)(x-x_i)}{\sin(0.5(x-x_i))}$
B Splines	$K(x,x_i) = B_{2N+1}\|x-x_i\|$ $with\ B_i = \bigotimes_{i=1}^{k} 1_{[-0.5,0.5]}$

Based on the understanding of the concepts of SVR, Figure 45 summarizes the procedures of SVR modeling [108]. In the training process, training data is used to obtain a model including the solutions of ω and b, support vectors, and all the corresponding mapped vectors in feature space. Support vectors are a subset of

training data. When a new vector is input to the model, it is mapped into the feature space by $\varphi(X)$, and then the dot product of $\varphi(X)$ with each existing mapped vectors in the feature space $\varphi(X_i)$ obtained from training data are calculated. These two processes are conducted by kernel function, $K(X,X_i)$, the output is the summation of the weighted dot products and the constant item b. The entire process is similar to regression in a neural network. The advantage over neural network is that SVR does not need all the training vectors but only a subset of it.

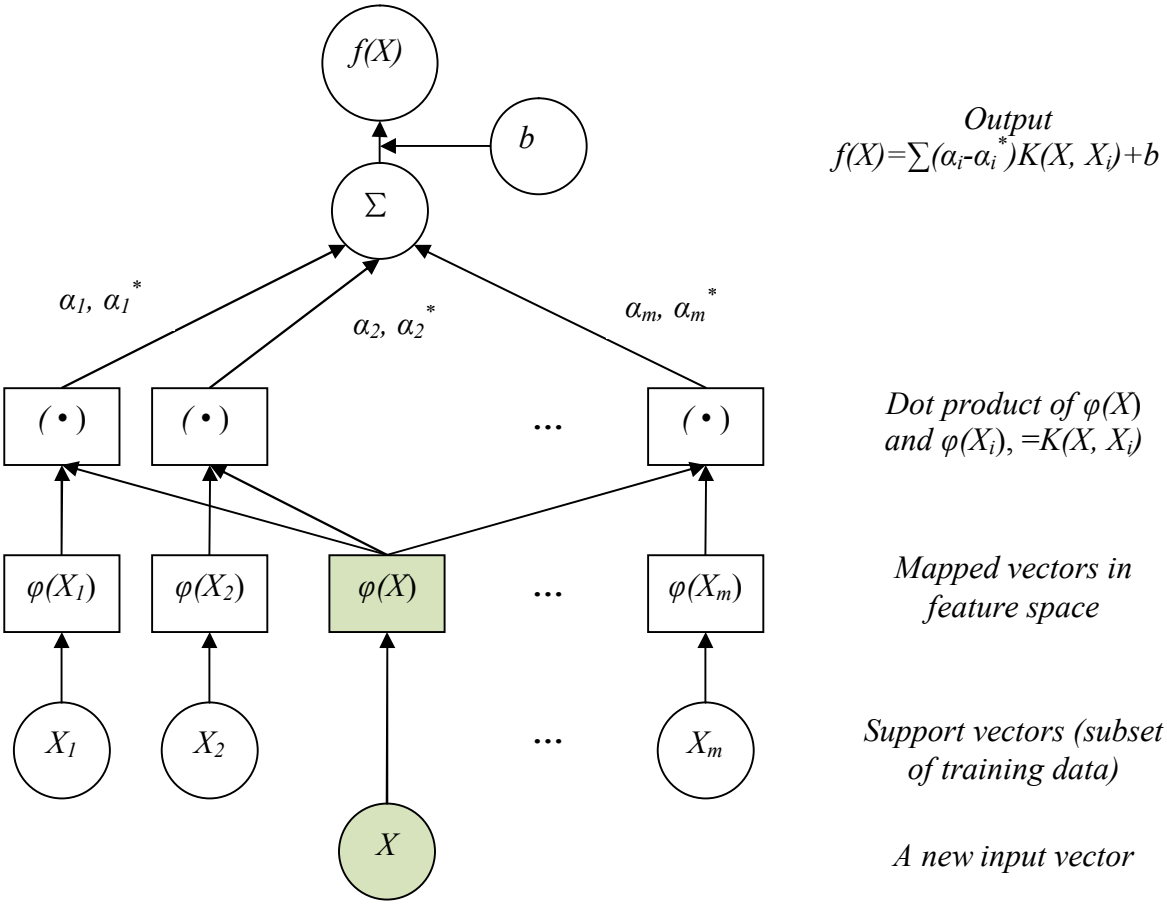

Figure 45: Schematic flowchart of SVR model

For the prediction model of univariate time series data, such as trip time or resistance after reset, the inputs data are past values, the lagged observations of the time series, while the outputs are the future values, shown in equation (27)

$$x_t = f(x_{t-1}, x_{t-2,\cdots,} x_{t-p}) \tag{27}$$

Table 19: Input and output pattern transformation for training data and process for n-steps-ahead prediction

	Index of Pattern (*i*)	Input Vector X_i	Output (Target or Prediction)
Training	*1*	$x_1, x_2, x_3, \ldots, x_p$	x_{p+1}
	2	$x_2, x_3, x_4, \ldots, x_{p+1}$	x_{p+2}
	3	$x_3, x_4, x_5, \ldots, x_{p+2}$	x_{p+3}
	⋮	⋮	⋮
	t-p	$x_{t-p}, x_{t-p+1}, x_{t-p+2}, \ldots, x_{t-1}$	x_t
n-steps - ahead prediction	*t+1*	$x_{t-p+1}, x_{t-p+2}, x_{t-p+3}, \ldots, x_t$	x'_{t+1}
	t+2	$x_{t-p+2}, x_{t-p+3}, x_{t-p+4}, \ldots, x'_{t+1}$	x'_{t+2}
	t+3	$x_{t-p+3}, x_{t-p+4}, \ldots, x'_{t+1}, x'_{t+2}$	x'_{t+3}
	⋮	⋮	⋮
	t+nstep	$x^{(')}_{t-+nstep-p}, \ldots, x'_{t+nstep-2}, x'_{t+nstep-1}$	$x'_{t+nstep}$

Where data vector *X:* $\{x_{t-1}, x_{t-2}, \ldots, x_{t-p}\}$ is the input data, which is p lagged values, while x_t is output or target. After training data is selected, it must be transformed into the certain $X \rightarrow Y$ pattern, in which X is the input vector and Y is the target, by a moving fixed-length window. The lag, which represents the number of

previous data or the length of the window, must be determined first. The transformation of the training data if the lag is p is shown in Table 19. Unfortunately, no systematic methods have been proposed to select the lag value.

6.2.2 Cross validation SVR (CVSVR)

In this thesis, Gaussian RBF is selected. It has only one variable to be determined, which can simplify the optimization of the model. In addition, SVR using RBF has excellent nonlinear regression ability. Four parameters, *C, ε, σ, and lag,* should be determined before the application of SVR model. Cross validation (CV) method has been used to select a proper *C, ε,* and *σ* for SVR. But the selection of lag value has not been considered in literature. In this thesis, all of four model parameters including the *lag* were selected by CV process.

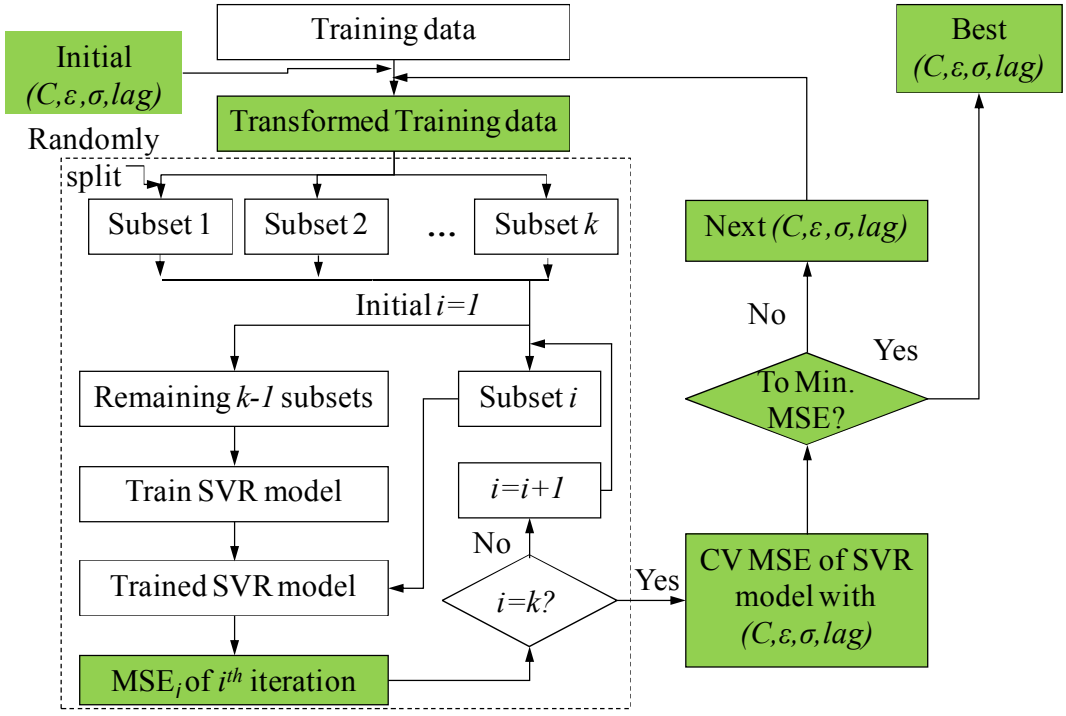

Figure 46: *k*-fold CV for SVR parameter optimization

Figure 46 shows the procedure using *k*-fold CV to select parameters for SVR. For each model set (*C, ε, σ, lag*), *k*-fold CV is used to calculate the prediction accuracy. When the accuracy reaches the criteria, the SVR model with that parameter set is used to predict the output of new input data. Before the *k*-fold CV process, the training data should be transformed (shown in Table 19) based on the value of *lag*. In *k*-fold CV, the transformed training data set is split into *k* equal or nearly equal sized subsets, then an iterated process is conducted to calculate the prediction accuracy. In each iteration, one subset is selected as validation data, and the other *k-1* subsets are used as training data to train the SVR model. The trained SVR model then is working on the validation data to predict the output for each input. The accuracy of prediction in the i^{th} iteration is calculated by mean squared error (MSE), shown in equation (28):

$$MSE_i = \frac{1}{nVal} \sum_{j=1}^{nVal} (y_j - f(x_j))^2 \tag{28}$$

Where *nVal* is the number of validation data.

After *k* iterations, the prediction accuracy of the SVR model with the parameter set (*C, ε, σ, lag*) can be calculated by equation (29):

$$MSE_{final} = \frac{1}{k} \sum_{i=1}^{k} MSE_i \tag{29}$$

When the MSE_{final} reaches the stop criteria, which can be defined as the minima of the MSE_{final}, the selection process is stopped and the SVR model with the corresponding parameter set is the final trained model, which is used for the prediction of a new test data. If the criteria are not reached, a new updated model

parameter set is input to the CVSVR to repeat the process. Table 20suggests the range of each parameter and how the CV updates the model set.

Table 20: Ranges of SVR model parameters

Parameter	Range	Start value	Interval
$Log_2(C)$	-10 ~10	-10	0.5
ε	0.01 ~ 0.2	0.01	0.01
$Log_2(\sigma)$	-10 ~10	-10	0.5
lag	5 ~15	5	1

6.2.3 MW-CVSVR

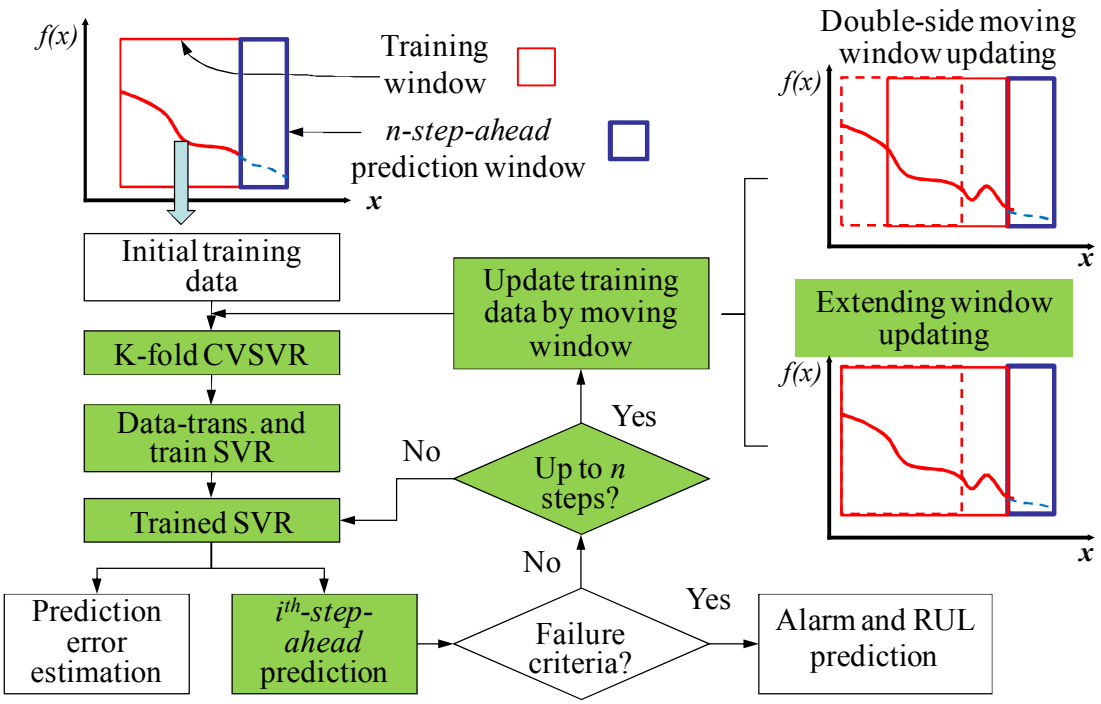

Figure 47: MW-CVSVR procedure

For failure prediction, training data for CVSVR modeling should contain the latest degradation features as much as possible. Using the developed MW training updating based prediction method in this thesis, a MW-CVSVR model was developed, shown in Figure 47.

Initial training data is transformed (shown in Table 19) and then used by *k*-fold CVSVR to select an optimal model parameter set for SVR. Then the training data is transformed again based on the optimal model parameters and used to train the SVR model, in which process the support vectors are identified and the coefficients and bias item are calculated. The n-steps-ahead predictions then can be calculated by this trained model. If any of the n-steps predictions reaches the threshold, alarm is triggered and a failure is predicted. If all the *n* predictions do not reach the failure threshold, a conclusion should be drawn to state that the fuse would not fail in the future *n* cycles. And then the training data for the prediction model should be updated by a MW method (double-side MW or extending window method) when the actual *n* observations are obtained. A new optimal model parameter set should be selected by cross validation process again. The model with the updated optimal model parameters should be trained by the updated training data to conduct the next n-steps-ahead predictions. This process is repeated until a failure is predicted. The prediction error is estimated by the residuals between the training data and its estimations. The actual application shows that the residuals are normally distributed. This MW-CVSPRT can always give the n-steps-ahead prediction to determine if failure will occur in near future, and the RUL prediction may be much closer to the actual failure.

6. 3 Prognostics of PPTC Resettable Fuses Using MW-CVSVR

The result of using MW-CVSVR on the failure prediction based on trip time data of PPTC fuses under -10°C condition is demonstrated in this section. Anomaly in terms of trip time under -10°C condition was detected at the 30th point (around

3000 cycles). So the prediction could be start at this point. The first 30 data points were used as the initial training data for MW-CVSVR. Gaussian radial basis function was chosen as the kernel function for MW-CVSVR and 3-fold cross validation was used to select the model parameters *(C, ε, σ, lag)*.

The accuracy of prediction is affected by the number of steps, *n,* and the MW methods (DMW and EW). The number of steps, *n,* also determines the number of predicted data in the future and the number of data used to update the training data (or steps in the window moving). The selection of *n* should be considered with a balance between the prediction error and the prediction distance. Figure 48 shows MSEs of predictions with different prediction steps, from 1 to 10, and different MW methods (DMW and EW) for trip time under -10°C conditions. Figure 49 shows the MSEs of predictions with different prediction steps and MW methods for minimum resistance after reset under -10°C conditions. Based on these two figures, 5-steps-ahead prediction is recommended as it balances accuracy and prediction distance.

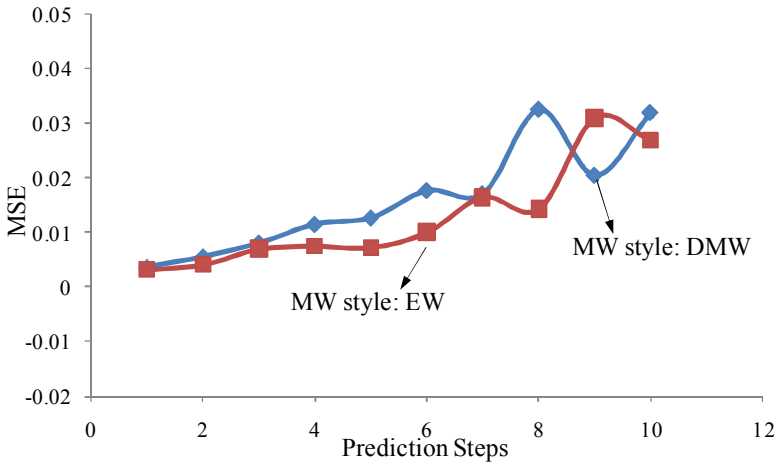

Figure 48: MSEs vs. number of prediction steps (trip time, -10°C).

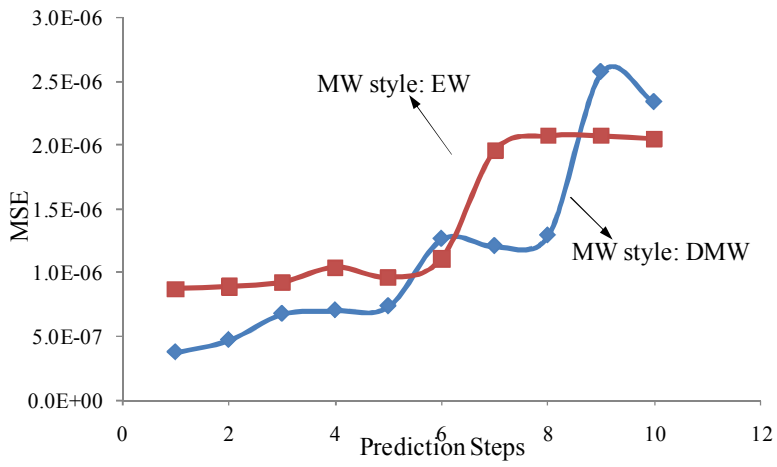

Figure 49: MSEs vs. number of prediction steps (min. resistance after reset, -10°C).

For comparison of accuracy for all conditions, 5-step-ahead prediction and 10-step-ahead prediction were conducted by MW-CVSVR. Both double-side MW updating and extending window updating methods were applied on this data. Figure 50 to Figure 53 are examples of 5-step-ahead prediction using double-side MW updating and extending window updating methods at different moments, in which the Figure 50 and Figure 51 are the predictions at the start moment, and Figure 52 and Figure 53 show the predictions when failure occurred based on the failure criteria. The predicted failures were exact the same with the actual failure, but the failures were predicted in 3 points (300 cycles) in advance.

The accuracy of prediction was evaluated by comparing the prediction results of all the n-steps-predictions at different moments with the original data, shown in Figure 54, Figure 55, Figure 56, and Figure 57. The figures indicate that the MW-CVSVR can catch the trends of the original data and the n-steps-ahead predictions

were close to the original data. Different training data updating methods and different prediction steps have different prediction accuracy. By comparing the MSE of different prediction methods, 5-step-ahead prediction with 5-step extending window training data updating had the best performance for the trip time data under -10°C condition.

Table 21 summarizes the prediction results for the trip time and resistance after reset under all conditions. The figures of the applications using MW-CVSVR model on trip time and resistance after reset under all the conditions are shown in Appendix C. The failure criteria for trip time for each environmental condition are defined as the 25% increase or decrease of the mean of the trip time used as training data for anomaly detection, shown in Table 17. The failure criteria for minimum resistance after reset (MinR) is defined as the 25% increase of the mean of the MinR values used as the training data for anomaly detection, shown in Table 17. The prediction results show that n-steps-ahead predictions by MW-CVSVR can capture the trends of the data and the predicted failures were very close to the actual failure. The alarmed cycles that were the number of cycles when the prediction was conducted were not later than the actual failures. It means that the n-steps-ahead prediction using MW-CVSVR can predict the actual failure in advance but not too early. It is also shown that 5-step-ahead prediction was better than 10-step-ahead prediction based on the MSE values.

Table 22 shows the comparison of 5-step-ahead prediction using MW-CVSVR and MW-SVR, in which the model parameters are not optimized for each updating of

training data. The MSEs of MW-CVSVR are smaller than those of MW-SVR. The alarmed cycles by MW-CVSVR are earlier than the actual failures while MW-SVR failed to predict some of the conditions. The comparisons indicate that the MW-CVSVR have much better performance than MW-SVR because of the contribution from dynamic model parameter optimization for each training data updating.

6. 4 Summary

Moving window based dynamic model parameter optimization (MW-DMPO) n-steps-ahead prediction method was developed in this chapter. This method keeps updating the training data by a moving window to contain the latest data so that the latest degradation information can be captured by the model. This method also optimizes the model parameters for the data trending models for each updating of the training data to ensure its high performance. As a case study of the developed MW-DMPO method, a moving window based cross validation support vector regression (MW-CVSVR) was developed for the prediction of PPTC resettable fuses. The cross validation technique solved the model parameter selection for SVR including the lag value. The application of MW-CVSVR on the PPTC resettable fuse shows that the developed method worked well on the prediction. The MW-DMPO method can be extended to apply on any data trending and regression methods, such as ARIMA and Neural networks.

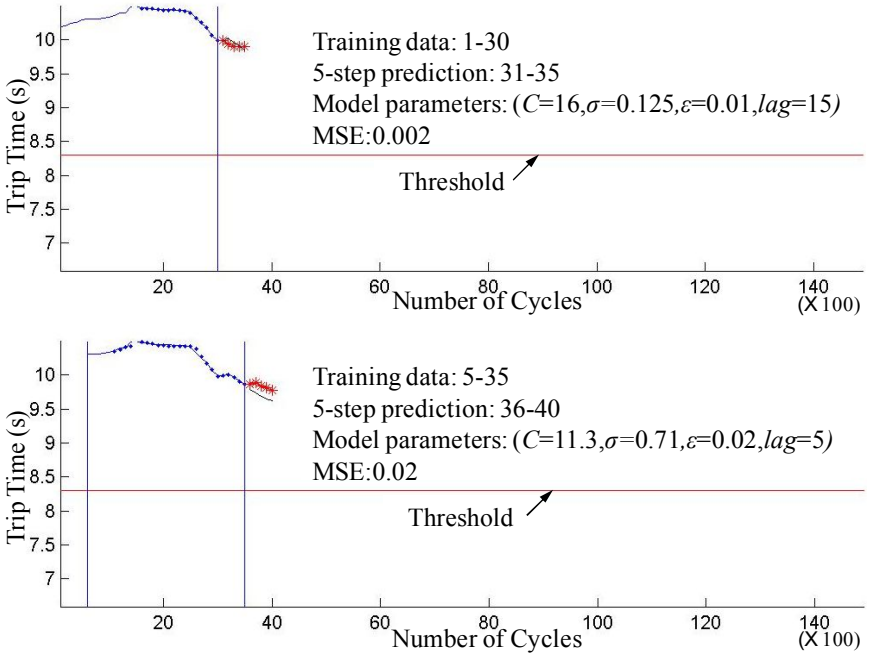

Figure 50: Example of double-side MW 5-step-ahead prediction (1-30→5-35, -10°C)

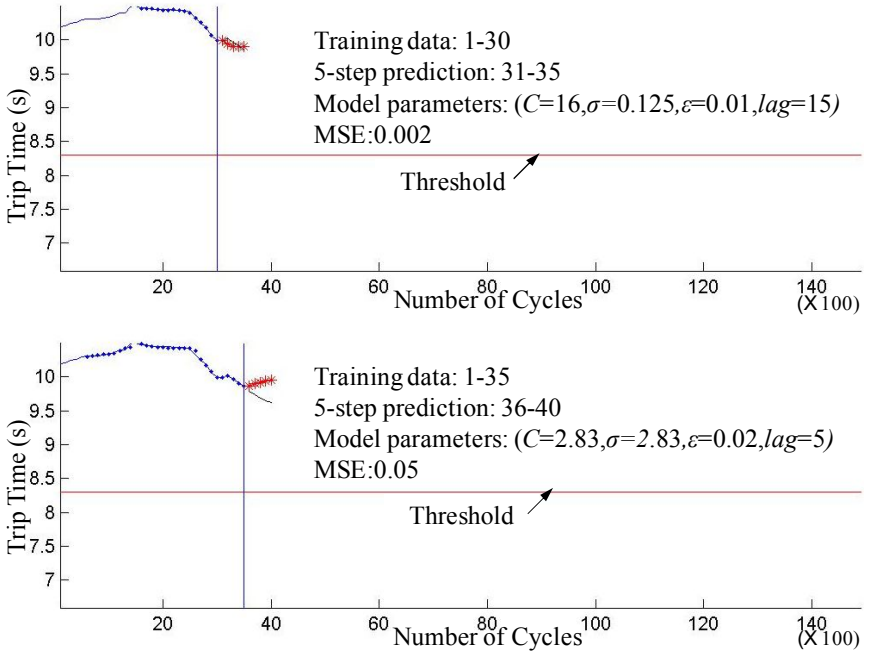

Figure 51: Example of extending window 5-step-ahead prediction (1-30→1-35, -10°C)

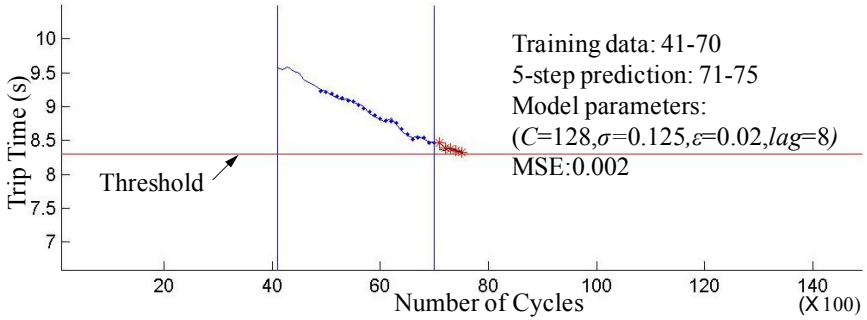

Figure 52: Example of double-side MW 5-step-ahead prediction (41-70→46-75, -10°C)

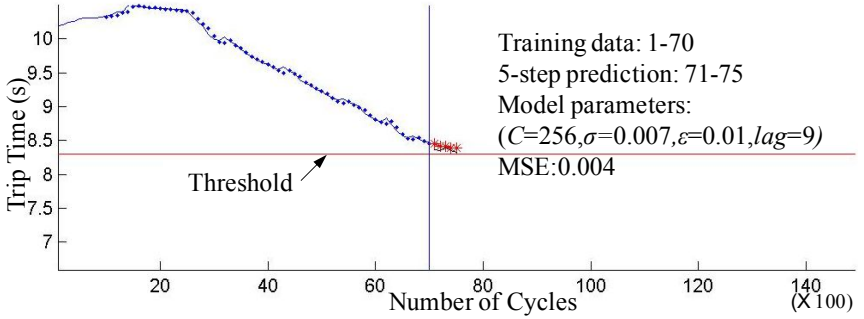

Figure 53: Example of extending window 5-step-ahead prediction (1-70→1-75, -10°C)

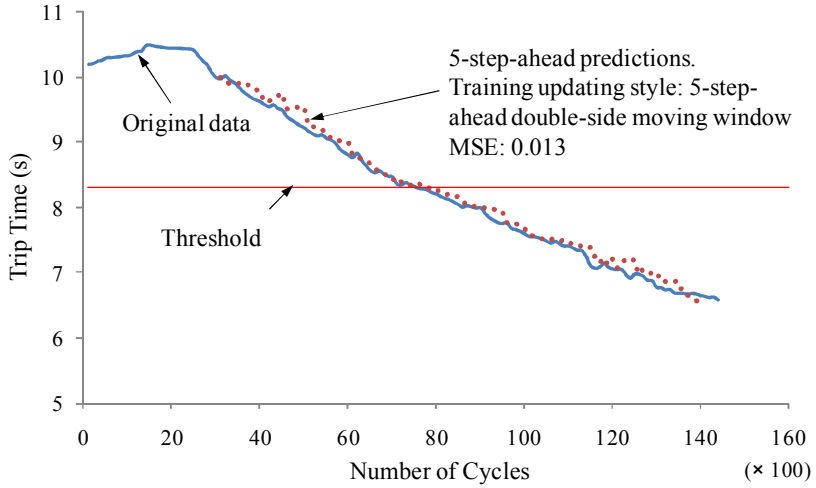

Figure 54: All 5-step-ahead predictions (-10°C,trip time, double-side MW)

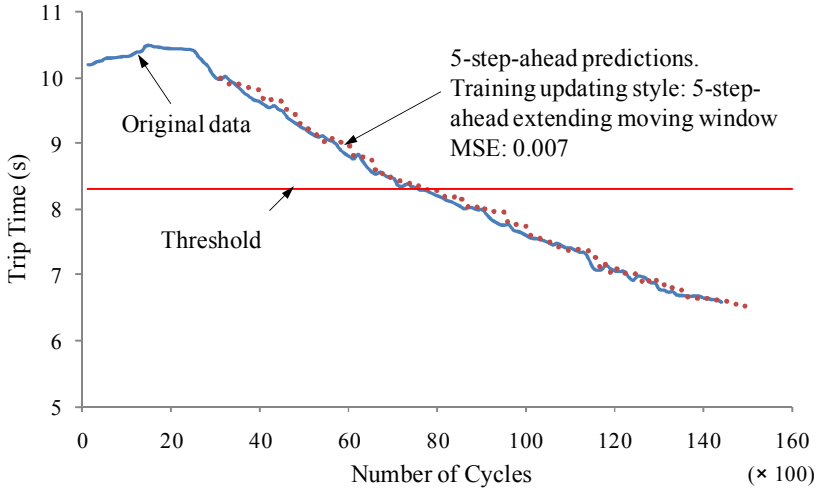

Figure 55: All 5-step-ahead predictions (-10°C, trip time, extending window)

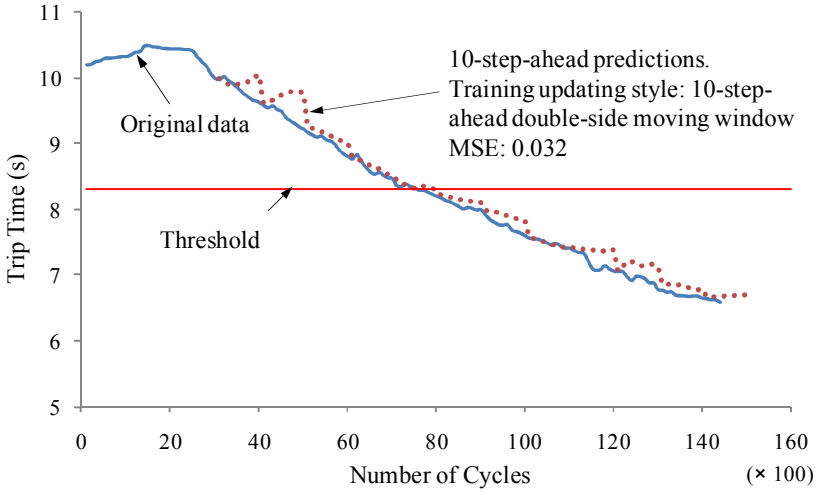

Figure 56: All 10-step-ahead predictions (-10°C,trip time, double-side MW)

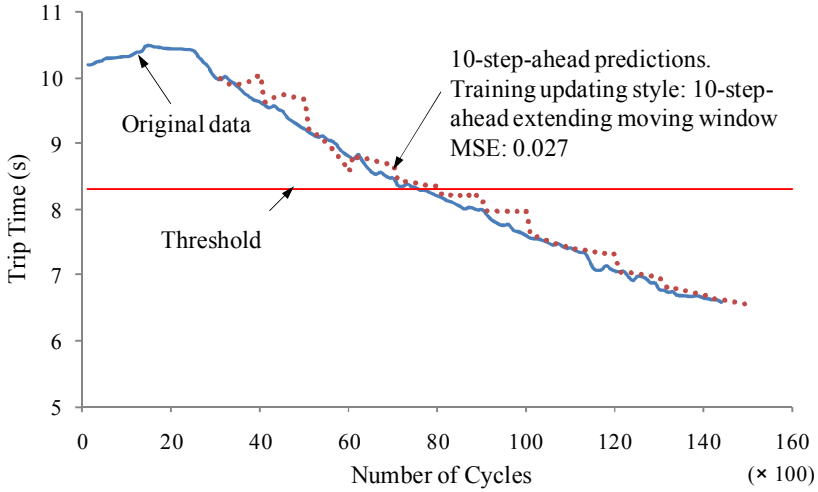

Figure 57: All 10-step-ahead predictions (-10°C,trip time, extending window)

Table 21: Summary of MW-CVSVR prediction results

Conditions	Parameters	Moving window style (double-side or extending)	Moving steps	Prediction steps	Alarmed cycle (The number of cycle when the prediction is conducted (×100)	Predicted failure cycle (×100)	Actual failure cycle (×100)	MSE
-10°C	TT	Double-side	5	5	75	78	79	0.013
		Extending	5	5	75	77		0.007
		Double-side	10	10	70	80		0.032
		Extending	10	10	80	81		0.027
	MinR	Double-side	5	5	100	105	108	1.3E-06
		Extending	5	5	95	98		9.58E-07
		Double-side	10	10	105	107		2.34E-06
		Extending	10	10	95	98		2.05E-06
RT	TT	Double-side	5	5	120	121	121	0.02
		Extending	5	5	120	122		0.015
		Double-side	10	10	110	116		0.076
		Extending	10	10	120	121		0.076
	MinR	Double-side	5	5	115	117	122	1.96E-06
		Extending	5	5	115	119		1.86E-06
		Double-side	10	10	115	117		3.06E-06
		Extending	10	10	115	119		3.23E-06
60°C	TT	Double-side	5	5	No failure based on failure criteria			3.8E-04
		Extending	5	5				3.6E-04
		Double-side	10	10				5.1E-04
		Extending	10	10				6.6E-04
	MinR	Double-side	5	5	165	166	167	8.02E-07
		Extending	5	5	165	166		6.47E-07
		Double-side	10	10	165	166		1.61E-06
		Extending	10	10	165	166		1.47E-06

85°C	TT	Double-side	5	5	No failure based on failure criteria			4.8E-03
		Extending	5	5				1.1E-02
		Double-side	10	10				7.9E-03
		Extending	10	10				1.2E-02
	MinR	Double-side	5	5	120	125	126	4.06E-06
		Extending	5	5	125	126		5.59E-06
		Double-side	10	10	115	125		6.86E-06
		Extending	10	10	125	126		8.76E-06

Table 22: Comparison of 5-step-ahead predictions by MW-CVSVR and MW-SVR

		5-step-ahead prediction and 5-step-ahead moving	MSE		Alarmed cycle (×100)		Predicted failure cycle (×100)		Actual failure cycle (×100)
			MW-CVSVR	MW-SVR	MW-CVSVR	MW-SVR	MW-CVSVR	MW-SVR	
-10 °C	TT	DMW	0.013	0.02	75	75	78	80	79
		EW	0.007	0.01	75	75	77	78	
	MinR	DMW	1.3E-06	1.45E-06	100	115	105	116	108
		EW	9.58E-07	2.4E-06	95	120	98	121	
RT	TT	DMW	0.02	0.03	120	125	121	126	121
		EW	0.015	0.04	120	125	122	126	
	MinR	DMW	1.96E-06	2.0E-06	115	125	117	127	122
		EW	1.86E-06	7.33E-06	115	150	119	152	
60 °C	TT	DMW	3.8E-04	4.6E-04	No failure based on failure criteria				
		EW	3.6E-04	8.5E-04					
	MinR	DMW	8.02E-07	9.0E-07	165	165	166	170	167
		EW	6.47E-07	8.12E-07	165	170	166	171	
85 °C	TT	DMW	4.8E-03	5.0E-03	No failure based on failure criteria				
		EW	1.1E-02	1.15E-02					
	MinR	DMW	4.06E-06	5.39E-06	120	125	125	126	126
		EW	5.59E-06	7.49E-06	125	130	126	132	

Chapter 7: Contributions and Future work

Contributions of this thesis include the following:

1) Determined the failure precursor parameters for PPTC resettable fuses, shown in chapter 3. Potential precursor parameters were determined by failure modes, mechanisms, and effects analysis (FMMEA), and then a series of experiments were conducted to verify these parameters. Trip time, resistance after reset, and surface temperature have been determined as precursor parameters for observed failures, including the cracks at the coating and solders, gaps between different parts of the fuse, and the performance shifting of the fuses, such as tripping faster and faster and the resistance becoming higher and higher. These precursor parameters should be monitored when testing or in the actual application. Other parameters, including the maximum resistance during trip endurance and the resistance in aging test did not exhibit obvious changes (<5% of the initial values) under all test conditions. They are not considered as failure precursors.

2) Determined the causes of the observed failures for PPTC resettable fuses considering the interconnections of different parts in the fuse, shown in chapter 4. A series of failure analyses, including the heating process analyses by infrared camera, the interconnection analyses by cross-section and ESEM, the analyses of microstructures of carbon black(CB)/polyethylene (PE) composite, the thermal property analyses of CB/PE composite, and the CTE analyses of different parts of the component were conducted. The gaps between coating and the foil, caused by thermal fatigue and CTE-mismatches, are the main causes

for decreases in the trip time. Aside from the gaps, the increases in the crystallinity of CB/PE composite are the main causes for the increases in the trip time. The agglomeration of the CB particles is one of the main causes for the increase in the resistance after reset. With the increases in the cycle numbers, the cracks at the solder and the gaps between foil and CB/PE composite will control the increases in the resistance and finally cause an open of current.

3) Developed an *in-situ* anomaly detection method using cross validation sequential probability ratio test (CVSPRT), shown in chapter 5. The cross validation was used to select optimal model parameters for SPRT to reduce the false alarm and missed alarm probabilities. The value of the approach is that CVSPRT can be extended to conduct *in-situ* anomaly detection for any conditions if the training data is available and the SPRT index can be calculated.

4) Developed a moving window (MW) based dynamic model parameter optimization (MW-DMPO) n-steps-ahead prediction method, shown in chapter 6. This method involves the latest monitored data by a moving window to update the training data for data trending and regression models to capture the latest degradation information, and for each updating of the training data, the model parameters are optimized by the dynamic model parameter optimization methods. Besides being used in the support vector regression (SVR) in this thesis, the developed MW-DMPO method can be extended as general training data updating methods for data trending and regression models, such as ARIMA and NN models, to enable more accurate failure prediction.

5) Developed a moving window cross validation SVR (MW-CVSVR) for n-steps-ahead prediction, shown in chapter 6. In MW-CVSVR n-steps-ahead prediction, the CV method is used to optimze model parameters for SVR including the lag value and then train the SVR model. The trained SVR model predicts *n* values of the monitored precursor parameter in the future. MW method is used to update the training data to ensure the SVR model capture the latest degradation features. MW-CVSVR was used on trip time and resistance after reset to predict the failures of PPTC resettable fuses in this thesis. The results of 5-step-ahead predictions and 10-step-ahead predictions using MW-CVSVR showed that the MW-CVSVR can capture the trends of the data and predict the failures accurately and not too early. MW-CVSVR can be used as a general method for nonlinear data regression.

Future work may include the following:

1) Determine the failure mechanisms of PPTC resettable fuses and develop PoF models to predict failures. The mechanisms of the polymer positive are complex and highly depend on the composition of the composite and the usage conditions. More experiments and analyses are required to reveal and model the formation of cracks and gaps, diffusion and aggregation of the CB fillers, and the changes in the properties of the polymer matrix.

2) Develop a methodology to dynamically choose the double-side moving window training or extending window training for prediction.

3) Develop a method to evaluate the uncertainty of the moving window based failure prediction methods. The impact factors may include the uncertainty from

the sensing, training, and modeling. For MW-CVSVR, the errors from the training data can indicate the prediction uncertainty in some degrees; however a better way is required to evaluate the prediction uncertainty.

Appendix A: Results of Failure Analyses

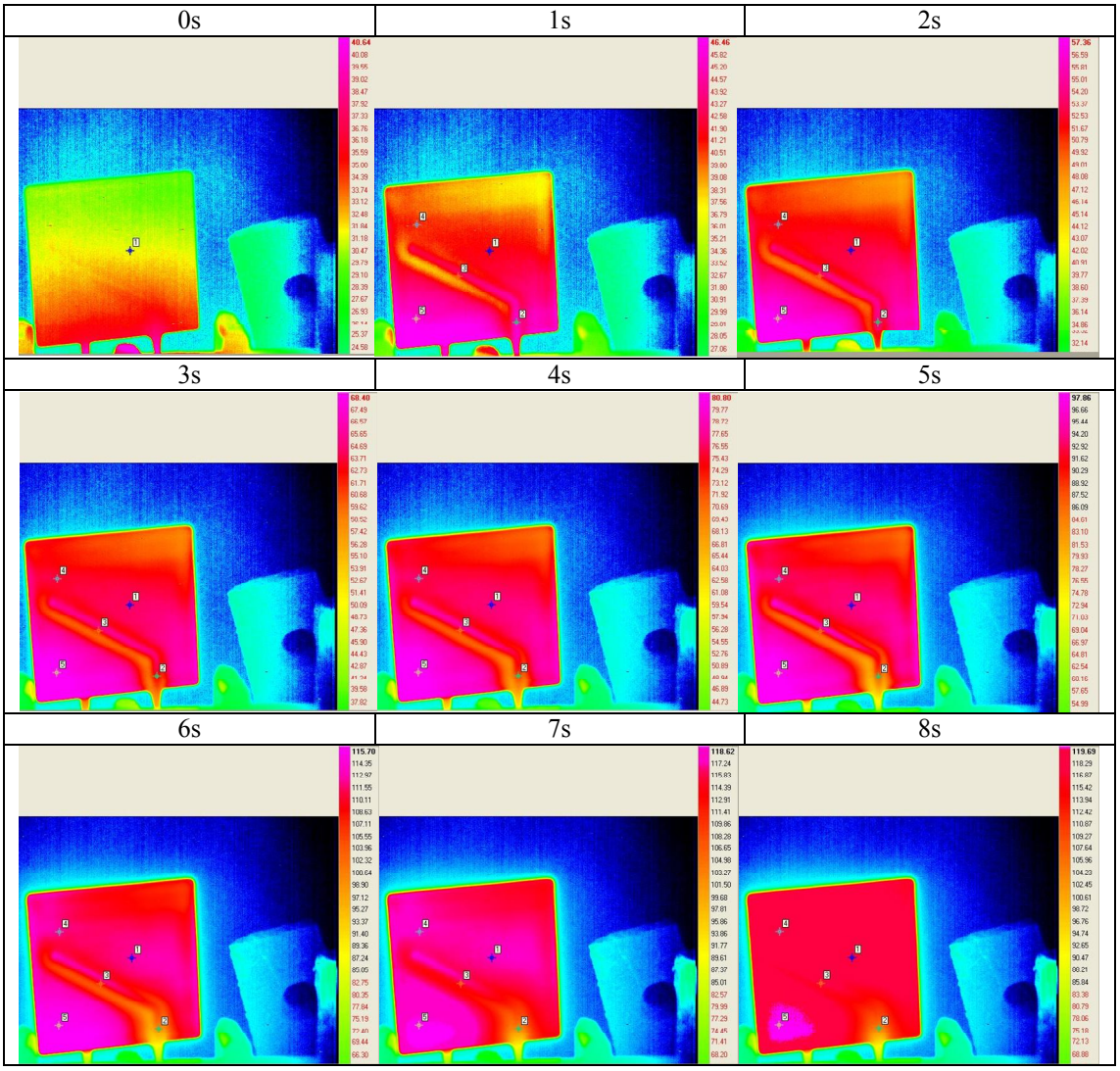

Figure 58: Typical IR pictures of a new sample

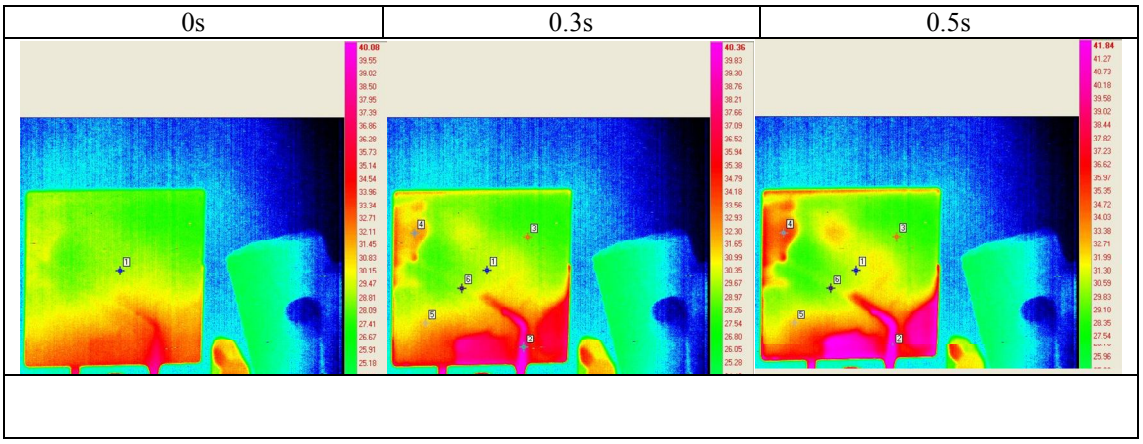

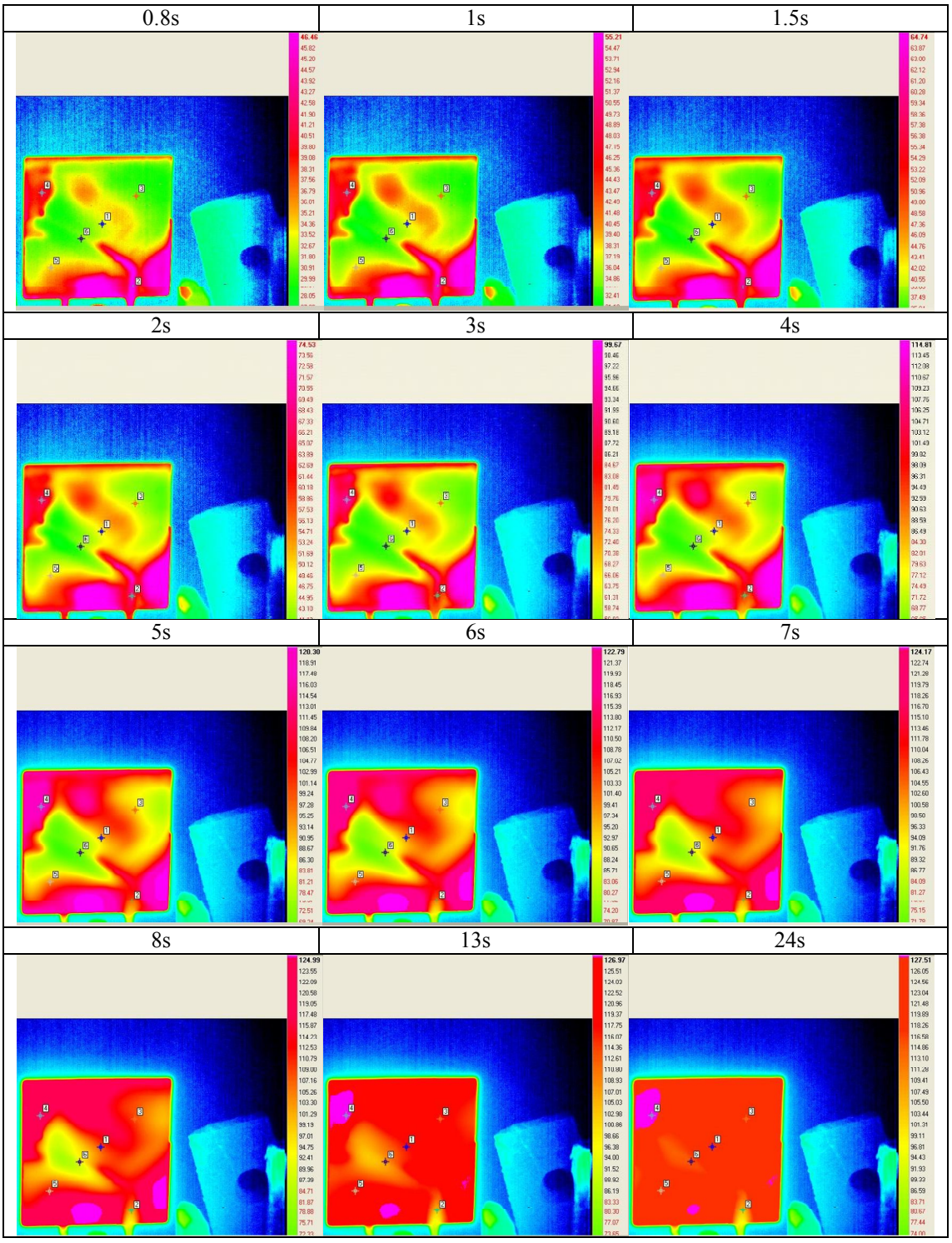

Figure 59: Typical IR pictures of tested sample (-10 °C, trip cycle)

0s	0.2s	0.4s
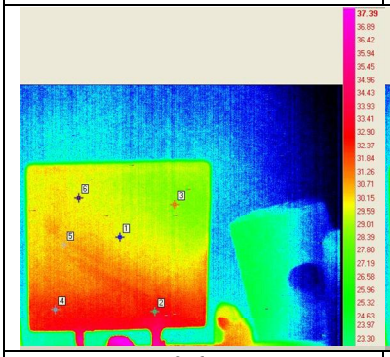	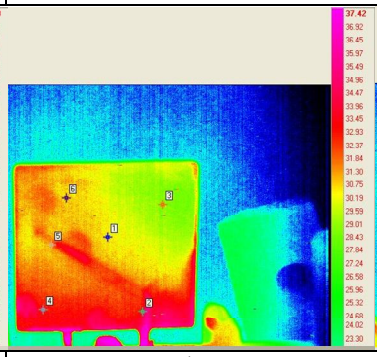	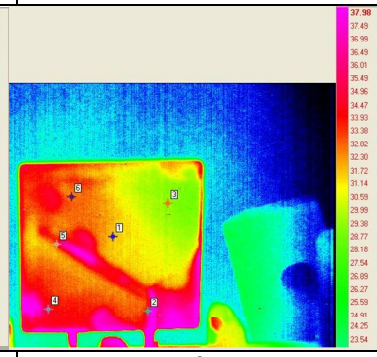
0.6s	1s	2s
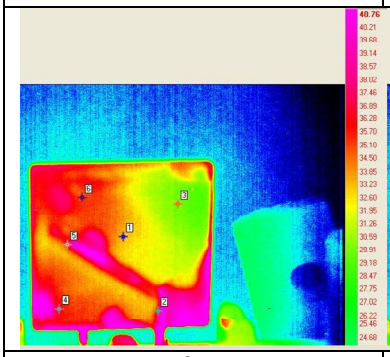	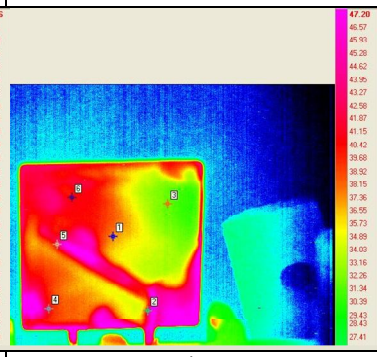	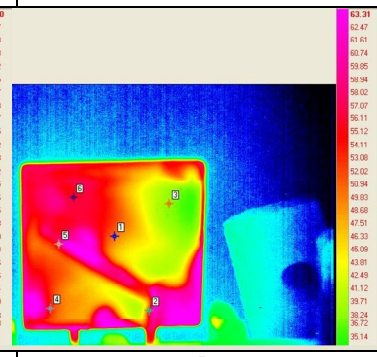
3s	4s	5s
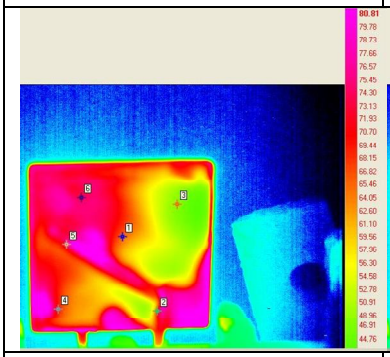	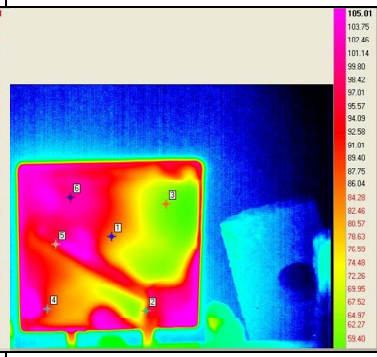	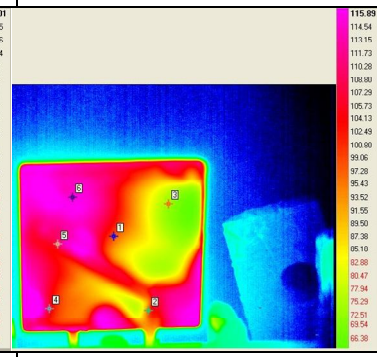
6s	7s	8s
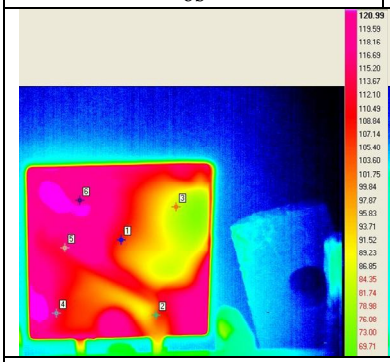	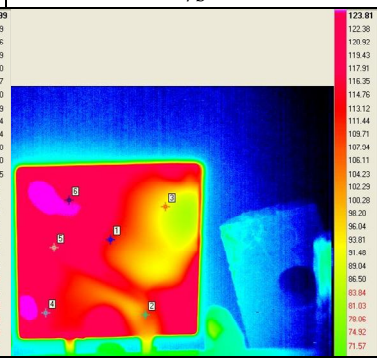	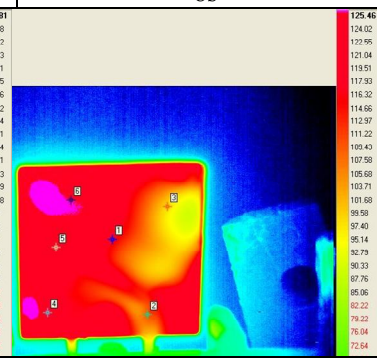

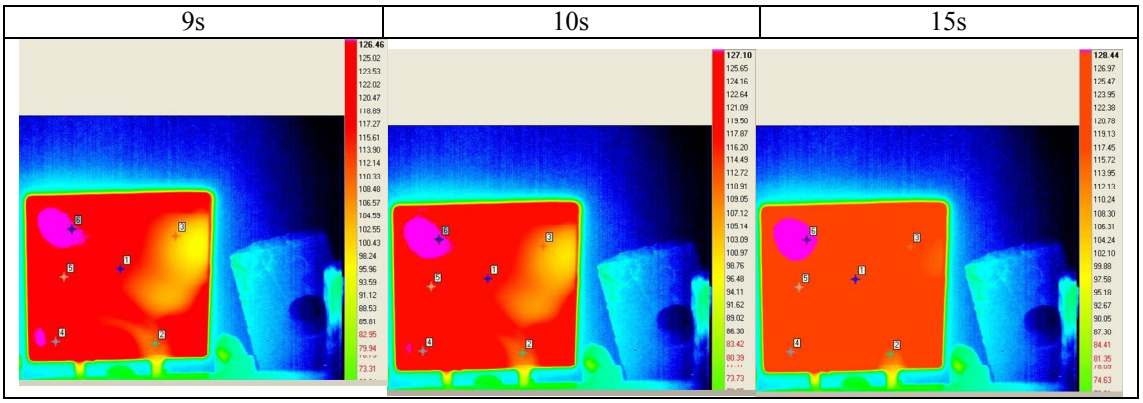

Figure 60: Typical IR pictures of tested sample (RT, trip cycle)

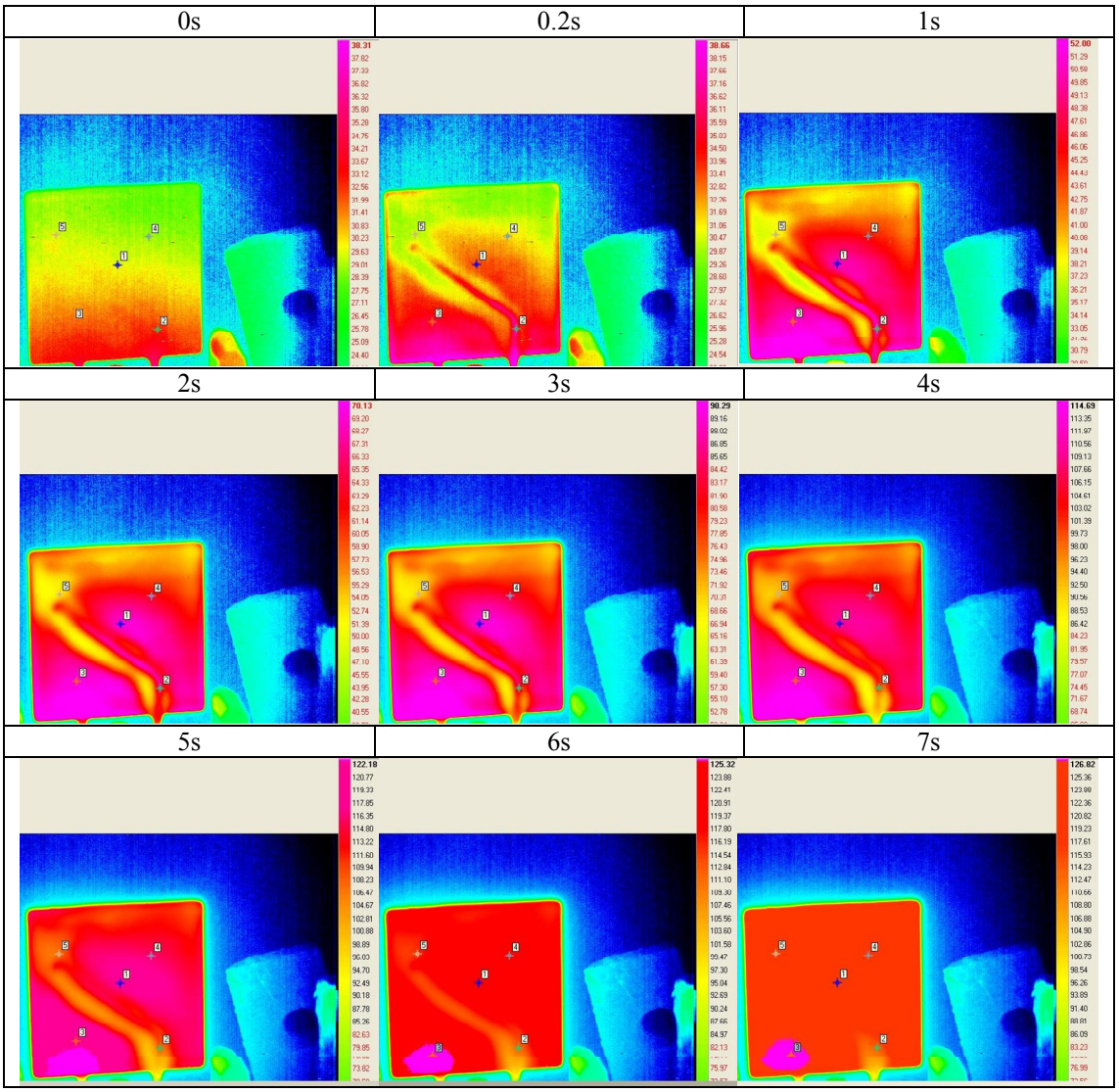

Figure 61: Typical IR pictures of tested sample (60 °C, trip cycle)

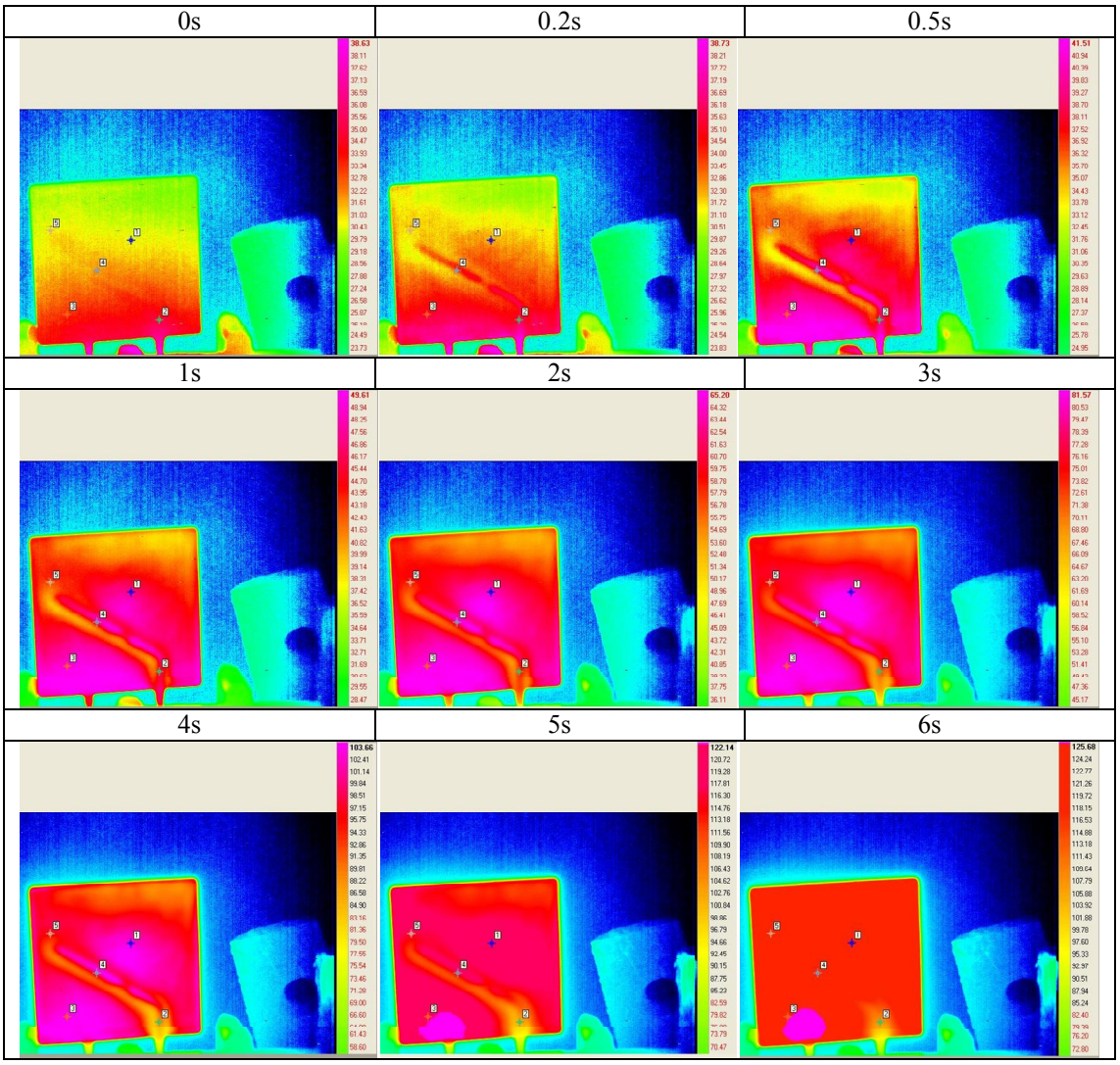

Figure 62: Typical IR pictures of tested sample (85°C, trip cycle)

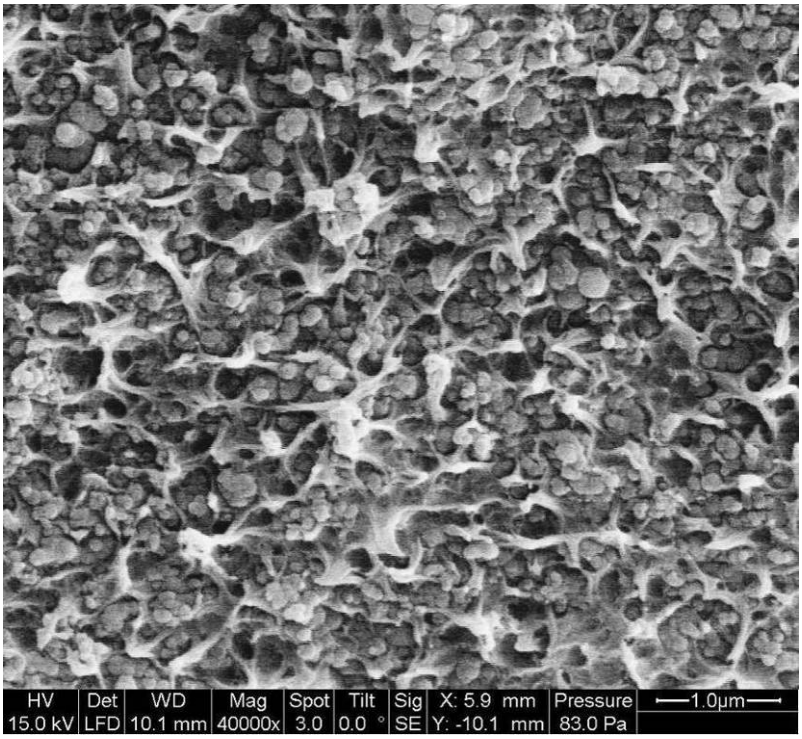

Figure 63: Typical microstructure of CB and PE of tested samples (-10°C, aging, freeze fractured)

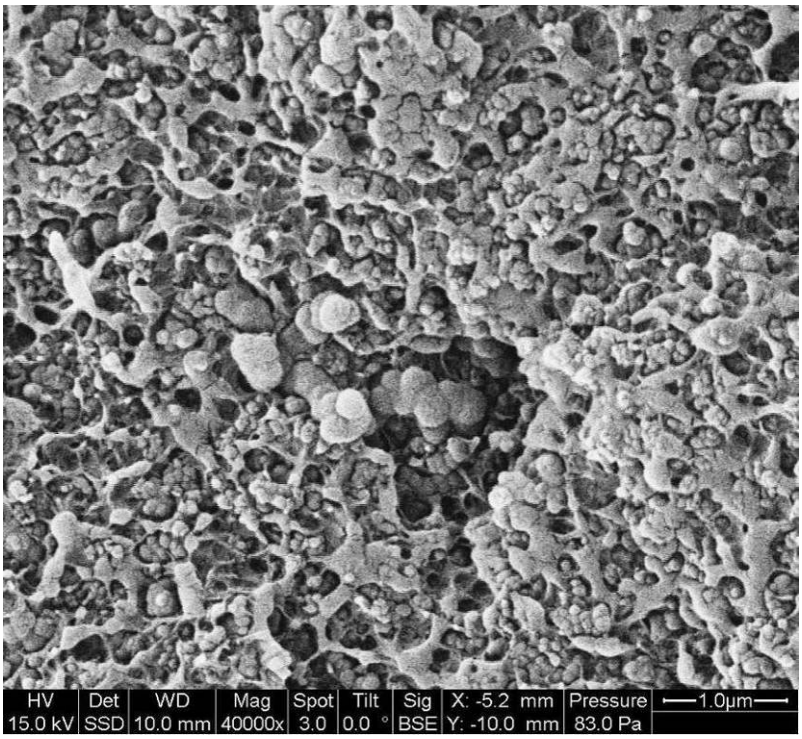

Figure 64: Typical microstructure of CB and PE of tested samples (-10 ° C, trip cycles, freeze fractured)

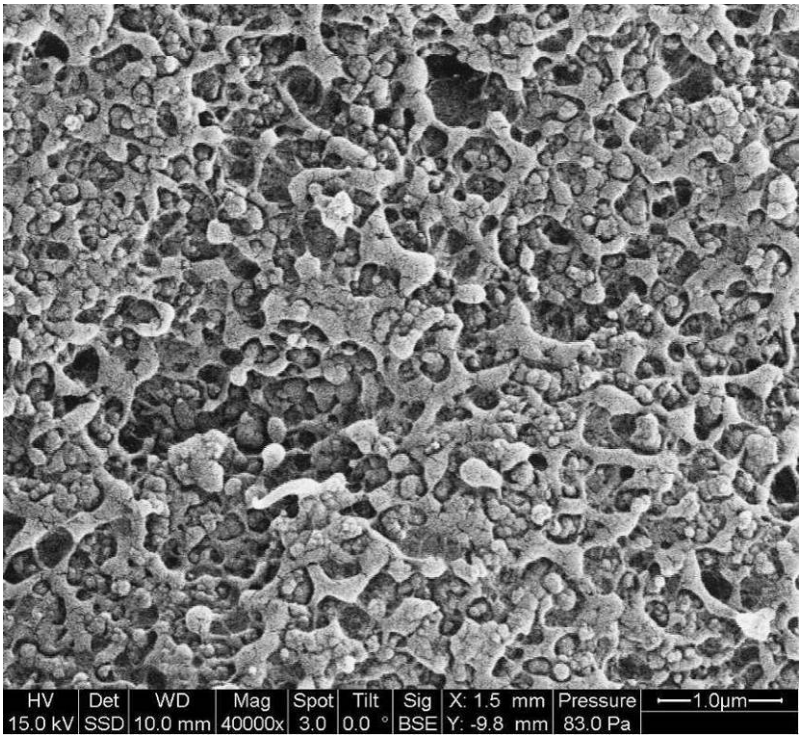

Figure 65: Typical microstructure of CB and PE of tested samples (RT, aging, freeze fractured)

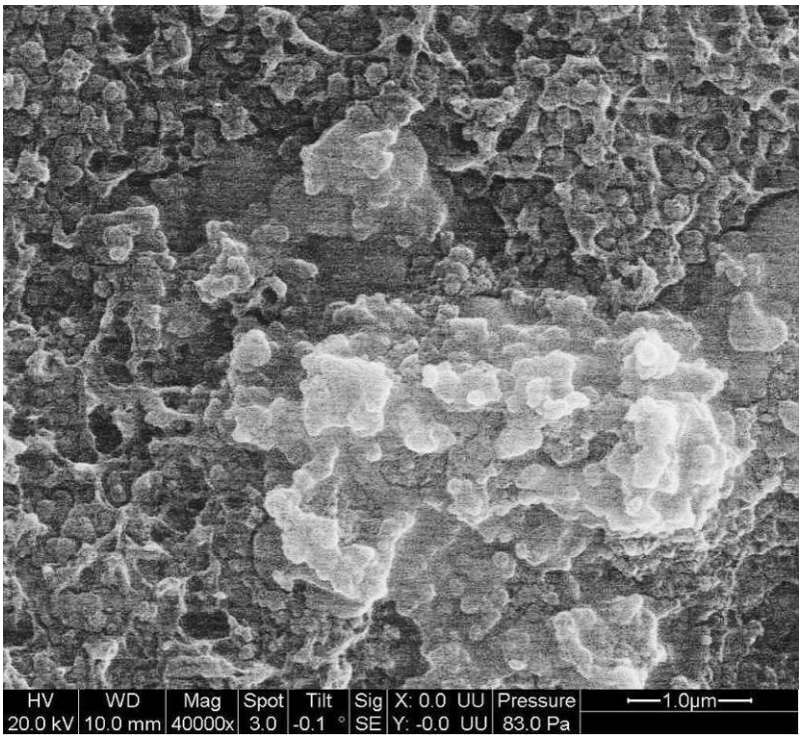

Figure 66: Typical microstructure of CB and PE of tested samples (RT, trip cycle, freeze fractured)

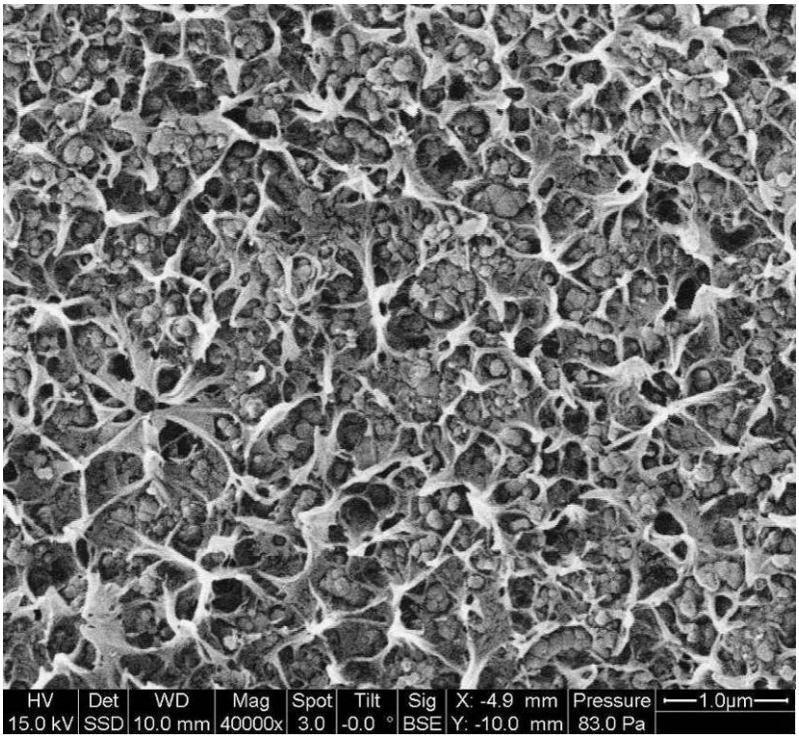

Figure 67: Typical microstructure of CB and PE of tested samples (60° C, aging, freeze fractured)

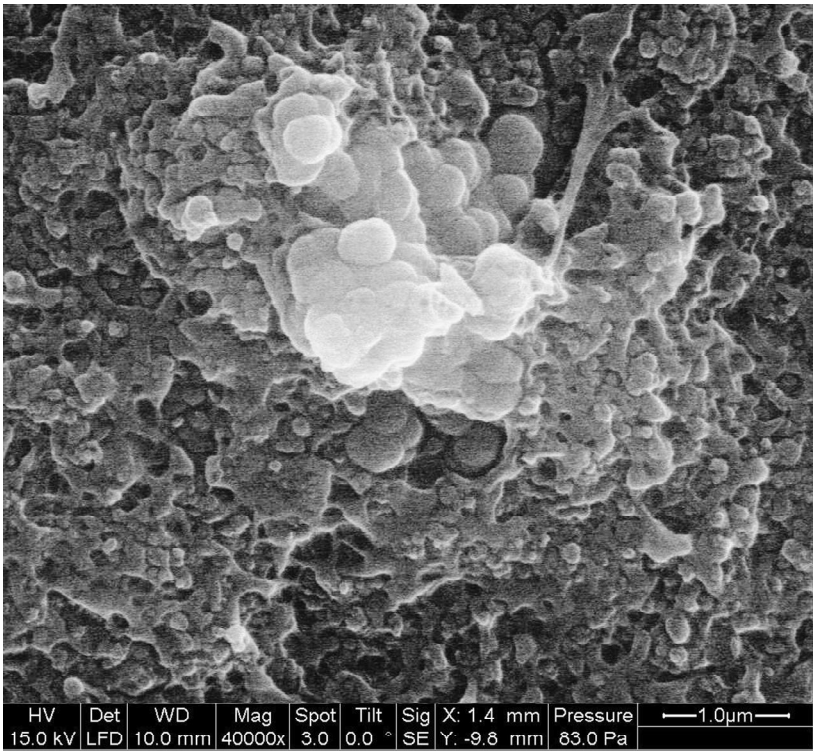

Figure 68: Typical microstructure of CB and PE of tested samples (60 ° C, trip cycles, freeze fractured)

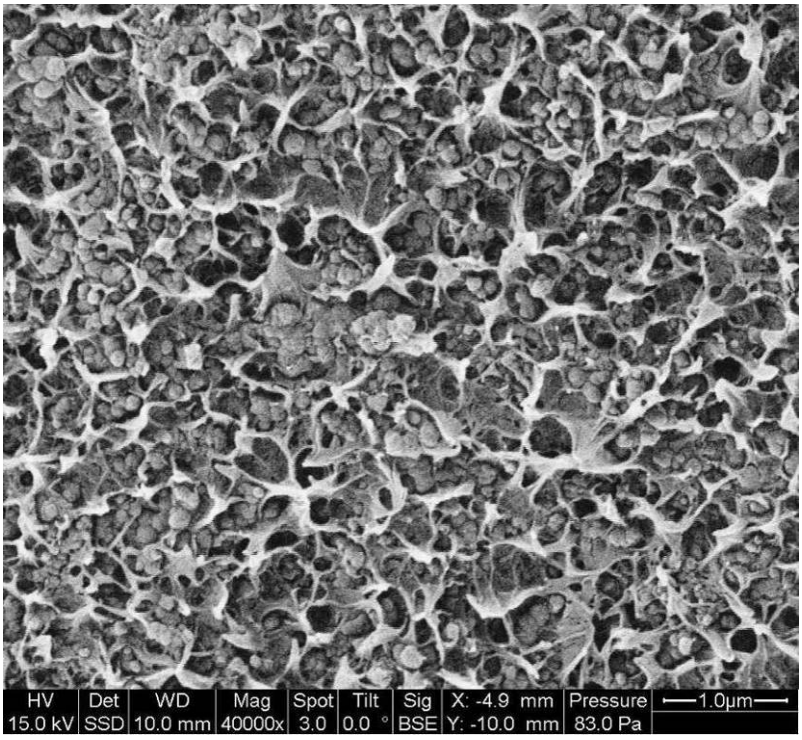

Figure 69: Typical microstructure of CB and PE of tested samples (85°C, aging, freeze fractured)

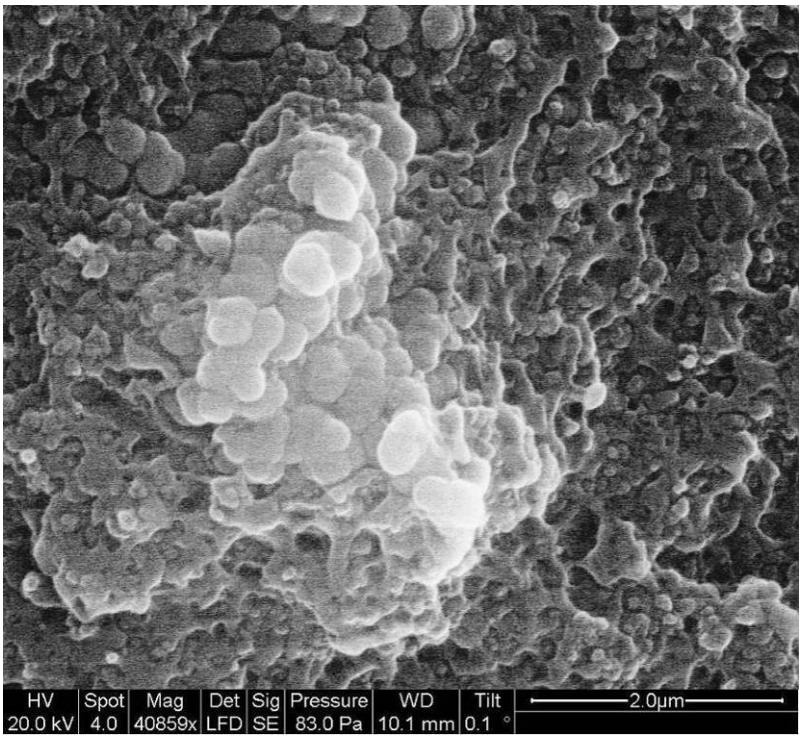

Figure 70: Typical microstructure of CB and PE of tested samples (85 ° C, trip cycles, freeze fractured)

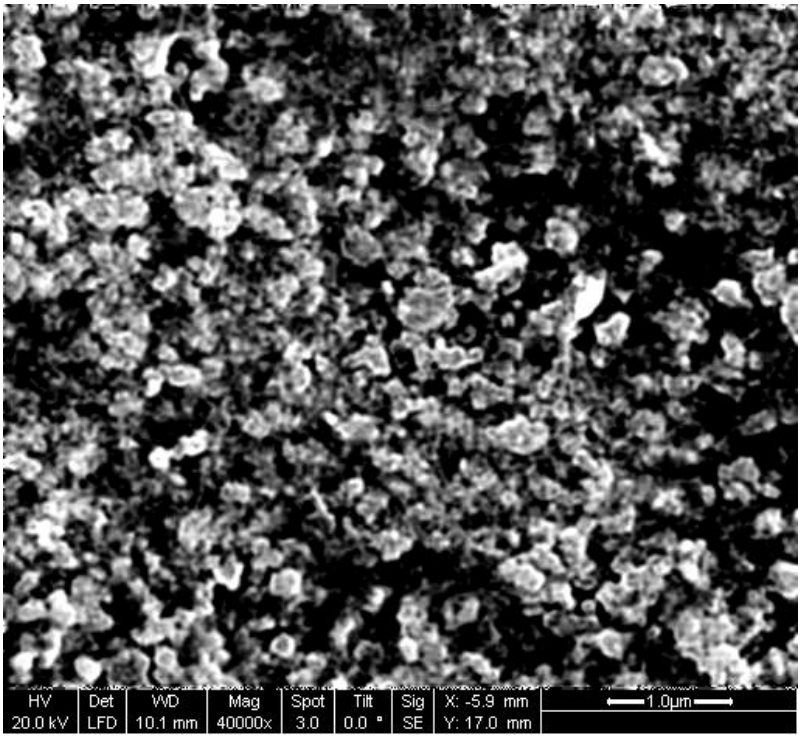

Figure 71: Typical microstructure of CB and PE of tested samples (-10°C, aging, etched by Argon ions)

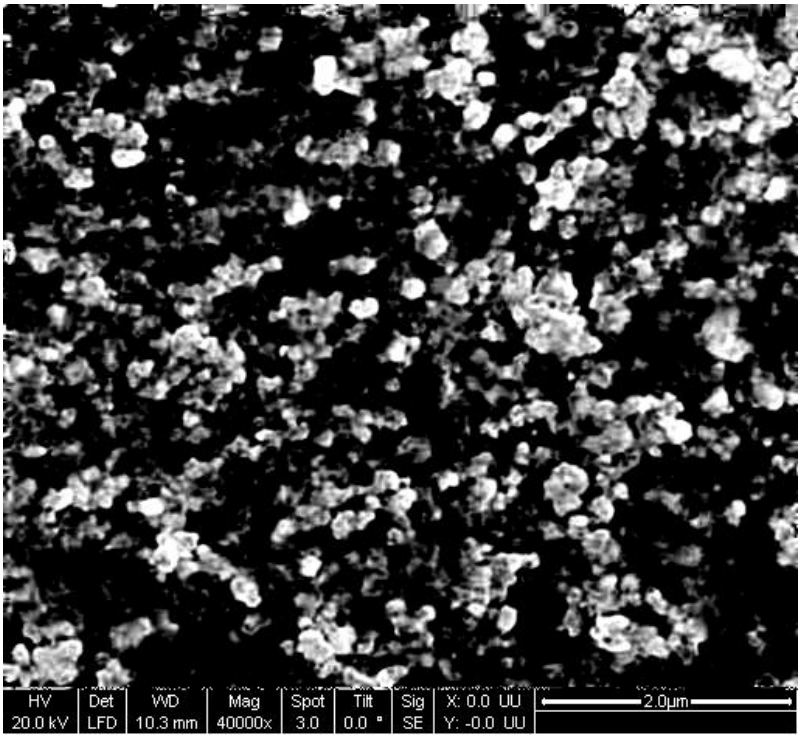

Figure 72: Typical microstructure of CB and PE of tested samples (-10°C, trip cycle, etched by Argon ions)

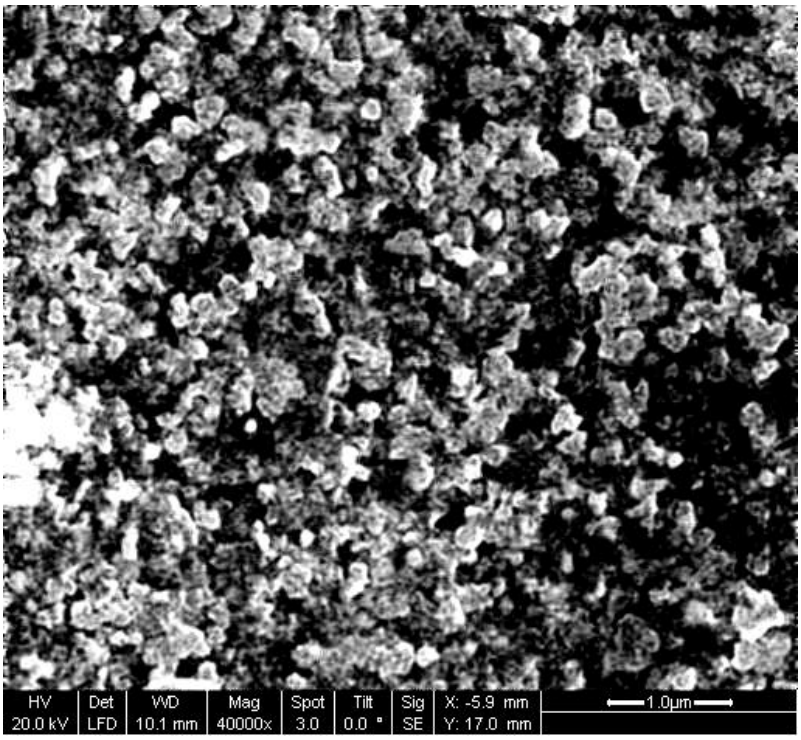

Figure 73: Typical microstructure of CB and PE of tested samples (RT, aging, etched by Argon ions)

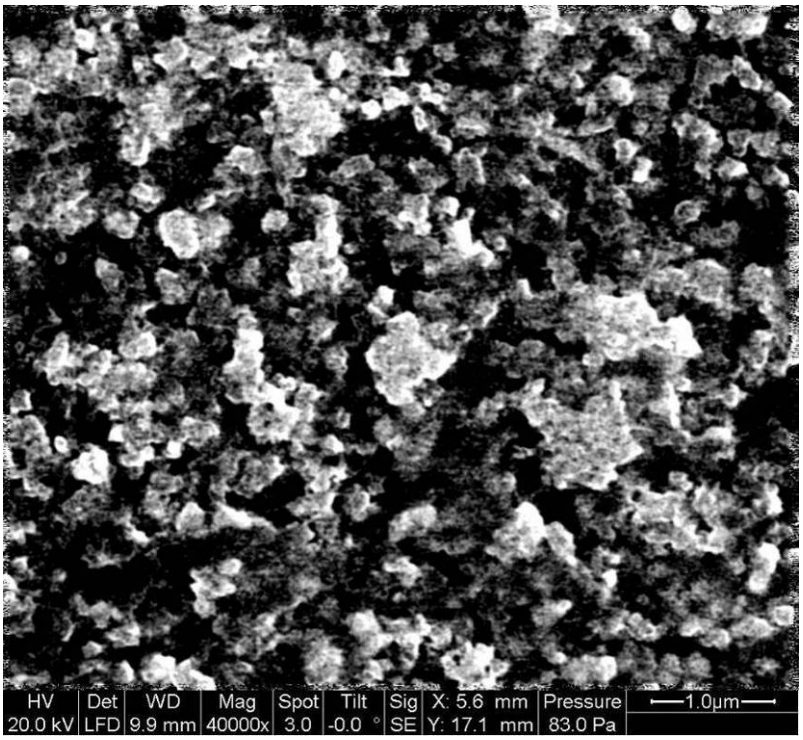

Figure 74: Typical microstructure of CB and PE of tested samples (RT, trip cycle, etched by Argon ions)

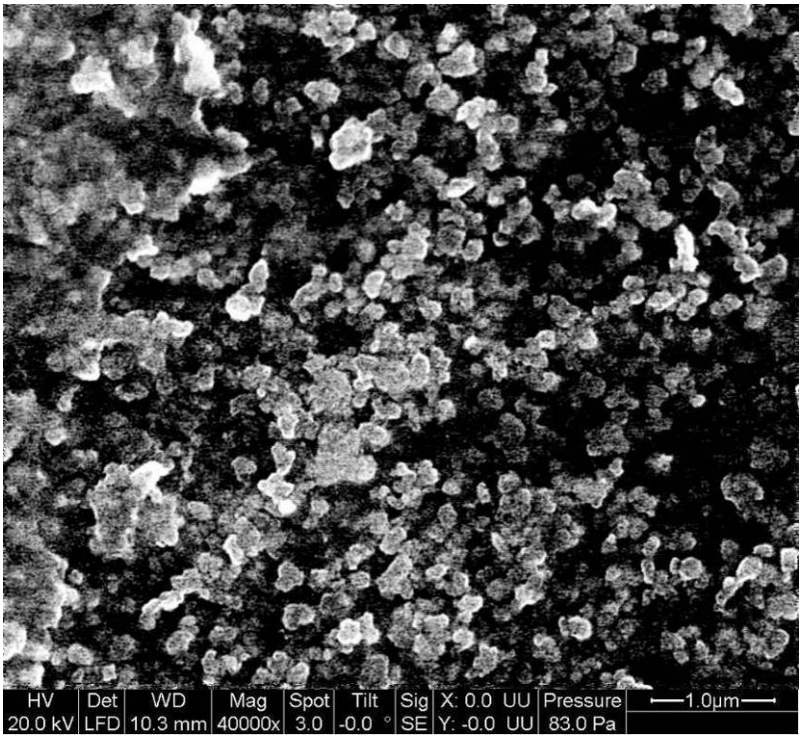

Figure 75: Typical microstructure of CB and PE of tested samples (60 °C, aging, etched by Argon ions)

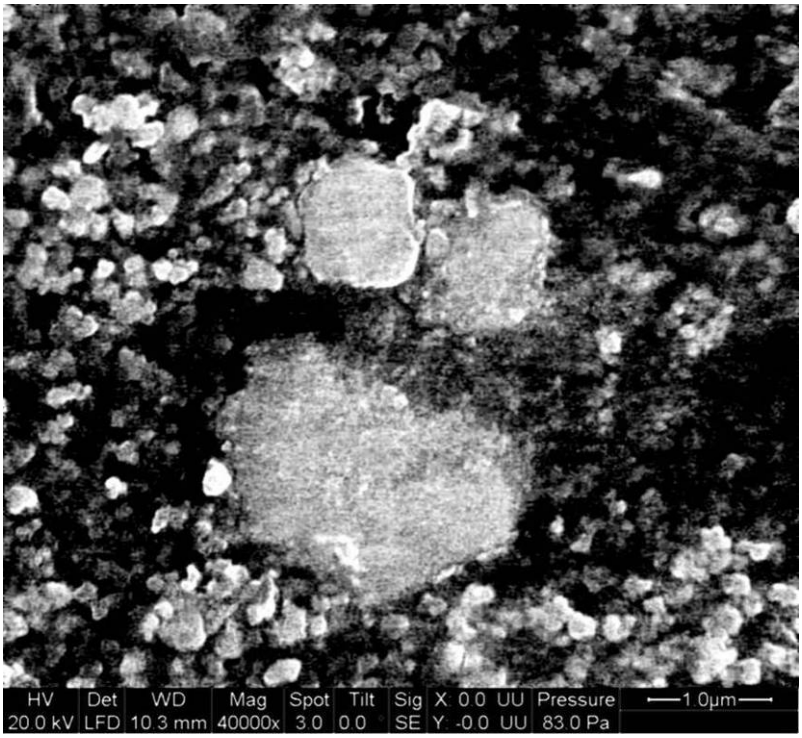

Figure 76: Typical microstructure of CB and PE of tested samples (60 °C, trip cycle, etched by Argon ions)

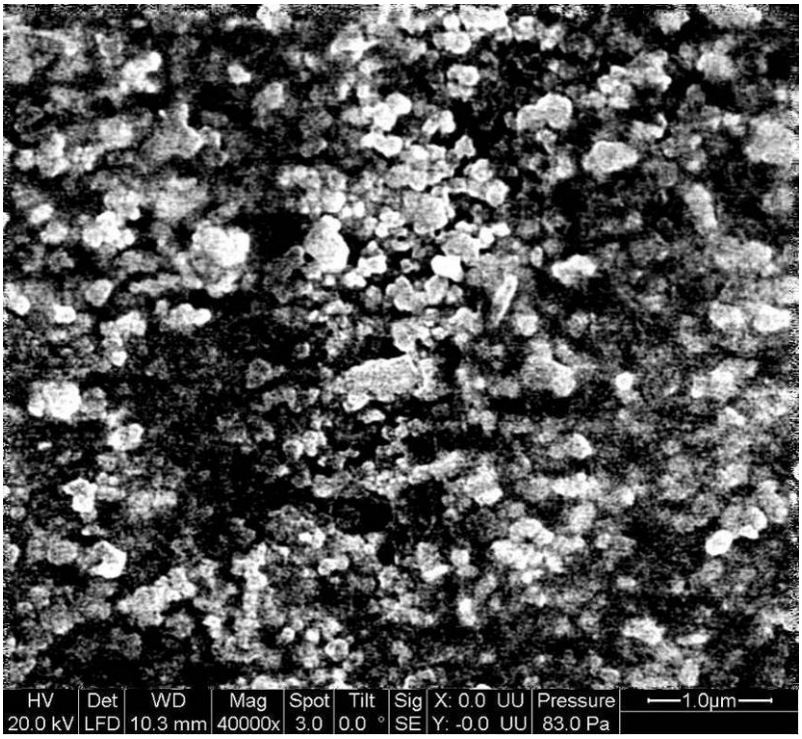

Figure 77: Typical microstructure of CB and PE of tested samples (85 °C, aging, etched by Argon ions)

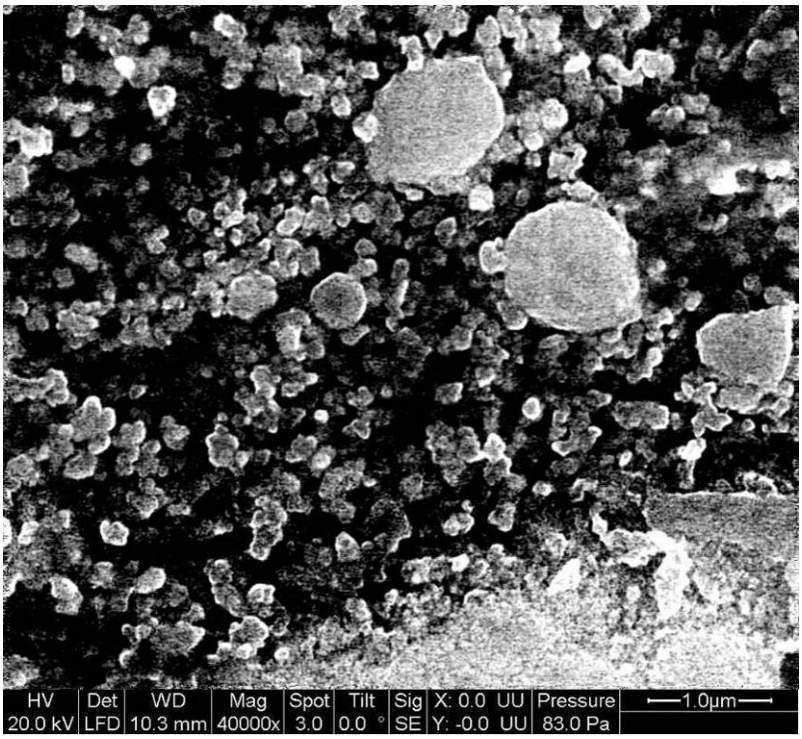

Figure 78: Typical microstructure of CB and PE of tested samples (85 °C, trip cycle, etched by Argon ions)

Appendix B: Anomaly Detection Results by CVSPRT

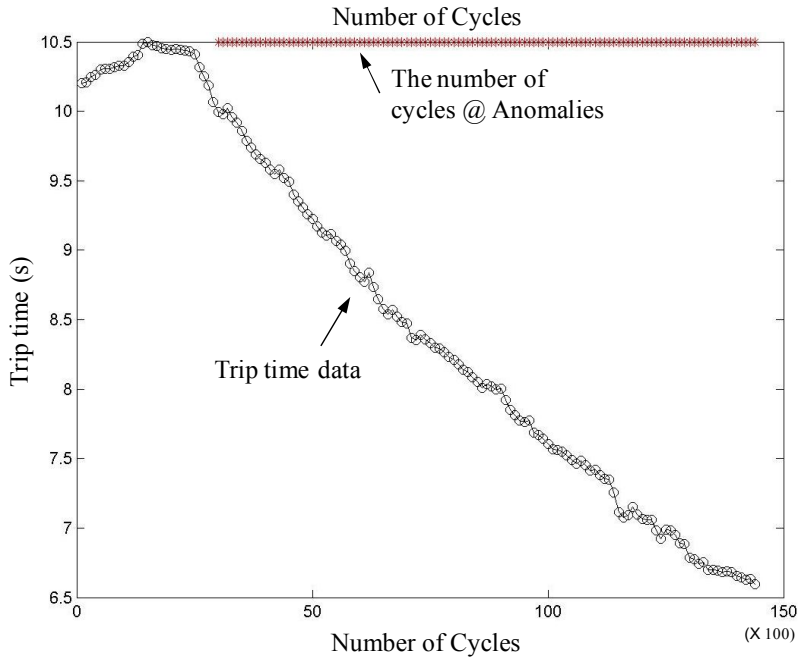

Figure 79: Anomaly detection results based on trip time (-10 °C, trip cycle)

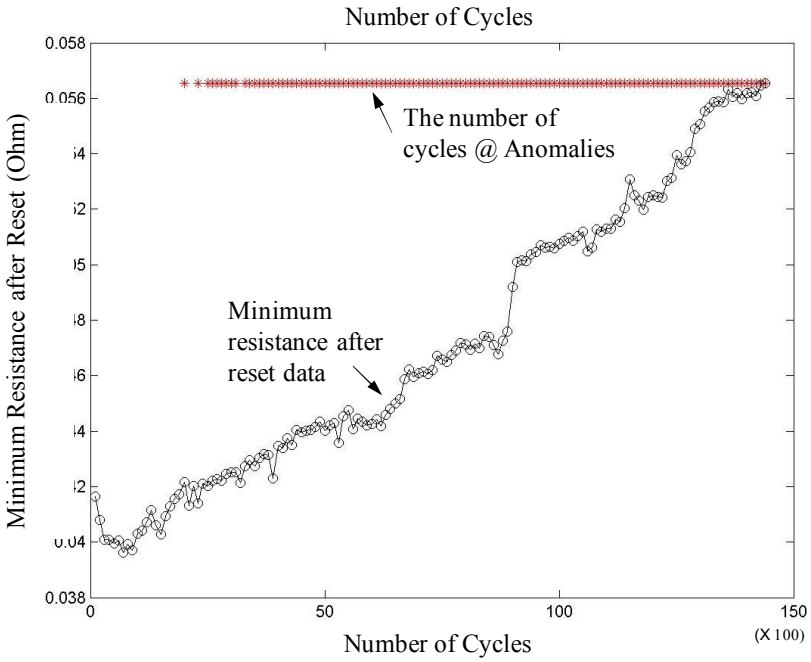

Figure 80: Anomaly detection results based on min. resistance after reset (-10 °C, trip cycle)

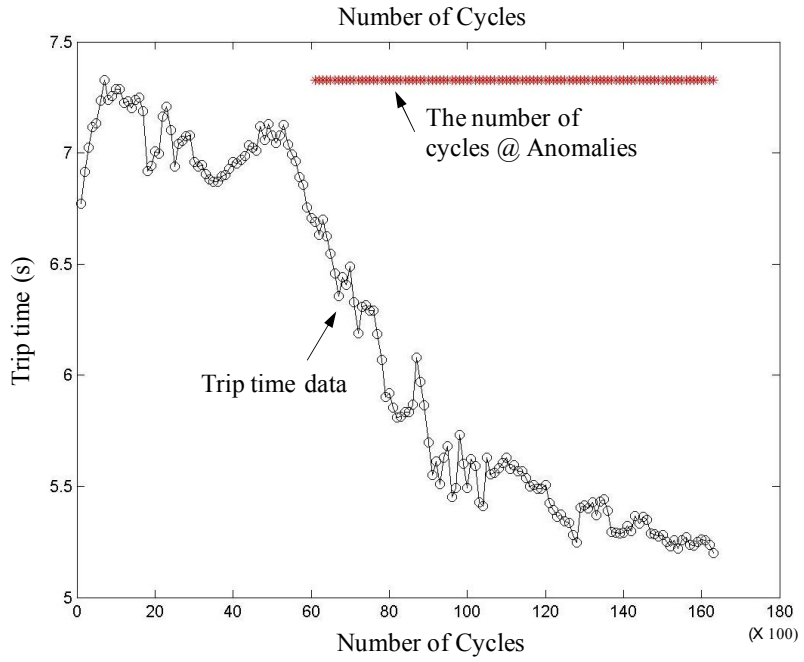

Figure 81: Anomaly detection results based on trip time (RT, trip cycle)

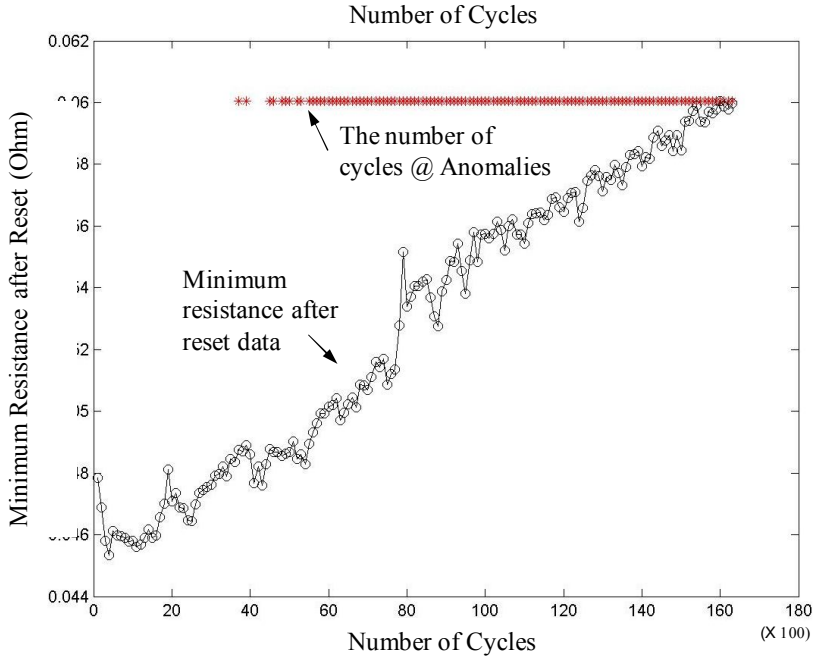

Figure 82: Anomaly detection results based on min. resistance after reset (RT, trip cycle)

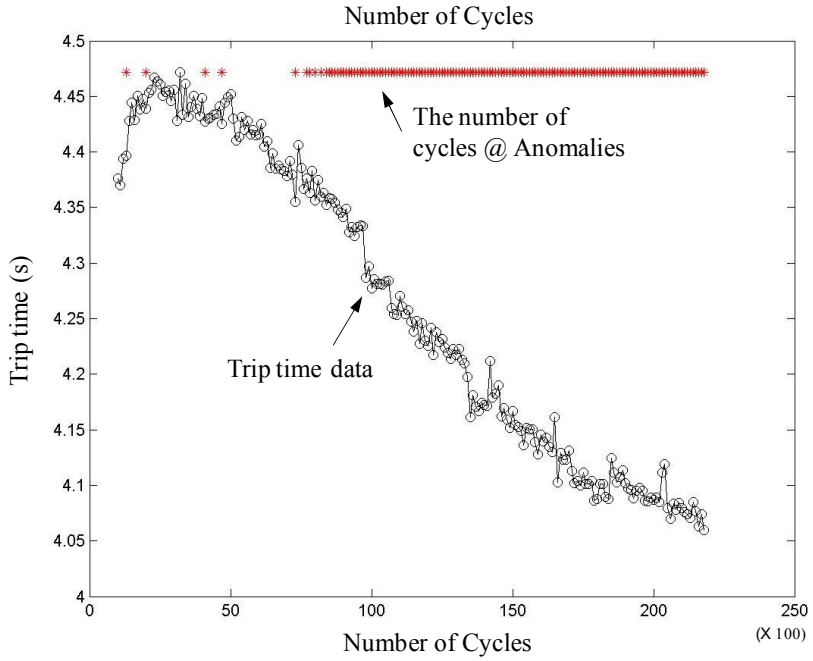

Figure 83: Anomaly detection results based on trip time (60 °C, trip cycle)

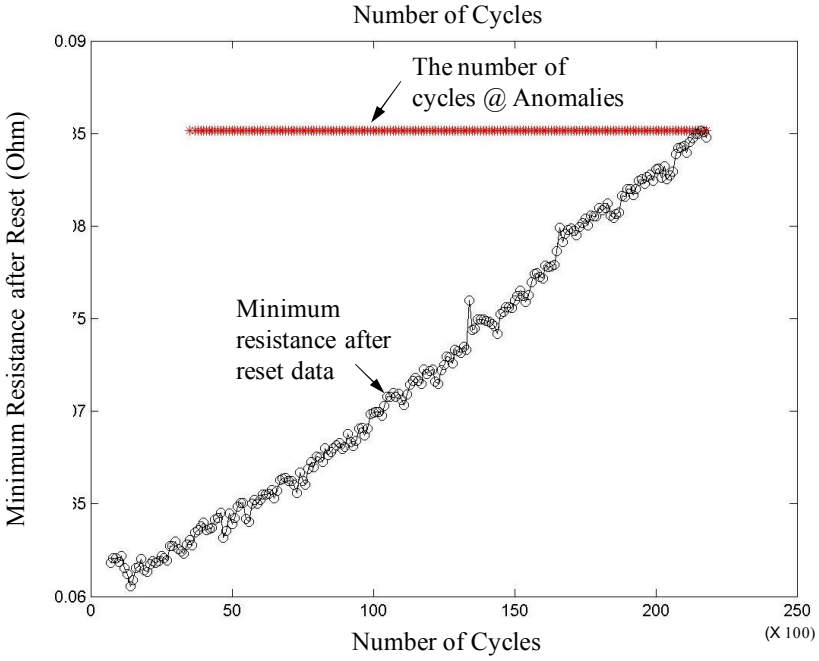

Figure 84: Anomaly detection results based on min. resistance after reset (60 °C, trip cycle)

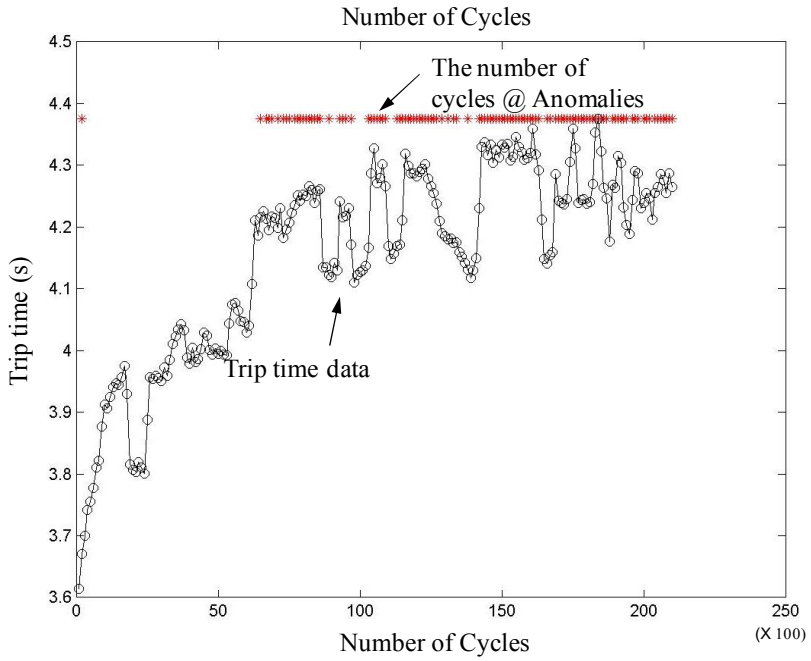

Figure 85: Anomaly detection results based on trip time (85 °C, trip cycle)

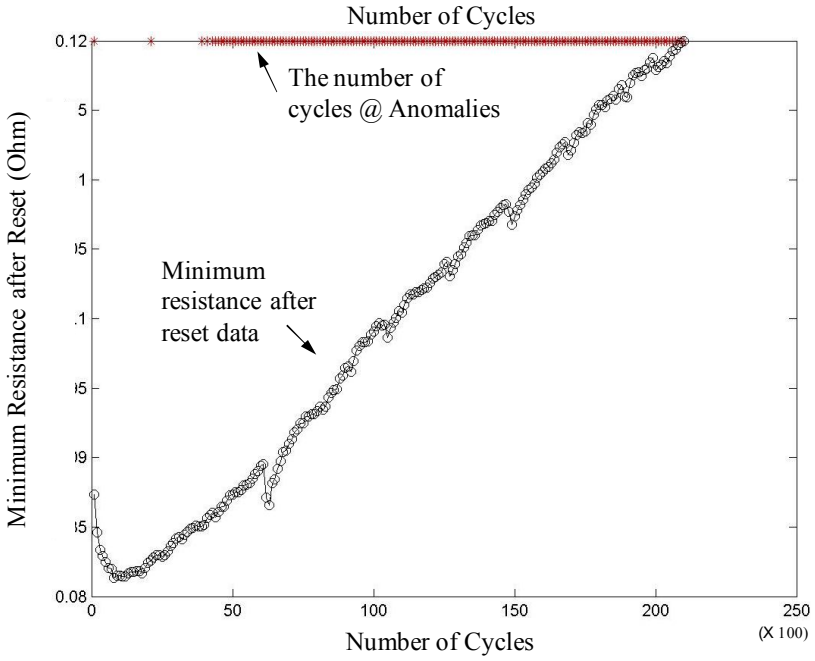

Figure 86: Anomaly detection results based on min. resistance after reset (85 °C, trip cycle)

Appendix C: 5-step-ahead and 10-step-ahead Predictions by MW-CVSVR

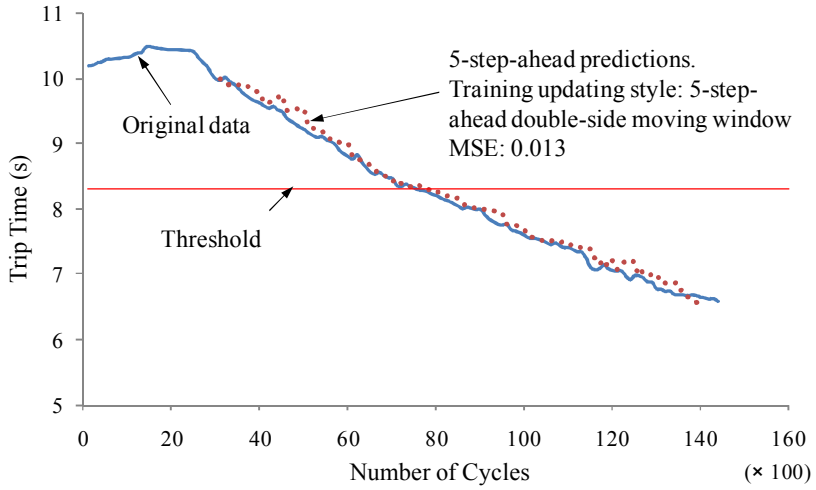

Figure 87: All 5-step-ahead predictions (-10°C,trip time, double-side MW)

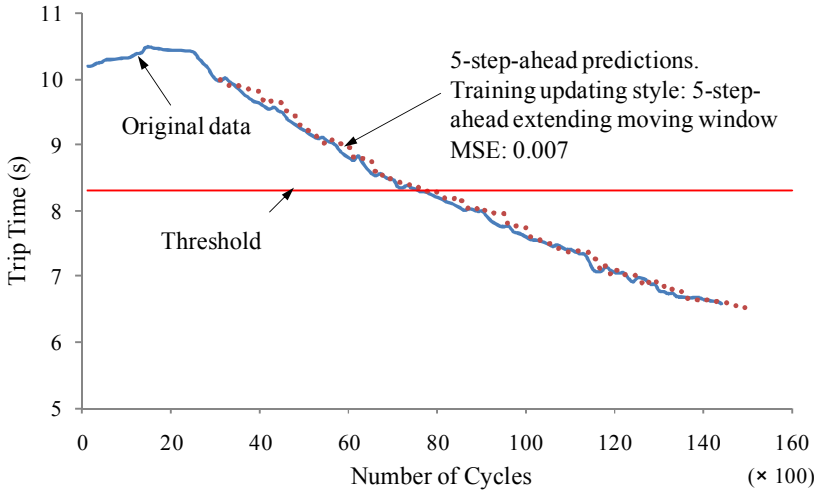

Figure 88: All 5-step-ahead predictions (-10°C, trip time, extending window)

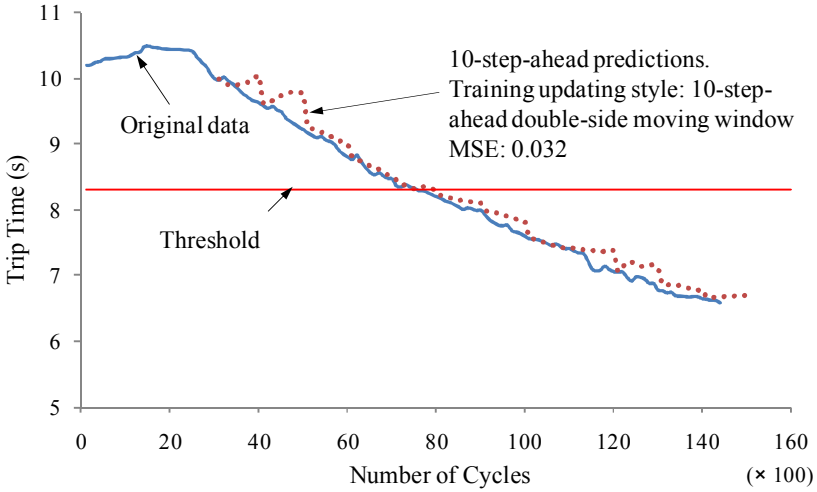

Figure 89: All 10-step-ahead predictions (-10°C,trip time, double-side MW)

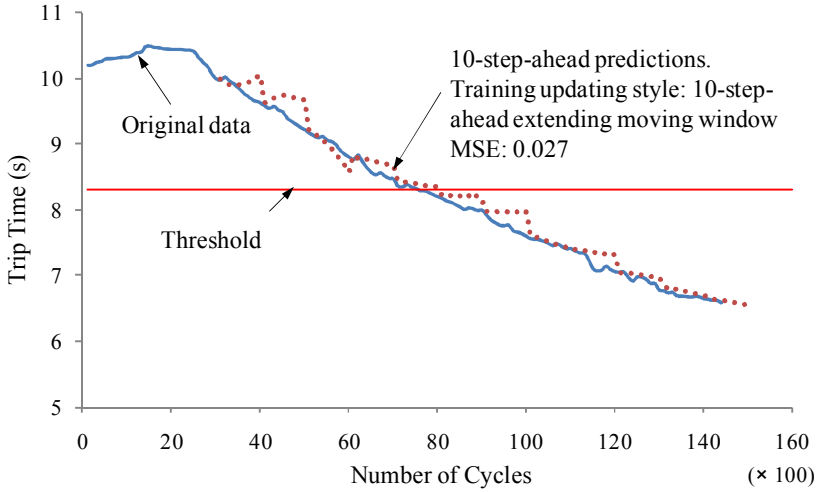

Figure 90: All 10-step-ahead predictions (-10°C,trip time, extending window)

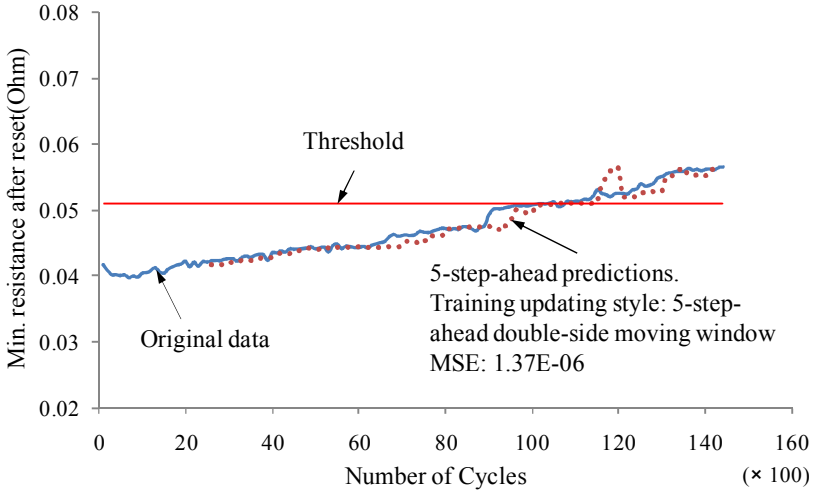

Figure 91: All 5-step-ahead predictions (-10°C, min. resistance after reset, double-side MW)

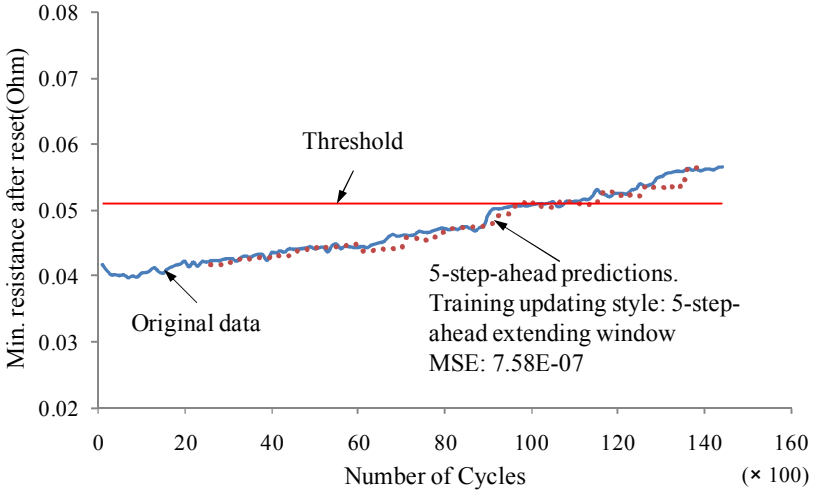

Figure 92: All 5-step-ahead predictions (-10°C, min. resistance after reset, extending window)

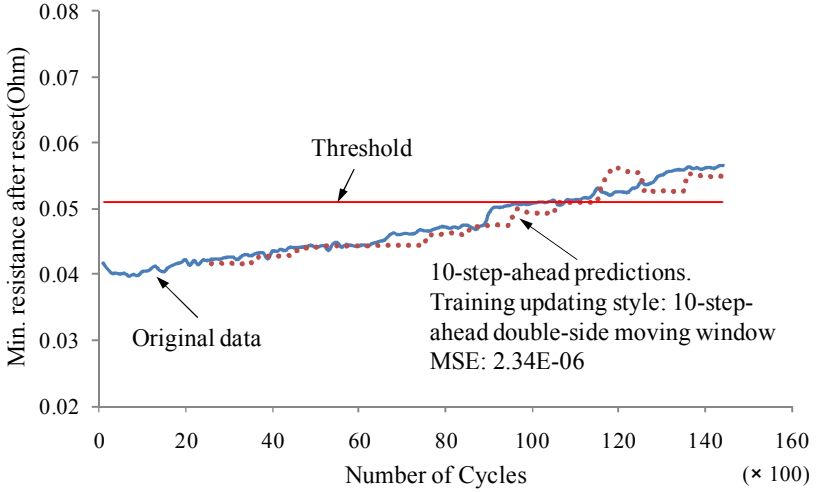

Figure 93: All 10-step-ahead predictions (-10°C, min. resistance after reset, double-side MW)

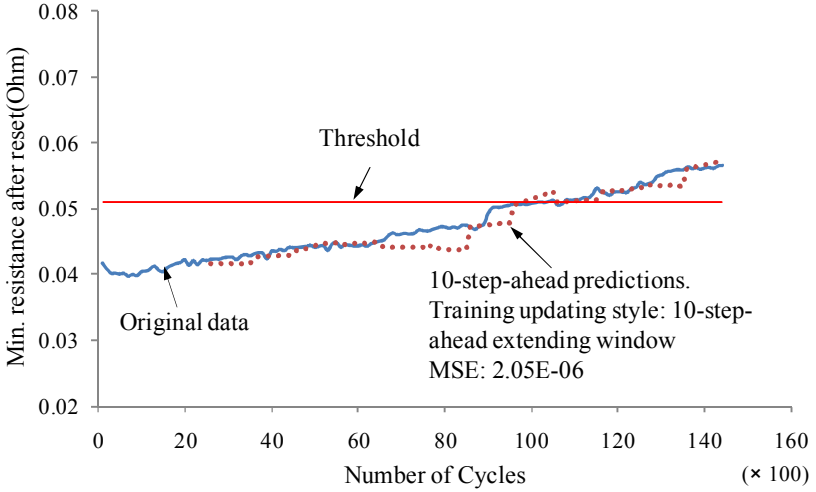

Figure 94: All 10-step-ahead predictions (-10°C, min. resistance after reset, extending window)

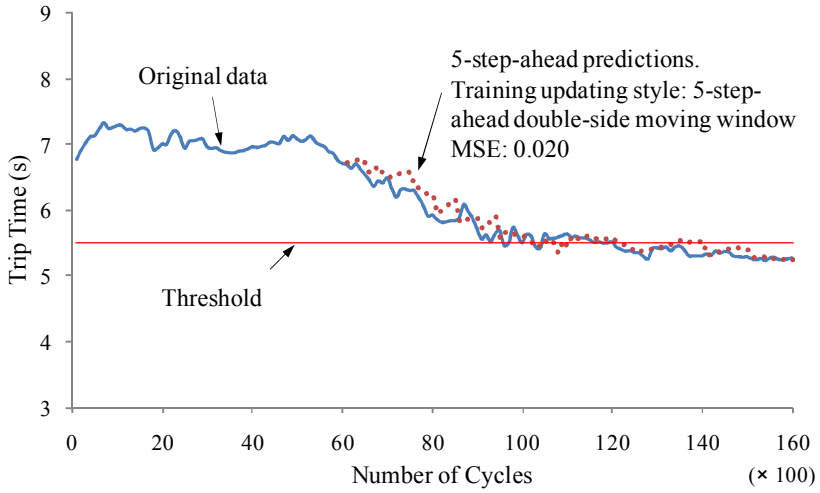

Figure 95: All 5-step-ahead predictions (RT, trip time, double-side MW)

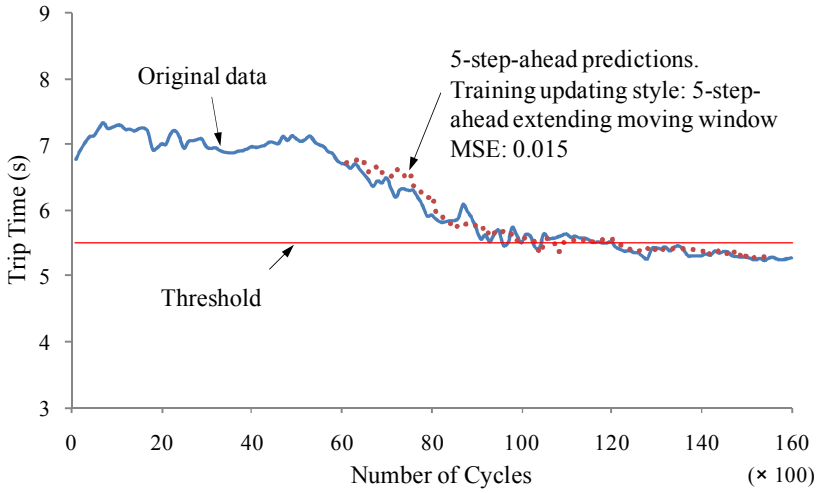

Figure 96: All 5-step-ahead predictions (RT, trip time, extending window)

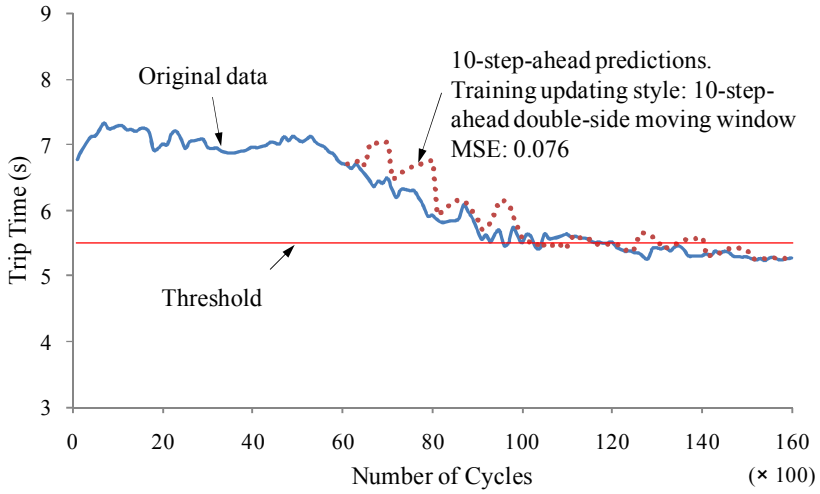

Figure 97: All 10-step-ahead predictions (RT, trip time, double-side MW)

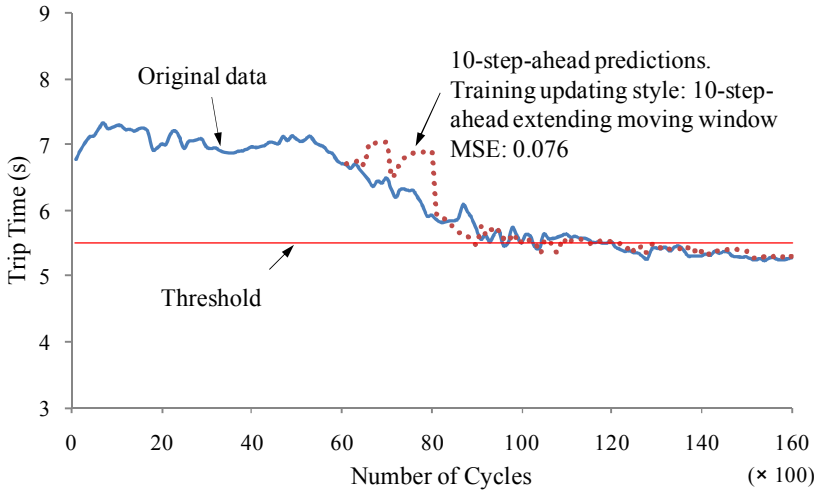

Figure 98: All 10-step-ahead predictions (RT, trip time, extending window)

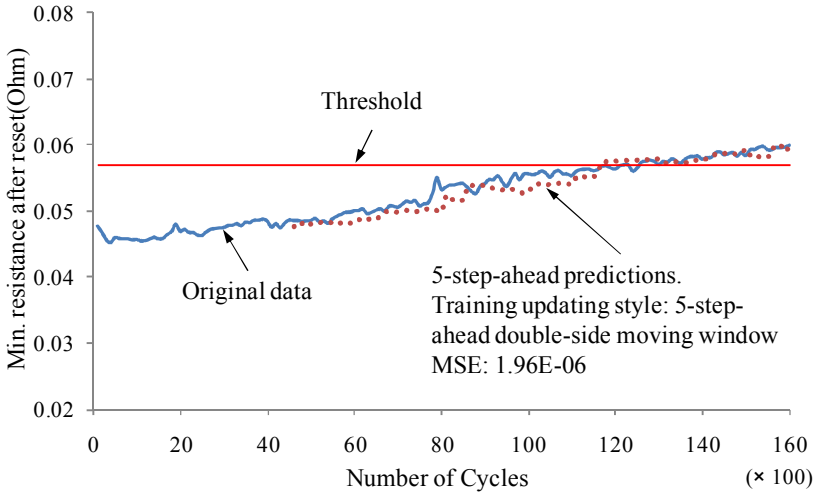

Figure 99: All 5-step-ahead predictions (RT, min. resistance after reset, double-side MW)

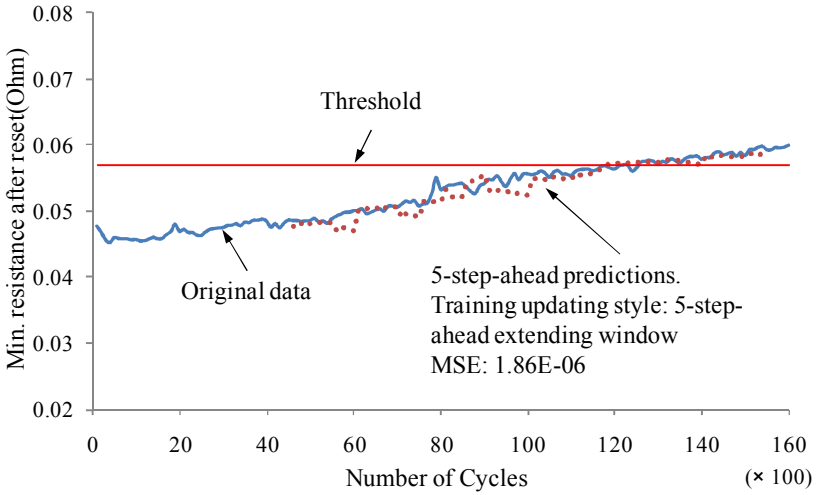

Figure 100: All 5-step-ahead predictions (RT, min. resistance after reset, extending window)

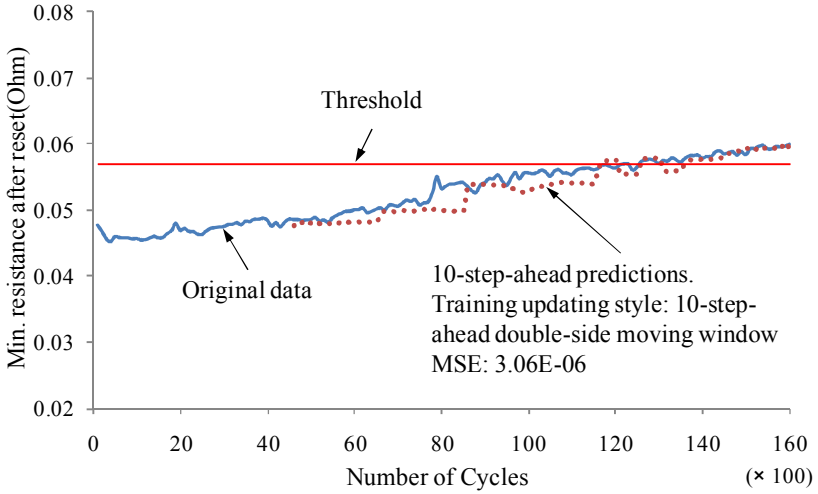

Figure 101: All 10-step-ahead predictions (RT, min. resistance after reset, double-side MW)

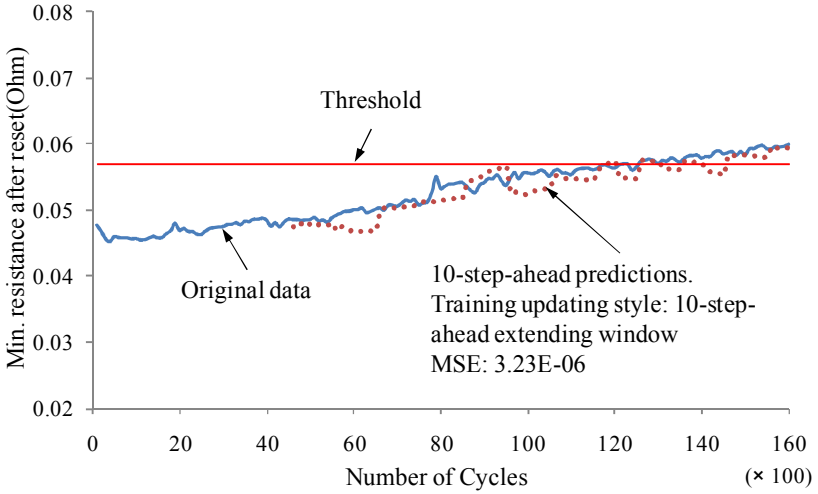

Figure 102: All 10-step-ahead predictions (RT, min. resistance after reset, extending window)

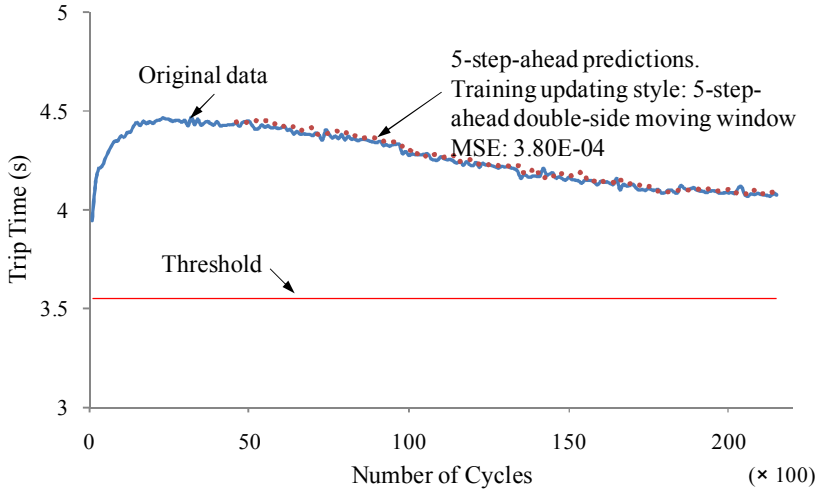

Figure 103: All 5-step-ahead predictions (60°C,trip time, double-side MW)

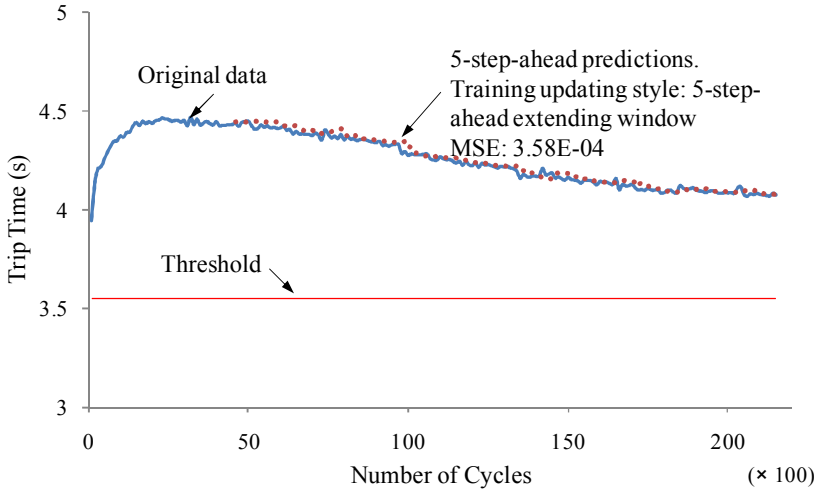

Figure 104: All 5-step-ahead predictions (60°C, trip time, extending window)

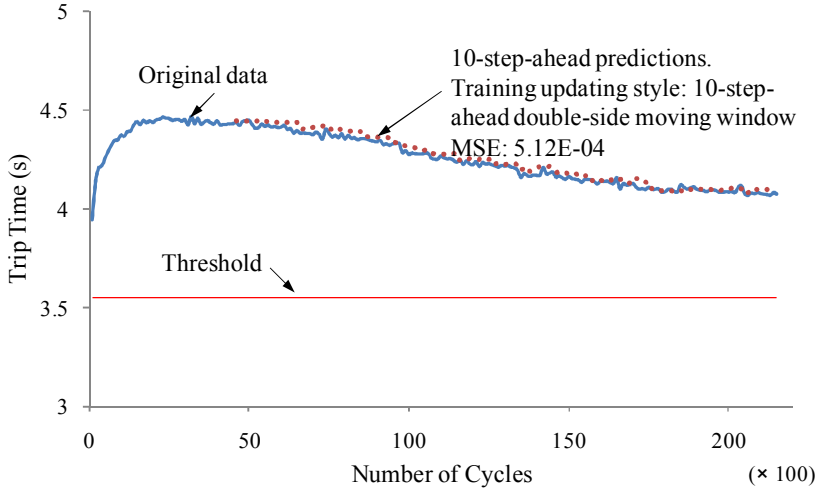

Figure 105: All 10-step-ahead predictions (60°C,trip time, double-side MW)

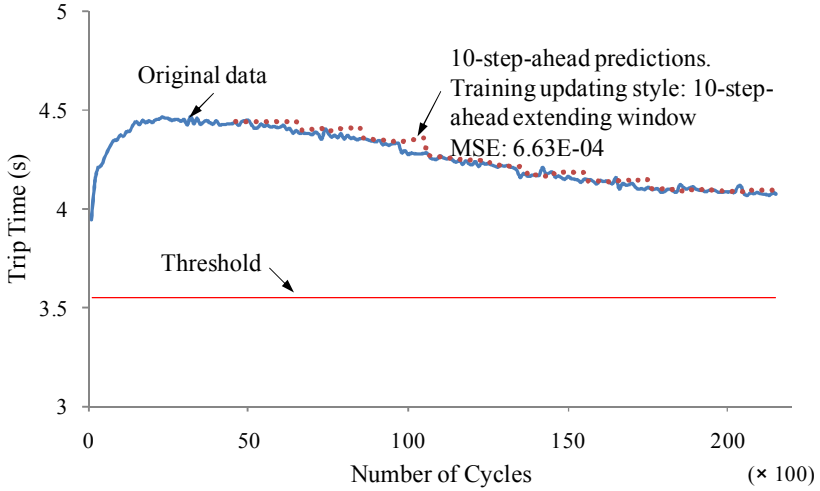

Figure 106: All 10-step-ahead predictions (60°C,trip time, extending window)

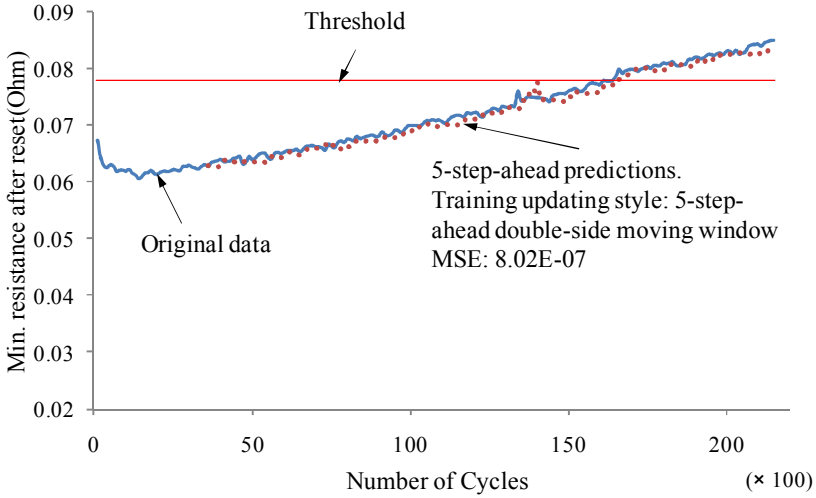

Figure 107: All 5-step-ahead predictions (60°C, min. resistance after reset, double-side MW)

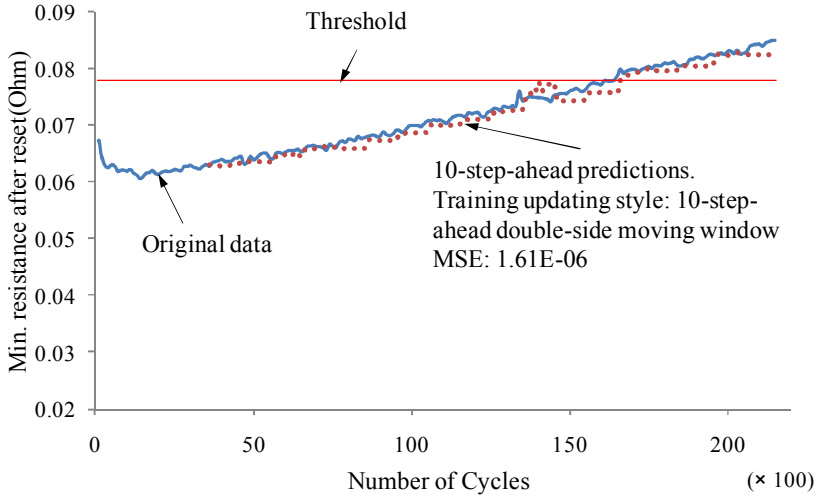

Figure 108: All 5-step-ahead predictions (60°C, min. resistance after reset, extending window)

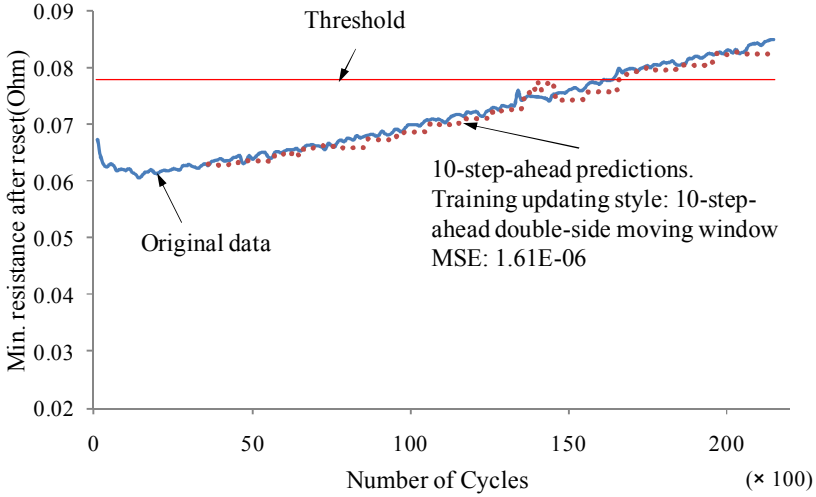

Figure 109: All 10-step-ahead predictions (60°C, min. resistance after reset, double-side MW)

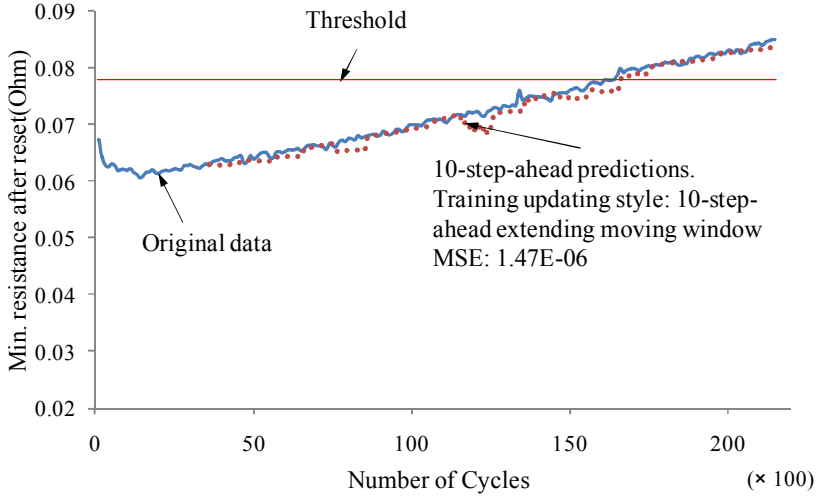

Figure 110: All 10-step-ahead predictions (60°C, min. resistance after reset, extending window)

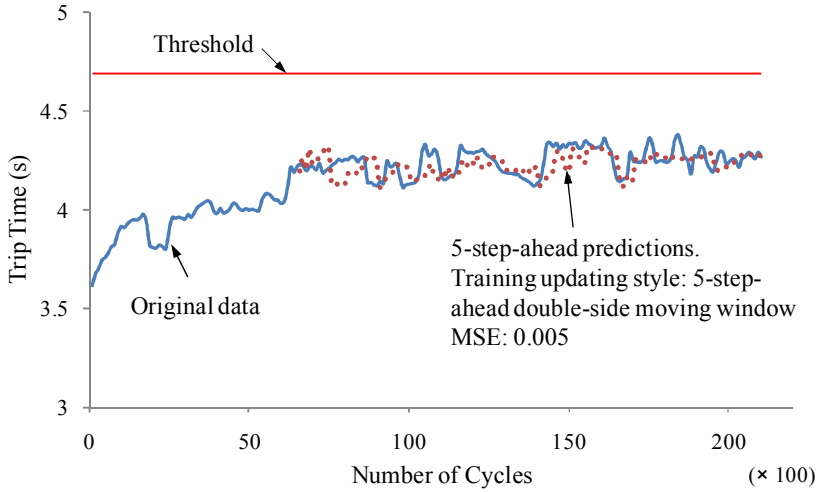

Figure 111: All 5-step-ahead predictions (85°C,trip time, double-side MW)

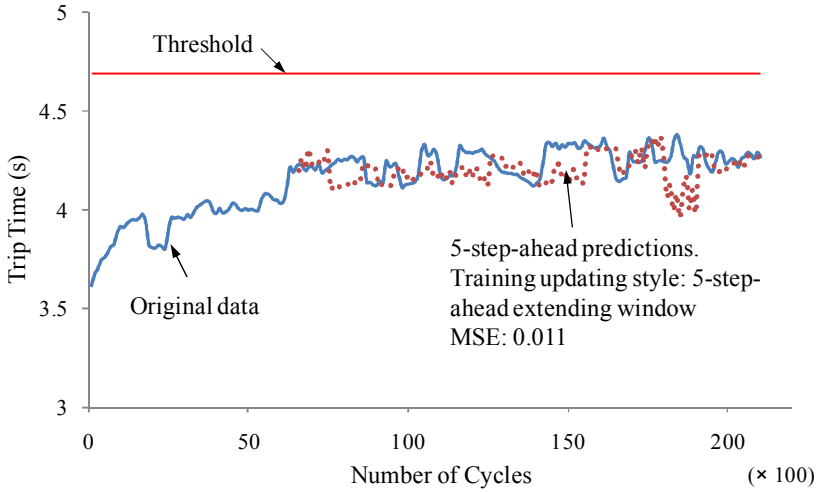

Figure 112: All 5-step-ahead predictions (85°C, trip time, extending window)

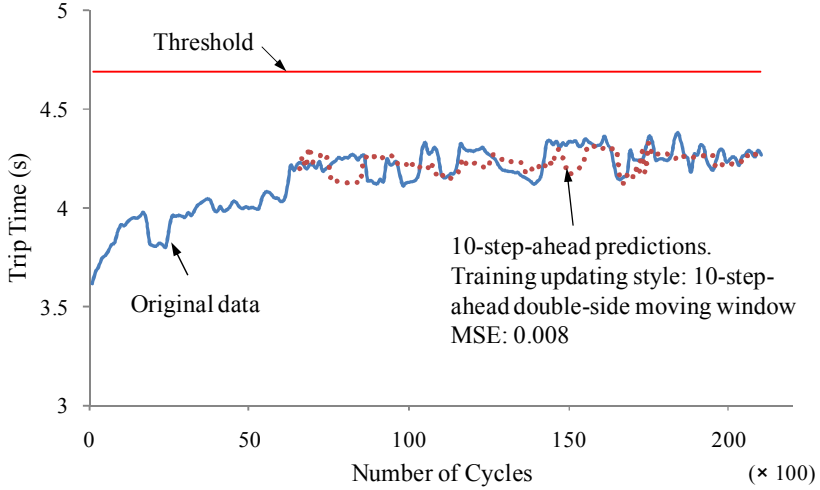

Figure 113: All 10-step-ahead predictions (85°C,trip time, double-side MW)

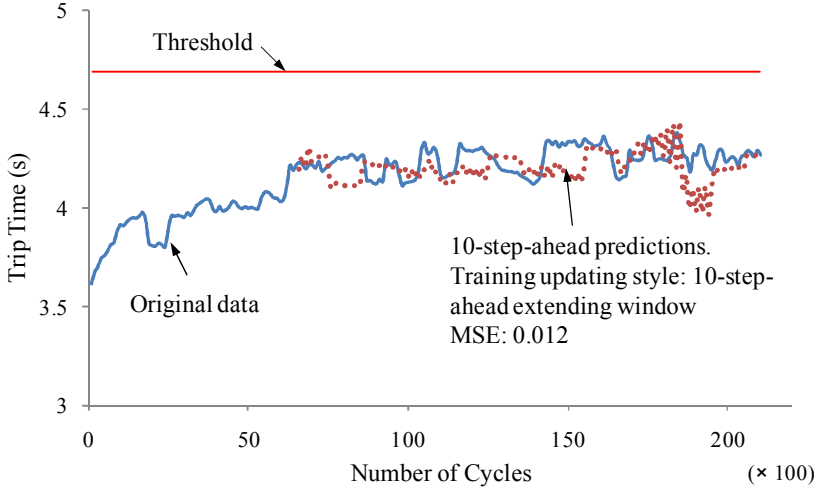

Figure 114: All 10-step-ahead predictions (85°C,trip time, extending window)

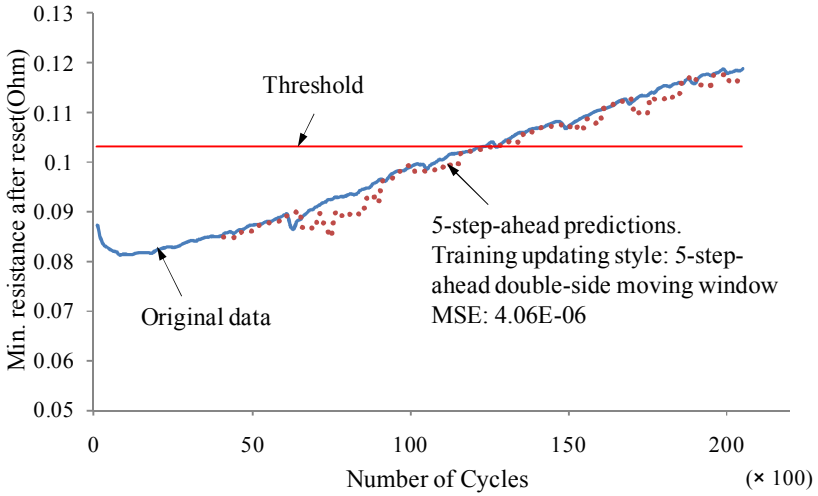

Figure 115: All 5-step-ahead predictions (85°C, min. resistance after reset, double-side MW)

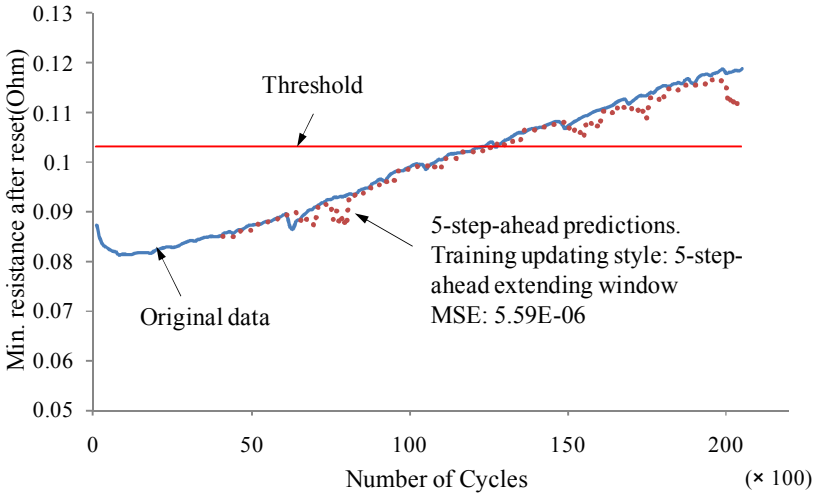

Figure 116: All 5-step-ahead predictions (85°C, min. resistance after reset, extending window)

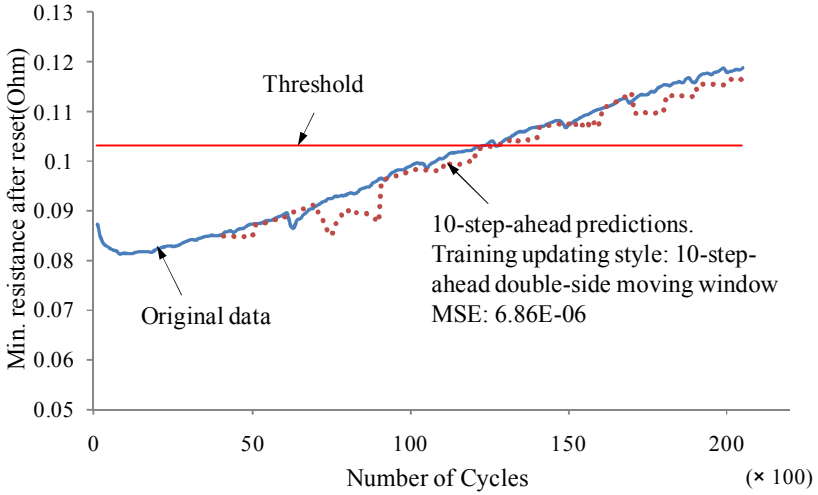

Figure 117: All 10-step-ahead predictions (85°C, min. resistance after reset, double-side MW)

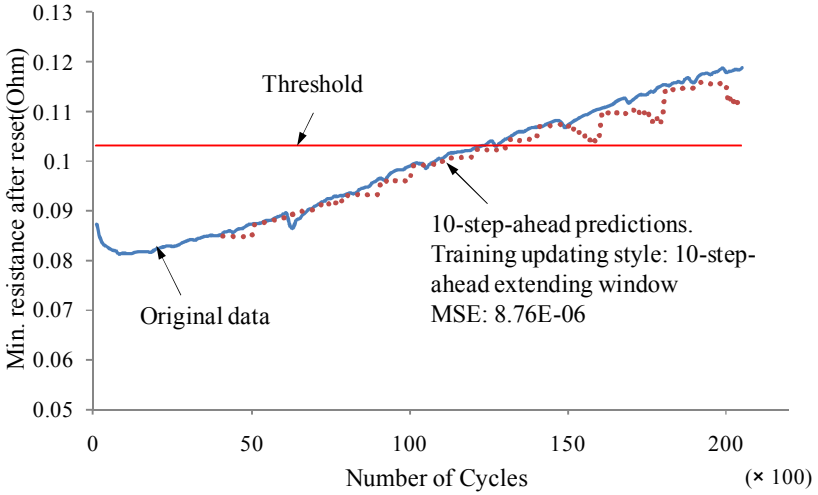

Figure 118: All 10-step-ahead predictions (85°C, min. resistance after reset, extending window)

References

[1]. D. Wei, T. Zhao, and X. Yi, "Resistivity–Volume Expansion Characteristics of Carbon Black-loaded Polyethylene," Journal of Applied Polymer Science, Vol.77, pp. 53–58, 2000.

[2]. S. Luo, and C. Wong, "Study on Effect of Carbon Black on Behavior of Conductive Polymer Composites with Positive Temperature Coefficient," IEEE Trans. on Component and Packaging Technologies, Vol.23, No.1, pp. 151-155, 2000.

[3]. M. Gorniak, and R.Masnicki, "The Estimation of the Polymer Fuses Features," IMEKO TC-4, 2007.

[4]. Tyco Electronics, "Fundamentals of PolySwitch Overcurrent and Overtemperature Devices," Technical paper, 2008.

[5]. Bourns University: Multifuse® Resettable Fuses, http://www.ruf-electronics.com/bu/index2_3.asp

[6]. UL 1434, Standard for Safety for Thermistor-Type Devices, August, 2002.

[7]. S. Cheng, K. Tom, and M. Pecht, "Failure Precursors for Polymer Resettable Fuses," IEEE Transactions on Devices and Materials Reliability, Vol.10, Issue.3, pp.374-380, 2010.

[8]. S. Cheng, M. Azarian, and M. Pecht, "Sensor System for Prognostics and Health Monitoring," Sensors, No. 10, pp.5774-5797, 2010.

[9]. M. Pecht, *Prognostics and Health Management of Electronics*. New York: Wiley-Interscience, 2008.

[10]. B. F. Xi, K. Chen, F. Liu, C. Xu, and Q. Zhang, "The Advance in Theory

Research of PTC Properties of Polymer/Carbon black Composites," Proceedings of 1998 International Symposium on Electrical Insulating Materials, pp. 325-328, Toyohashi, Japan,1998.

[11]. F. Kohler, "Resistance Element," US patent 3,243,753, Mar. 29, 1966.

[12]. F. Doljack, "PolySwitch PTC Devices-A New Low-resistance Conductive Polymer-based PTC Device for Overcurrent Protection," IEEE Transactions on Components, Hybrids, and Manufacturing Technology, vol.CHMT-4, pp. 372-378, 1981.

[13]. B. Xi, and G. Chen, "The Mechanism of Electrical Conduction in Polyethylene/Carbon Black Composite," Proc. of the 6th International Conference on Properties and Applications of Dielectric Materials, pp 1015-1018, Xi'an China, 2000.

[14]. J. Fournier, G. Boiteux, G. Seytre, and G. Marichy, "Positive Temperature Coefficient Effect in Carbon Black/Epoxy Polymer Composites," Journal of Materials Science Letters, Vol. 16, pp.1677-1679, 1997.

[15]. H. Horibe, T. Kamimura, and K. Yoshida, "Electrical Conductivity of Polymer Composites Filled with Metal," Japanese. Journal of Applied Physics, Vol. 44, No. 4A, pp. 2025-2029.

[16]. R. Striimpler, J. Skindhoj, J. Glatz-Reichenbach, J.H.W. Kuhlefelt and F. Perdoncin, "Novel Medium Voltage Fault Current Limiter Based on Polymer PTC Resistors," IEEE Trans. Power Delivery. Vol. 14, No.2, pp. 425–430, 1999.

[17]. K. Ohe and Y. Natio, "A New Resistor Having an Anomalously Large

Positive Temperature Coefficient," Japanese Journal of Applied Physics, Vol. 10, No.1, pp. 99–108, 1971.

[18]. C. Klason and J. Kubat, "Anomalous Behavior of Electrical Conductivity and Thermal Noise in Carbon Black-containing Polymers at Tg and Tm," Journal of Applied Polymer Science, Vol.19, I3, pp. 831-845, 1975.

[19]. H. Allak, A. Brinkman, and J. Woods, "I-V Characteristics of Carbon Black-loaded Crystalline Polyethylene," Journal of Materials Science, Vol. 28, No.1, pp. 117-120,1993.

[20]. MF-RX/72 Series-PTC Resettable Fuses, http://www.bourns.com/pdfs/mfrx72.pdf, latest accessed on March 7, 2011.

[21]. J. Huang, "Carbon Black Filled Conducting Polymers and Polymer Blends," Advances in Polymer Technology, Vol. 21, No. 4, pp. 299–313, 2002.

[22]. W. Zhang, A. Dehghani-Sanij, and R. Blackburn, "Carbon Based Conductive Polymer Composites," Journal of Materials Science, Volume 42, Number 10, pp. 3408-3418, 2007.

[23]. K. P. Sau, T. K Chaki, and D. Khastgir, "Conductive Rubber Composites from Different Blends of Ethylene-Propylene-Diene Rubber and Nitrile Rubber," Journal of Materials Science, Vol. 32, No. 21, pp. 5717-5724, 1997.

[24]. M. Narkis and A. Vaxman, "Resistivity Behavior of Filled Electrically Conductive Crosslinked Polyethylene," Journal of Applied Polymer Science, Vol. 29, Issue 5, pp.1639–1652, 1984.

[25]. S. Bhattacharya, *Metal Filled Polymers,* Marcel Dekker, New York, 1986.

[26]. E. Sichel, *Carbon Black-Polymer Composites,* Marcel Dekker, New York,

1982.

[27]. K. Miyasaka, K. Watanabe, E. Jojima, H. Aida, M. Sumita and K. Ishikawa, "Electrical Conductivity of Carbon-polymer Composites as a Function of Carbon Content," Journal Material Science, Vol. 17, No.6, pp. 1610–1616, 1982.

[28]. F. Lux, "Models Proposed to Explain the Electrical Conductivity of Mixtures Made of Conductive and Insulating Materials," Journal of Material Science, Vol. 28, No.2, pp.285-301, 1993.

[29]. J. Donnet, R. Bansal and M. Wang, *Carbon Black Science and Technology (2nd ed.)*, Marcel Dekker, New York, 1993.

[30]. I. Mironi-Harpaz and M.Narkis, "Electrical Behavior and Structure of Polypropylene/Ultrahigh Molecular Weight Polyethylene/Carbon Black Immiscible Blends," Journal of Applied Polymer Science, Vol. 81, pp.104-115, 2001.

[31]. J. Donnet, "Fifty Years of Research and Progress on Carbon Black," Carbon, Vol. 32, Issue 7, pp.1305 1310, 1994.

[32]. X. Bourrat, "Electrically Conductive Grades of Carbon Black: Structure and Properties," Carbon, Vol. 31, No.2, pp.287-302, 1993.

[33]. B. Xi, G. Chen, and A.E. Davies, "Investigation into the Positive Temperature Coefficient Effect in Polyethylene/Carbon Black Composites,"8th International Conference on Dielectric Materials, Measurements and Applications, pp. 480-484, 2000.

[34]. M. Sumita, S. Asai, N. Miyadera, E. Jojima and K. Miyasaka, "Electrical

Conductivity of Carbon Black Filled Ethylene-Vinyl Acetate Copolymer as a Function of Vinyl Acetate Content," Colloid & Polymer Science, Vol. 264, No. 3, pp.212-217, 1986.

[35]. J. Huang and C. Wu, "Processability, Mechanical Properties, and Electrical Conductivities of Carbon Black-filled Ethylene-vinyl Acetate Copolymers," Advances in Polymer Technology, Vol. 19, No. 2, PP.132-139, 2000.

[36]. R. Tchoudakov, O. Breuer, M. Narkis, and A. Siegmann, "Conductive Polymer Blends with Low Carbon Black Loading: Polypropylene/Polyamide," Polymer Engineering & Science, Vol. 36, pp. 1336–1346, 1996.

[37]. S. Wu, *Polymer Interface and Adhesion*, Marcel Dekker: New York, 1982.

[38]. H. He, P. Deng, L. Dong, and J. Sun, "LDPE/Carbon Black Conductive Composites: Influence of Radiation Crosslinking on PTC and NTC Properties," Journal of Applied Polymer Science, Vol. 85, pp.2742-2749, 2002.

[39]. J. Oakey, D.W.M. Marr, K.B. Schwartz, and M. Wartenberg, "Influence of Polyethylene and Carbon black Morphology on Void Formation in Conductive Composite Materials: A SANS Study," Macromolecules, 32, pp.5399-5404, 1999.

[40]. E. Park, "Resistivity and Thermal Reproducibility of High-Density Polyethylene Heaters Filled with Carbon Black," Macromolecular Materials and Engineering, 291, pp.690-696, 2006.

[41]. S. Huang, J. lee, C. Ha, "Polymeric Positive-Temperature-Coefficient Materials: Dynamic Curing Effect," Colloid & Polymer Science, Vol. 282,

pp.575-582, 2004.

[42]. Z. Li, X. Xu, A. Lu, K. Shen, R. Huang, and M. Yang, "Carbon black/poly(ethylene terephthalate)/polyethylene Composite with Electrically Conductive *in-situ* Microfiber Network," Carbon. Vol. 42, No. 2, pp. 428-432, 2004.

[43]. X. Xu, Z. Li, R. Yu, A. Lu, M. Yang, and R. Huang, "Formation of *in-situ* CB/PET Microfibers in CB/PET/PE Composites by Slit Die Extrusion and Hot Stretching," Macromolecular Materials and Engineering, Volume 289, Issue 6, pp. 568-575, 2004.

[44]. T. M. Tawalbeh, S. Saq'an, S. F. Yasin, A. M. Zihlif, and G. Ragosta, "Low Temperature Electrical Conductivity of Low-density Polyethylene/carbon Black Composites," Journal of Materials Science: Materials in Electronics, Vol. 16, No. 6, pp. 351-354, 2005.

[45]. H. Yui, G. Wu, H. Sano, M. Sumita, and K. Kino, "Morphology and Electrical conductivity of Injection-Molded Polypropylene/carbon Black Composite with Addition of High-Density Polyethylene," Polymer, Vol. 47, pp.3599-3608, 2006.

[46]. H. Horibe, T. Kaimura, and K. Yoshida, "Electrical Conductivity of Polymer Composites Filled with Carbon Black," Japanese Journal of Applied Physics, Vol.44, No.4A, pp.2025-2029, 2005.

[47]. C.P. Wong and S. Luo, "Investigation on Effect of Carbon Black and Polymer Matrix on Conductive Polymer Composites with Positive Temperature Coefficient," International Symposium on Advanced Packaging Materials, pp.

343-348, 2000.

[48]. M. Stevens, *Polymer Chemistry 3rd Ed*, Oxford University Press, 1999.

[49]. H. White, and A. Grover, "Reliability of Surface-Mount PPTC Circuit Protection Devices," Proceedings of Annual Reliability and Maintainability Symposium, 1997, pp: 229-236.

[50]. J. Gu, N. Vichare, T. Tracy, and M. Pecht, "Prognostics Implementation Approaches for Electronics," Reliability and Maintainability Symposium, pp. 101-106. Orlando, FL, 2007.

[51]. S. Mathew, D. Das, R. Rosenberger, and M. Pecht, "Failure Mechanism Based Prognostics," Proceedings of the 1st International Conference on Prognostics and Health Management, Denver, CO, Oct. 6-9, 2008.

[52]. S. Kumar, M. Torres, M. Pecht, and Y.C. Chan, "A Hybrid Prognostics Methodology for Electronics Systems," Special Session on Computational Intelligence for Anomaly Detection, Diagnosis, and Prognosis, IEEE World Congress on Computational Intelligence (WCCI 2008), Hong Kong, June 1-6, 2008.

[53]. M. Pecht, M. and R. Jaai, "A Prognostics and Health Management Roadmap for Information and Electronics-Rich Systems," Microelectronics Reliability, Volume 50, Issue 3, pp. 317-323, 2010.

[54]. G.E. Box, G.M. Jenkins, and G.C. Reinsel, *Time Series Analysis Forecasting and Control, 4th edition*, John Wiley and Sons, New York, 2008.

[55]. S. Ho, and M. Xie, "The Use of ARIMA Models for Reliability Forecasting and Analysis," Computers & Industrial Engineering, Vol.35, pp.213–216,

1998.

[56]. S. Ho, M. Xie, and T. Goh, "A Comparative Study of Neural Network and Box-Jenkins ARIMA Modeling in Time Series Prediction," Computers & Industrial Engineering, Vol.42, pp.371–375, 2002.

[57]. K. Xu, M. Xie, L. Tang, S. Ho, "Application of Neural Networks in Forecasting Engine System Reliability," Applied Soft Computing, Vol. 2, pp.255–268, 2003

[58]. V.N. Vapnik. *The Nature of Statistical Learning Theory*. New York: Springer, 1995.

[59]. P.F. Pai and W.C. Hong, "Software Reliability Forecasting by Support Vector Machines with Simulated Annealing Algorithms," Journal of Systems and Software, Vol. 79, no. 6, pp. 747-755, 2006.

[60]. K.Y. Chen, "Forecasting Systems Reliability based on Support Vector Regression with Genetic Algorithms," Reliability Engineering & System Safety, Vol. 92, pp. 423- 432, 2007.

[61]. Y. Kuo and K. Lin, "Using Neural Network and Decision Tree for Machine Reliability Prediction," The International Journal of Advanced Manufacturing Technology, Vol. 50, No.9-12, pp.1243-1251, 2010.

[62]. Y. Freund and R. Schapire, "A Decision-theoretic Generalization of on-line Learning and an Application to Boosting," Journal of Computer and System Sciences, Vol. 55, No.1, pp.119–139, 1997.

[63]. S. Choi, C. Lee, J. Lee, J. Park, and I. Lee, "Fault Detection and Identification of Nonlinear Processes based on KPCA," Chemometrics and Intelligent

Laboratory Systems, Vol. 75, Issue 1, pp. 55-67, 2005.

[64]. J. Cho, J. Lee, S. Choi, D. Lee, and I. Lee, "Fault Identification for Process Monitoring Using Kernel Principal Component Analysis," Chemical Engineering Science, Vol. 60, pp.279–288, 2005.

[65]. Z. Xu, Y. Ji, and D. Zhou, "Real-time Reliability Prediction for a Dynamic System Based on the Hidden Degradation Process Identification," IEEE Trans. Reliability, Vol. 57, No.2, pp. 230-242, 2008.

[66]. B. Zhang, M. Chen, D. Zhou, and Z. Li, "Particle-filter-based Estimation and Prediction of Chaotic States," Chaos Solitons Fractals, Vol. 32, pp.1491–1498, 2007.

[67]. O.P. Yadav, N. Singh, R.B. Chinnam, and P.S. Goel, "A Fuzzy Logic based Approach to Reliability Improvement Estimation during Product Development," Reliability Engineering and System Safety, Vol. 80, pp. 63-74, 2002.

[68]. J. Gu and M. Pecht, "Prognostics and Health Management Using Physics of Failure," 54th annual Reliability and Maintainability Symposium (RAMS), Las Vegas, NV, Jan. 2008.

[69]. J. Gu, D. Barker, and M. Pecht, "Prognostics Implementation of Electronics under Vibration Loading," accepted by Microelectronics Reliability Journal.

[70]. S. Mishra, M. Pecht, T. Smith, I. McNee, and R. Harris, "Remaining Life Prediction of Electronic Products using Life Consumption Monitoring Approach," in Proceedings of the European Microelectronic Package Interconnection Symposium, pp. 136–142, Cracow, Poland, June 16–18,

2002.

[71]. L. Tian and A. Noore, "Dynamic Software Reliability Prediction: an Approach based on Support Vector Machines," International Journal of Reliability, Quality and Safety Engineering, vol. 12, no. 4, pp. 309-321, 2005.

[72]. W. Hong and P. Pai, "Predicting Engine Reliability by Support Vector Machines," International Journal of Advanced Manufacturing Technology, Vol. 28, No.1-2, pp. 154-161, 2006.

[73]. B. Yang and X. Li, "A Study on Software Reliability Prediction based on Support Vector Machines," IEEE International Conference on Industrial Engineering and Engineering Management, pp. 1176-1180, 2007.

[74]. Material declaration sheet, www.bourns.org/data/global/pdfs/mfrx72_mds.pdf, latest accessed on March 7, 2011.

[75]. S. Ganesan, V. Eveloy, D. Das, and M. Pecht, "Identification and Utilization of Failure Mechanisms to Enhance FMEA and FMECA," Proceedings of the IEEE Workshop on Accelerated Stress Testing & Reliability (ASTR), 2005.

[76]. M. Pecht and A. Dasgupta, "Physics-of-Failure: An Approach to Reliable Product Development", Journal of the Institute of Environmental Sciences, Vol. 38, pp. 30-34, 1995.

[77]. IEEE Standard 1413.1-2002, IEEE Guide for Selecting and Using Reliability Predictions Based on IEEE 1413, IEEE Standard, 2003.

[78]. M. Omastova, S. Podhradska, J. Prokes, I. Janigova and J. Stejskal, "Thermal Ageing of Conducting Polymeric Composites," Polymer Degradation and

Stability, 82, pp. 251–256, 2003.

[79]. M. Omastova, J. Prokes, S. Kosina and D. Hlavata, "Stability of Electrical Properties of Conducting Polymer Composites," Macromolecular Symposia, 170, pp. 241–248, 2001.

[80]. S. Gao and J. Kim, "Cooling Rate Influences in Carbon Fibre/PEEK Composites. Part 1. Crystallinity and Interface Adhesion," Composites Part A: Applied Science and Manufacturing, Volume 31, Issue 6, pp. 517-530, 2000.

[81]. J. Huang, Y. Wen, C. Kang, W. Tseng, and M. Yeh, "Nonisothermal Crystallization of High Density Polyethylene and Nanoscale Calcium Carbonate Composites," Polymer Engineering and Science, 48, pp.1268–1278, 2008.

[82]. A. Wald, Sequential Analysis, John Wiley & Sons, New York, NY, 1947.

[83]. K. Gross and W. Lu, "Early Detection of Signal and Process Anomalies in Enterprise Computing Systems," Proc. 2002 IEEE Int'l Conf. on Machine Learning and Applications (ICMLA), Las Vegas, NV,2002.

[84]. K. Whisnant, K. C. Gross, and N. Lingurovska, "Proactive fault monitoring in enterprise servers," in Proceedings of the International Conference on Computer Design, pp. 3-10, June 2005.

[85]. K. Gross and K. Humenik, "Sequential Probability Ratio Tests for Nuclear Plant Component Surveillance," Nuclear Technology, 93:131, 1991.

[86]. S. Cheng, K. Tom, and M. Pecht, "A Wireless Sensor System for Prognostics and Health Management," IEEE Sensors Journal, Volume 10, Issue 4, pp. 856-862, 2010.

[87]. H. Sohn, D. Allen, K. Worden, and C. Farrar, "Statistical Damage Classification Using Sequential Probability Ratio Tests," Structural Health Monitoring, Vol. 2(1), pp. 57–74, 2003.

[88]. Z. Stoumbo, and M. R.Jr. Reynolds, "The SPRT Control Chart for the Process Mean with Samples Starting at Fixed Times," Nonlinear Analysis, 2, pp.1-34, 2001.

[89]. M. R.Jr. Reynolds and Z. Stoumbo, "The SPRT Chart for Monitoring a Proportion," IIE Transactions, 30, pp. 545-561, 1998.

[90]. A. Wald, "Sequential Test of Statistical Hypotheses," The Annals of Mathematical Statistics, Vol. 16, No. 2, pp. 117-186, 1945.

[91]. A. Wald and J. Wolfowitz, "Optimum Character of the Sequential Probability Ratio Test," The Annals of Mathematical Statistics, Vol. 19, pp. 326-339, 1948.

[92]. A. Miron, "A Wavelet Approach for Development and Application of A Stochastic Parameter Simulation System," PhD Dissertation in Nuclear Engineering of University of Cincinnati, 2001.

[93]. J. Herzog, S. Wegerich, R. Singer, K. Gross, "Theoretical Basis of the Multivariate State Estimation Technique (MSET)," Argonne National Laboratory NT Technical Memorandum No. 49, 1997.

[94]. R. Kohavi, "A Study of Cross validation and Bootstrap for Accuracy Estimation and Model selection," In Proceedings of International Joint Conference on AI, pp. 1137-1145, 1995.

[95]. W. Zucchini, "An Introduction to Model Selection," Journal of Mathematical

Psychology, 44, pp. 41-61, 2000.

[96]. J. Gertheiss, and G. Tutz, "Feature Selection and Weighting by Nearest Neighbor Ensembles," Chemometrics and Intelligent Laboratory Systems, Vol. 99, Issue 1, pp. 30-38, 2009.

[97]. M. Mullin, and R. Sukthankar, "Complete Cross validation for Nearest Neighbor Classifiers," 17th International Conference on Machine Learning (ICML), Stanford, California, 2000.

[98]. R. Setiono, "Feedforward Neural Network Construction Using Cross Validation," Neural Computation, 13, pp.2865–2877, 2001.

[99]. A. Krogh and J. Vedelsby, "Neural Network Ensembles, Cross Validation, and Active Learning, Advances in Neural Information Processing Systems," Tesauro, G., Touretsky, D., and Leen, T.., Vol. 7, Cambridge, Mass.: MIT Press, 1995.

[100]. B. Efron, "Estimating the Error Rate of a Prediction Rule: Improvement on Cross validation," Journal of American Statistical Association, 78:316–331, 1983.

[101]. M. Browne, "Cross validation Methods," Journal of Mathematical Psychology, Volume 44, Issue 1, pp. 108-132, 2000.

[102]. M. Stone, "Cross-Validatory Choice and Assessment of Statistical Predictions (with discussion)," Journal of the Royal Statistical Society, Series B, 36, pp.111-147, 1974.

[103]. G. Box and D. Cox, "An Analysis of Transformations," Journal of the Royal Statistical Society, Series B, Vol. 26, pp. 211-246, 1964.

[104]. Y. Chou, A. Polansky, and R. Mason, "Transforming Non-normal Data to Normality in Statistical Process Control," Journal of Quality Technology, Vol. 30, No.2, pp. 133-141, 1998.

[105]. M. Djukanovic, S. Ruzic, B. Babic, D. J. Sobajic, and Y. H. Pao, "A Neural-net based Short Term Load Forecasting Using Moving Window Procedure ," Electrical Power & Energy Systems, vol. 17, no. 6, pp. 391 - 397, 1995.

[106]. Z. Ren, and Z. Hao, "Application of Moving Windows Autoregressive Quadratic Model in Runoff," International Conference on Industrial Mechatronics and Automation, pp. 200-203, 2009.

[107]. M. Pecht and S. Cheng, "Prognostics and Health Management Method for Aging Systems", U.S. Patent Application Publication, No. US 2010/0191681 A1, Jul. 2010.

[108]. A. Smola and B. Scholkopf, "A Tutorial on Support Vector Regression," Statistics and Computing, 14, pp. 199-222, 2004.